# A Systematic Stiffness-Temperature Model for Polymers and Applications to the Prediction of Composite Behavior

Céline A. Mahieux

Dissertation submitted to the Faculty of Virginia Tech
in partial fulfillment of the requirements for the degree of

Doctor of Philosophy
in
Materials Engineering and Science

Kenneth L. Reifsnider (Chair)
Scott W. Case
Stephen L. Kampe
John J. Lesko
Hervé L. Marand

February 26, 1999
Blacksburg, Virginia

`

Keywords: Polymers, composites, temperature, stiffness, life-prediction

# A Systematic Stiffness-Temperature Model for Polymers and Applications to the Prediction of Composite Behavior

Céline A. Mahieux

(ABSTRACT)

Polymer matrix composites (PMC's) are now being used more and more extensively and over wider ranges of service conditions. Large changes in pressure, chemical environment or temperature influence the mechanical response of such composites. In the present effort, we focus on temperature, a parameter of primary interest in almost all engineering applications. In order to design composite structures without having to perform extensive experiments (virtual design), the necessity of establishing theoretical models that relate the macroscopic response of the structure to the microscopic properties of the constituents arises. In the first part of the present work, a new stiffness versus temperature model is established. The model is validated using data from the literature. The influence of the different polymer's properties (Molecular weight, crystallinity, and filler content) on the model are studied by performing experiments on different grades of four polymers PMMA, PEEK, PPS, and PB. This statistical model is proven to be applicable to very different polymers (elastomers, thermoplastics, crystalline, amorphous, cross-linked, linear, filled, unfilled…) over wide temperature ranges (from the glassy state to the flow region). The most attractive feature of the proposed model is the capability to enable a description of the polymer's mechanical behavior within and across the property transition regions.

In order to validate the feasibility of using the model to predict the mechanical response of polymer matrix composites, the stiffness-temperature model is used in various micromechanical models (rule of mixtures, compression models for the life prediction of unidirectional PMC's in end-loaded bending…). The model is also inserted in the MRLife prediction code to predict the remaining strength and life of unidirectional PMC's in fatigue bending. End-loaded fatigue experiments were performed. A good correlation between theoretical and experimental results is observed. Finally, the model is used in the Classical Lamination Theory; some laminates were found to exhibit stress reversals with temperature and behaved like thermally activated mechanical switches.

## Dedication

This work is dedicated to my parents: Francis and Guitty Mahieux

## Acknowledgments

The author would like to thank the following people:

The author's parents Francis and Guitty whose love and constant moral support made this work possible.

Dr. K. L. Reifsnider for his tremendous help, valuable advice and support.

Sheila Collins and Beverly Williams for their help and moral support.

Scott Case, Dave Dillard, Hervé Marand, Steve Kampe and Jack Lesko for their guidance in the research process.

Robert Young for his help in processing the material.

Mac McCord for his help in the experimental work.

Josh Jackson, Shannon Pipik, and Blair Russell for their essential contributions to the experimental work.

All the members of the Materials Response Group for their support and camaraderie.

## Table of contents

(ABSTRACT) ii
Dedication iv
Table of contents vi
List of illustrations x
List of tables xv
Chapter 1 Introduction and literature review 1
1.1 Introduction 1
1.2 Literature review 2
1.2.1 Typical modulus changes with temperature: the 4 regions of the master curve 2
1.2.1.1 The glassy state (region 1) 3
1.1.1.2 The glass transition (region 2) 6
1.1.1.2.1 The thermodynamic theory of the glass transition 7
1.1.1.2.2 Free-volume theory and WLF equation 8
1.1.1.1.3 Spring and dashpots models 9
1.1.1.1.4 KWW equation 10
1.1.1.1.5 Other viscoelastic models 11
1.1.1.3 The rubbery state (region 3) 12
1.1.1.4 The liquid flow region (region 4) 13
1.1.2 Molecular simulations 15
1.1.3 Micromechanics 16
1.1.3.1 Tensile experiments 16
1.1.3.2 Rule of mixtures 19
1.1.3.3 End-loaded bending stress-rupture 19
1.1.3.4 Macromechanics 20
1.3 Objective 20
Chapter 2 Stiffness versus temperature predictions for polymers 21
2.1 Preliminary comments 21
2.2 Theoretical modeling 22
2.3 Feasibility 29

2.3.1 Literature data ..... 29
2.3.2 Discussion ..... 33
2.4 Experimental work ..... 34
2.4.1 Material selection ..... 34
2.4.1.1 PMMA ..... 34
2.4.1.2 PEEK ..... 35
2.4.1.3 PPS ..... 36
2.4.1.4 Rubber ..... 36
2.4.1.5 Composite ..... 37
2.4.2 Materials processing and samples preparation ..... 37
2.4.2.1 PEEK processing ..... 37
2.4.2.2 PPS processing ..... 38
2.4.2.3 Samples manufacturing ..... 38
2.4.3 Crystallinity modifications ..... 38
2.4.3.1 Obtaining the maximum crystallinity of the material ..... 38
2.4.3.1.1 PEEK ..... 38
2.4.3.1.2 PPS ..... 39
2.4.3.1.3 Composite ..... 39
2.4.3.2 Obtaining amorphous material ..... 39
2.4.3.2.1 PPS ..... 39
2.4.3.2.2 PEEK ..... 41
2.4.3.3 Obtaining intermediate crystallinity ..... 42
2.4.3.3.1 PEEK ..... 42
2.4.3.3.2 PPS ..... 42
2.4.3.3.3 Composite ..... 43
2.4.4 Material characterization ..... 43
2.4.4.1 Density measurements ..... 43
2.4.4.2 DSC ..... 47
2.4.4.2.1 Calibration procedure ..... 47
2.4.4.2.2 DSC Results ..... 49
2.4.5 Summary of the samples and properties ..... 51

2.4.6 DMA ..... 52
1.5 DMA results and model validation ..... 53
1.5.1 Varying the crystallinities ..... 53
1.5.1.1 PPS ..... 53
1.5.1.1.1 PPS Celanese ..... 53
1.5.1.1.2 PPS PR09 ..... 55
1.5.1.1.3 PPS PR10 ..... 56
1.5.1.2 PEEK ..... 57
1.5.1.2.1 PEEK 150 ..... 57
1.5.1.2.2 PEEK 450 ..... 59
1.5.1.2.3 Composite ..... 59
1.5.2 Varying the molecular weights ..... 60
1.5.2.1 PMMA ..... 61
1.5.2.2 PPS ..... 62
1.5.2.3 PEEK ..... 62
1.5.2.4 Polybutadiene ..... 63
1.5.3 Varying the filler content ..... 64
1.6 Discussion ..... 65
Chapter 3 Effect of temperature on the mechanical behavior of polymer matrix composites ..... 71
3.1 Tensile experiments ..... 71
1.2 Stress rupture ..... 79
1.2.1 Background ..... 79
1.2.2 Experimental work ..... 82
1.2.2.1 The material ..... 82
1.2.2.2 Experimental apparatus and results ..... 83
1.2.3 Analysis ..... 88
1.1.4 Discussion ..... 97
1.3 Fatigue and life prediction ..... 101
1.3.1 Experimental work ..... 101
1.3.1.1 Fatigue ..... 101

1.3.1.1.1 Experimental apparatus ..... 101
1.3.1.1.2 Experimental results ..... 104
1.3.1.2 Stress rupture and remaining strength ..... 110
1.3.2 Modeling and results ..... 112
1.3.2.1 The MRLife concept ..... 112
1.3.2.2 The incremental approach ..... 113
1.3.2.3 Application to fatigue bending at elevated temperature ..... 115
1.3.2.4 Discussion ..... 119
1.4 Classical Lamination Theory ..... 121
1.4.1 AS4/PEEK laminate ..... 121
1.4.1.1 Pure Axial loading ..... 123
1.4.1.2 Thermal constraint ..... 125
1.4.1.3 Thermal and mechanical load combination ..... 126
1.4.2 AS4/PPS-AS4/PEEK hybrid laminate ..... 128
1.4.3 Discussion ..... 130
Chapter 4 Conclusions and recommendations ..... 132
4.1 Summary ..... 132
4.2 Recommendations ..... 132
4.2.1 Inputs for the polymer modulus versus temperature model ..... 133
4.2.2 The Weibull coefficients ..... 135
4.2.3 Other areas of interest ..... 135
4.2.4 Micromechanics ..... 136
4.2.5 Strength ..... 136
4.2.6 End-loaded bending experiments on laminate composites ..... 136
4.2.7 The Classical Lamination Theory ..... 137
4.3 Conclusions ..... 137
References ..... 138
Vita ..... 144

## List of illustrations

Figure 1. Modulus versus temperature for a typical polymer ..... 2
Figure 2. Crankshaft mechanism ..... 4
Figure 3. Stiffness versus temperature for unidirectional AS4/PPS. From Walther ..... 18
Figure 4. Strength versus temperature for unidirectional AS4/PPS. From Walther ..... 18
Figure 5. Modulus versus temperature for a typical polymer ..... 23
Figure 6. Schematic of bonds in polymer materials ..... 23
Figure 7. Reptation ..... 24
Figure 8. Inputs of Equation 52. Schematic. ..... 28
Figure 9. PMMA ..... 30
Figure 10. PVDC ..... 31
Figure 11. Poly(1,4-BFB, Bis A) ..... 31
Figure 12. $(PEO)_{0.82}(Fe(SCN)_3)_{0.18}$ ..... 32
Figure 13. PEEK(5K)PSX(3K) ..... 32
Figure 14. PEEKt(5K)PSX(5K) ..... 33
Figure 15. PMMA molecule ..... 34
Figure 16. PEEK molecule ..... 35
Figure 17. PPS molecule ..... 36
Figure 18. Polybutadiene molecule ..... 37
Figure 19. Specimens in the tube furnace ..... 40
Figure 20. Quenching of the samples ..... 41
Figure 21. X-rays of PPS Celanese. Plate as received and two specimens after 1 hour at 130°C ..... 43
Figure 22. Density measurements apparatus ..... 44
Figure 23. Crystallinity contents ..... 46
Figure 24. Calibration curves ..... 47
Figure 25. Single cantilever sample arrangement ..... 52
Figure 26. Experimental and theoretical results for various crystallinities of PPS Celanese ..... 54
Figure 27. Experimental and theoretical results for various crystallinities of PPS PR09. 55

Figure 28. Experimental and theoretical results for various crystallinities of PPS PR10. 56
Figure 29. Experimental and theoretical results for various crystallinities of PEEK 150 58
Figure 30. Experimental and theoretical results for various crystallinities of PEEK 450 59
Figure 31. Experimental and theoretical results for various crystallinities of AS4/PPS composite ..... 60
Figure 32. Experimental and theoretical results for PMMA ..... 61
Figure 33. Experimental and theoretical results for various molecular weights of PPS.. 62
Figure 34. Experimental and theoretical results for various molecular weights of PEEK 63
Figure 35. Experimental and theoretical results for various molecular weights of unfilled polybutadiene ..... 64
Figure 36. Experimental and theoretical results for polybutadiene with different contents of carbon black ..... 65
Figure 37. Theoretical variations of the stiffness versus temperature curve. $m_2$=20, $m_3$=20, $m_1$=1, 5, 20, and 40 ..... 66
Figure 38. Theoretical variations of the Stiffness versus Temperature curve. $m_1$=5, $m_3$=20, $m_2$=1, 5, 20, and 40 ..... 67
Figure 39. $m_2$ versus crystallinity content ..... 68
Figure 40. $m_2$ versus carbon black content for polybutadiene ..... 69
Figure 41. Theoretical variations of the Stiffness versus Temperature curve. $m_1$=5, $m_2$=20, $m_3$=1, 5, 20, and 40 ..... 70
Figure 42. Efficiency factor versus temperature for AS4/PEEK composite ..... 75
Figure 43. Stiffness of unidirectional AS4/PEEK samples at various temperatures. Experimental data from Walther. ..... 75
Figure 44. Efficiency factors for the AS4/PPS composite. ..... 77
Figure 45. Stiffness of unidirectional AS4/PPS samples at various temperatures. Experimental data from Walther ..... 77
Figure 46. Normalized longitudinal and transverse moduli versus efficiency factor for a 50% fiber volume fraction ..... 79
Figure 47. End-loaded compression bending fixture. From Russell et. al. ..... 80
Figure 48. Microbuckling in end-loaded experiments. From Mahieux et. al. ..... 81
Figure 49. DSC of the amorphous and crystalline AS4/PPS composite ..... 83

Figure 50. Time-to-failure versus maximum applied strain at 90°C. (The empty squares indicate run-out experiments). From Russell et. al. ..... 84
Figure 51. Time-to-failure versus maximum applied strain at 120°C from..... 84
Figure 52. Time-to-failure versus temperature for specimens bent at 90% of their strain-to-failure ..... 85
Figure 53. Time-to-failure versus applied maximum strain at 75°C ..... 86
Figure 54. Time-to-failure versus applied maximum strain at 90°C ..... 86
Figure 55. Time-to-failure versus temperature at a maximum normalized strain of 75% (strain/ultimate strain-to-failure in tension)..... 87
Figure 56. Time-to-failure versus temperature at a maximum normalized strain of 90% (strain/ultimate strain-to-failure in tension)..... 87
Figure 57. Schematic of a microbuckle. $\alpha$ and $\beta$ are the characteristic angles ..... 88
Figure 58. Modulus versus temperature for PPS PR09 (low molecular weight) ..... 91
Figure 59. Efficiency factor for AS4/PPS composite ..... 91
Figure 60. Reference shear stress for AS4/PPS composite..... 92
Figure 61. Time-to-failure versus strain level prediction at 4 example temperatures (30°C, 90°C, 120°C, 200°C) for the crystalline and amorphous material..... 92
Figure 62. Time-to-failure versus temperature prediction at 4 example strain levels (0.005, 0.0075, 0.01, 0.0125, 0.015) for the crystalline and amorphous material .... 93
Figure 63. Time-to-failure versus temperature for crystalline specimen bent at 90% of its maximum strain-to-failure ..... 94
Figure 64. Time-to-failure versus maximum strain-to-failure for crystalline specimen at 90°C..... 94
Figure 65. Time-to-failure versus maximum strain-to-failure for crystalline specimen at 120°C..... 95
Figure 66. Time-to-failure versus temperature for amorphous specimen bent at 75% of its maximum tensile strain-to-failure ..... 95
Figure 67. Time-to-failure versus temperature for amorphous specimen bent at 90% of its maximum strain-to-failure ..... 96
Figure 68. Time-to-failure versus maximum strain-to-failure for amorphous specimen at 75°C..... 96

Figure 69. Time-to-failure versus maximum strain-to-failure for amorphous specimen at 90°C ..... 97
Figure 70. Underneath of the bent specimen in oven (sequence of events). ..... 100
Figure 71. End-loaded fatigue fixture from Jackson et. al. ..... 102
Figure 72. Fatigue machine schematic. From Pipik ..... 103
Figure 73. Fatigue machine schematic (details) ..... 103
Figure 74. Room temperature End-loaded fatigue experiments ..... 104
Figure 75. SEM picture. Room temperature bending fatigue. Microbuckle on the compression side ..... 105
Figure 76. SEM picture. Room temperature bending fatigue. Damage on the compression side ..... 105
Figure 77. SEM picture. Room temperature bending fatigue. Damage on the compression side ..... 106
Figure 78. SEM picture. Room temperature bending fatigue. Damage on the compression side ..... 106
Figure 79. End-loaded fatigue experiments at 75°C ..... 107
Figure 80. End-loaded fatigue experiments at 90°C ..... 107
Figure 81. SEM picture. 90°C bending fatigue. Microbuckle on the compression side ..... 108
Figure 82. SEM picture. 90°C bending fatigue. Microbuckle on the compression side ..... 108
Figure 83. End-loaded fatigue experiments at 75% ..... 109
Figure 84. End-loaded fatigue experiments at 90% ..... 109
Figure 85. Remaining strength. Stress rupture experiments at 90°C and 38% strain-to-failure ..... 111
Figure 86. Remaining strength. Stress rupture experiments at 90°C and 57% strain-to-failure ..... 111
Figure 87. Sinusoidal variations of the failure function Fa (with $Fa_{max}$=75%) ..... 115
Figure 88. Isostrain experiments and theoretical results at 75% for various temperatures ..... 117

Figure 89. Isostrain experiments and theoretical restults at 90% for various temperatures ..... 117
Figure 90. Isotemperature experiments and theoretical results at 75°C for various strain levels ..... 118
Figure 91. Isotemperature experiments and theoretical results at 90°C for various strain levels ..... 118
Figure 92. SEM picture. Stress rupture at 90°C. Failure surface ..... 119
Figure 93. SEM picture. Room temperature bending fatigue. Failure surface ..... 119
Figure 94. SEM picture. Bending fatigue at 90°C. Failure surface ..... 120
Figure 95. $E_x$, $E_y$ and $G_{xy}$ versus temperature for the [AS4/PEEK$_{45°}$, AS4/PEEK$_{0°}$, AS4/PEEK$_{-45°}$, AS4/PEEK$_{90°}$]$_s$ laminate. ..... 122
Figure 96. $\upsilon_{xy}$ versus temperature for the ..... 123
Figure 97. Fiber direction stresses versus temperature in each ply. ..... 124
Figure 98. Fiber direction strains versus temperature in each ply. $N_x$=10 MPa. $\Delta T$=0°C. ..... 124
Figure 99. Fiber direction stresses versus temperature in each ply. ..... 125
Figure 100. Fiber direction strains versus temperature in each ply. $N_x$=0 Mpa. $\Delta T$=-100°C. ..... 126
Figure 101. Fiber direction stresses versus temperature in each ply. ..... 127
Figure 102. Fiber direction strains versus temperature in each ply. $N_x$=10 MPa. $\Delta T$=-100°C. ..... 127
Figure 103. $E_x$, $E_y$ and $G_{xy}$ versus temperature for the ..... 128
Figure 104. $\upsilon_{xy}$ versus temperature for the ..... 129
Figure 105. Fiber direction stresses versus temperature in each ply. $N_x$=10 MPa. $\Delta T$=-100°C. Hybrid laminate. ..... 129
Figure 106. Fiber direction strains versus temperature in each ply. $N_x$=0 MPa. $\Delta T$=-100°C. Hybrid laminate. ..... 130

## List of tables

Table 1. Density Measurements..... 45
Table 2. Crystallinity measurements..... 49
Table 3. Summary of the samples..... 51
Table 4. Parameters for PPS Celanese..... 54
Table 5. Parameters for PPS PR09..... 55
Table 6. Parameters for PPS PR10..... 57
Table 7. Parameters for PEEK 150..... 58
Table 8. Parameters for PEEK 450..... 59
Table 9. Parameters for AS4/PPS composite..... 60
Table 10. Parameters for PMMA..... 61
Table 11. Parameters for unfilled polybutadiene..... 64
Table 12. Parameters for filled polybutadiene..... 65
Table 13. Dependence of the input parameters on the microstructure..... 132

# Chapter 1 Introduction and literature review

## 1.1 Introduction

Unidirectional composites loaded in the fiber direction are often considered to be "fiber-controlled" materials. If the temperature has no or little effect on the properties (e.g. strength, stiffness) of the fibers, it is often assumed that the properties of the composite will remain constant in the fiber direction, even for large temperature changes.

However if we consider typical numerical values for carbon fiber/polymer matrix composites ($E_{fiber}$=180 MPa, $V_{fiber}$=20%, $E_{matrix}$=$4.10^3$ MPa below Tg and $E_{matrix}$=1 MPa above Tg) and calculate the stiffness of a unidirectional composite according to a simple rule of mixtures, we get an axial stiffness $E_{11}$ of the overall composite of 30 MPa below Tg and 27 MPa above Tg. In the axial direction the stiffness change is of 11% for the overall composite (this change would be 20% for a polymer composite reinforced with 50% of E-glass fibers). This trend is accentuated for low volume fractions of fibers. In the transverse direction, the change in the stiffness of the same composite in its glassy and rubbery state would be of one order of magnitude.

These very basic computations demonstrate the fact that the variation of the stiffness of the composite with temperature can not be ignored, even in the axial direction of "fiber-dominated" composites.

Macromechanics models and durability tools require a knowledge of the composite quasi-static properties. Most of the tests to evaluate these properties require laboratory work and destructive testing. Ideally, we could eliminate those if we knew the evolution of the properties of the composites' constituents under service conditions.

Composite materials are more and more extensively used over wide ranges of service conditions. Therefore it becomes necessary to have an accurate description of the variations of the material properties under various and extreme conditions. In our case, we will focus on temperature. In transition regions, the properties of the material change significantly over a small temperature range. To enable the use of polymer matrix composites within these transition regions, we need to be able to analytically describe the

changes of the polymers' properties with temperature. We will restrict our discussion to changes in the stiffness of the material.

In the following section, the relaxation process of a typical polymer is briefly described. The different theories of stiffness versus temperature models are reviewed. The last part of the literature review focuses on previous studies of the effect of temperature on the mechanical behavior of PMC's that we arbitrarily chose to serve as examples of micromechanics and macromechanics applications.

## 1.2 Literature review

### *1.2.1 Typical modulus changes with temperature: the 4 regions of the master curve*

It is well know that the stiffness of polymers changes with temperature due to molecular rearrangements. The modulus versus temperature curve for a typical polymer exhibiting a secondary relaxation is illustrated by Figure 1. This curve is traditionally divided into the 4 distinct regions. Let us analyze these different regions, and review the physical processes of relaxation that serve as the basis for the different models and behavior.

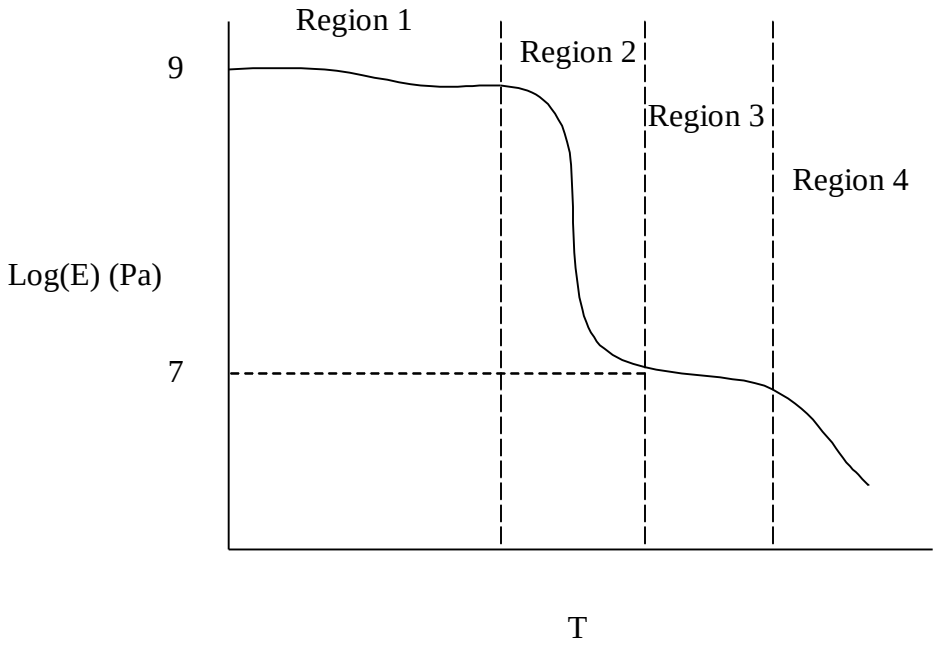


**Figure 1. Modulus versus temperature for a typical polymer**

*1.2.1.1 The glassy state (region 1)*

At very low temperatures, the modulus of polymers is often assumed to be constant as a function of temperature, and typically of the order of 3 GPa[1]. A relationship between the modulus (E) and the cohesive energy density (CED), energy required to move a detached segment into the vapor phase, was derived by Tobolsky[2] from the Lennard-Jones potential[3] to provide a simple approximate explanation for the constant modulus (Equation 1).

**Equation 1**

$$E \approx 9.6(CED)$$

for a Poisson's ratio equal to 0.3. However the presence of peaks during thermomechanical tests, for example, evidences the presence of molecular motion, even for low temperatures. As the temperature increases, the polymer can undergo several transitions. Typically the first transition is called $\gamma$ relaxation, the second is termed the $\beta$ relaxation, and the third is referred to as the glass transition (Tg) or the $\alpha$ transition[1]. This convention will be used in the remaining of this dissertation. One may note that this convention is modified for some semi-crystalline polymers such as PE, PP, PEO, POM that exhibit the presence of a specific transition, $a_c$, before the glass transition (called ß for these exceptions). The presence of the $a_c$ was attributed to reorientational motions within the crystals[78].

The $\gamma$ and $\beta$ transitions (secondary transitions) reflect molecular motions occurring in the glassy state (below Tg). In the glassy region, the thermal energy is much smaller than the potential energy barriers to large-scale segmental motion and translation, and large segments are not free to jump from one-lattice site to another[4]. Secondary relaxations result from localized motions. The secondary relaxations can be of 2 types[4]: side group motion or the motion of few main chains. It is difficult to establish a general model for these relaxations due to the molecular specificity (nature of the side groups). However, the crankshaft mechanism attributed to different authors[5,6] illustrates most of these mechanisms (Figure 2).

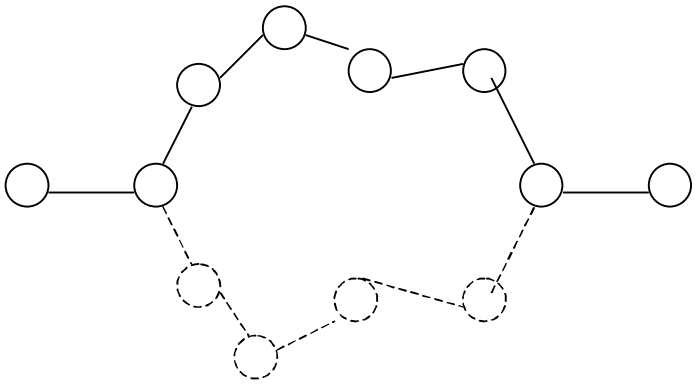

**Figure 2. Crankshaft mechanism**

The rotation of a part of the main chain can be activated by temperatures lower than the glass transition temperature. This is the case in many polymers containing $(CH_2)_n$ sequences where n equals 4 or greater[4] that exhibit a transition at -120°C. Even larger units can relax[7]. Group motion can be illustrated by the β relaxation of poly(alkyl methacrylate)s. If the radical is a cyclohexyl ring, a relaxation at 180K can be observed at 1Hz. This phenomenon can be attributed to an intramolecular chair-chair transition in the ring.

The study of β-relaxations can be complex and depends on the chemistry of the material. We will cite, for example, the detailed descriptions of β-relaxations given by Bartolotta[8] et. al. for polyethylene oxide-iron thiocyanate polymeric complexes (where the influence of the salt content is also discussed), for thermosetting systems by Wang[9] (influence of cure extent on β relaxation, explained by the difference in the micromechanisms before and after gelation due to cross linking). Study of the secondary relaxations also appear in the study of PEEK by Krishnaswamy[10] and poly(methyl methacrylate) by Muzeau[11].

According to Aklonis[4], a time-temperature or frequency-temperature superposition scheme can be applied to these relaxations. However the following Arrhenius equation:

**Equation 2**

$$\log a_T \propto -\frac{H_a}{2.303RT}$$

where $a_T$ is the time-temperature shift factor, $H_a$ is the activation energy, R is the gas constant and T the temperature, must be applied instead of the traditional WLF equation[12]

(detailed in the following section). The change in viscosity due to temperature in the glassy state depends on the presence of a "hole" for the polymer segment to move into. Therefore the presence of an energy barrier justifies the use of an activation energy. The log $a_T$ versus 1/T plots for a secondary relaxation will be a straight line (not a curve as in the WLF case)[4].

Recognizing the need for a modulus-temperature explicit relationship, an alternate approach was taken by Van Krevelen[13]. For a solid, the shear modulus (G) at a given temperature can be written as:

**Equation 3**

$$G(T) = r(T) \cdot \left( \frac{U_H}{V(T)} \right)^6$$

Where ρ is the density of the medium, V is the specific volume, M is the molar mass of the monomer and $U_H$ is the Hartmann[14] function:

**Equation 4**

$$U_H = V \cdot u_{sh}^{1/3}$$

$U_H$ is a molar elastic wave function, and $u_{sh}$ is the velocity of propagation of transverse sound waves. The problem in applying these two equations over a wide range of temperatures is that we need to know the variations of the polymer density or specific volume as a function of temperature. Van Krevelen[13] suggests empirical equations to compute the changes of stiffness for a semi-crystalline material with temperature:

**Equation 5**

$$\frac{G_a(T)}{G_a(T_{ref})} = \frac{T_g / T_{ref} + 2}{T_g / T_{ref} + 2 \cdot T / T_{ref}} \qquad \text{for } T<T_g$$

**Equation 6**

$$\frac{G_c(T)}{G_c(T_{ref})} = \exp\left[ -2.65 \frac{T_m / T_{ref} - T_m / T}{T_m / T_{ref} - 1} \right] \qquad \text{for } T>T_{ref}\text{-}100$$

**Equation 7**

$$G_{sc} = G_a + x_c^2 (G_c - G_a)$$

where the subscripts c, a, m, g, and sc denote crystalline, amorphous, melting, glass transition, and semi-crystalline, respectively.

Bicerano[15] suggests using Equation 3, and introduces an empirical equation for the specific volume variation as a function of temperature that can be directly used in Equation 3.

**Equation 8**

$$V(T) = V_{ref} \frac{1.57 \cdot T_g + 0.3 \cdot (T - T_g)}{1.42 \cdot T_g + 44.7}$$

However these approaches are restricted to low temperatures and the solid phase. Furthermore, they are empirical and are not related to the physics of the relaxation process. Finally, results generated by these equations have not been compared, to the author's knowledge, with experimental data.

Below the glass transition temperature, the molecules are in a "non-equilibrium" state. Densification, also referred to as physical aging, can be observed over very long periods of time. The molecules tend to reorganize (decrease the free volume) and try to reach the equilibrium state. Several theories have been established concerning this complex process where "relaxation time depends on entropy and free volume, while the rate of change for both is controlled by the changing relaxation time. The relaxation process is coupled with thermodynamic change."[16] Different theories have been established to describe this process (See Matsuoka[16] for details) and are beyond the scope of this dissertation.

*1.2.1.2 The glass transition (region 2)*

The glass transition region is characterized by a steep drop in the polymer instantaneous or storage modulus. "Qualitatively, the glass transition region can be interpreted as the onset of long-range, coordinated molecular motion. While only 1-4 chain atoms are involved in motions below the glass transition temperature, some 10-50

chain atoms attain sufficient thermal energy to move in a coordinate manner in the glass transition"[1]. From mechanical analysis, Tg is given by the peak of the loss tangent or the inflexion point in the modulus versus temperature resulting from quasi-static experiments. The glass transition temperature can also be determined by the point of discontinuity in the $C_p$ (heat capacity), $\alpha$ (volume coefficient of expansion), or G'' (loss shear modulus) versus temperature curves[1].

We will not discuss the full detail of the glass transition theories here. However, we will briefly outline the characteristics and assumptions of the main models.

1.2.1.2.1 The thermodynamic theory of the glass transition

The changes occurring at the glass transition can also be thought of as changes in the entropy of the material. Gibbs and Di Marzio[17] assume the existence of a true transition occurring at a temperature $T_2$. "Hindered rotation in the polymer chain is assumed to arise from two energy states"[4]. The difference between these two energy states can be written as: $\Delta E = e_1 - e_2$ , where $\varepsilon_1$ is the energy of one possible orientation and $\varepsilon_2$ is the energy of all the other orientations. If the number of holes is denoted by $n_o$, the degree of polymerization by x, the number of configurations for the $n_x$ molecule to be packed into the $xn_x+n_o$ sites by W, and the number of molecules packed in a conformation I by $f_i n_x$, then the configurational partition function can be written as:

**Equation 9**

$$Q = \sum_{f,n_n,n_o} W(f_1 n_x \ldots, f_i n_x \ldots, n_o) \times \exp\left(-\frac{E\left(f_1 n_x \ldots, f_i n_x \ldots, n_o\right)}{kT}\right)$$

From statistical thermodynamics we may obtain the entropy S:

**Equation 10**

$$S = kT\left(\frac{\P \ln Q}{\P T}\right)_{V,n} + k \ln Q$$

The glass transition and viscoelastic behavior of polymer are still controversial topics in the scientific community. The free volume concept is presented below as an alternative to the thermodynamic theory. We will only point out the fact that a diminution in the free volume hindering the motion of the chains can be seen as a decrease in entropy that

corresponds to the solid state. The two theories are therefore closely related but originate from fundamentally different considerations, the free volume theory being based upon kinetics considerations while the entropy calculations result from thermodynamics concepts.

1.2.1.2.2 Free-volume theory and WLF equation

The free volume theory is based on the assumption that the presence of free volume[4] is needed in order to allow cooperative motion of the molecular chains. As temperature increases the free volume increases, making reptation easier. Fox and Flory[18] related the free volume $V_f$ to temperature:

**Equation 11**

$$V_f = K + (a_R - a_G)T$$

where K is related to the free volume at absolute zero and $a_R$ and $a_G$ are the coefficients of thermal expansion of the rubbery and glassy states, respectively. The free volume at the glass transition is found to be a constant and assumed to linearly vary above $T_g$, as expressed by the WLF[12] equations (Equation 12, Equation 13):

**Equation 12**

$$E(T_g, \frac{t}{a_T}) = E(T,t)$$

**Equation 13**

$$\log a_T = \frac{-C_1(T - T_g)}{C_2 + T - T_g}$$

The WLF equations as stated above do not give any insight on the molecular behavior of the material. All the parameters influencing the modulus are included in the two material parameters $C_1$ and $C_2$, that mainly result from curve fitting. The WLF equations are only a time-temperature equivalence tool. These relations allow us to predict the viscoelastic response of the once we know any two of the following three curves: modulus versus time for the polymer at any temperature; modulus versus temperature curve at any time; and the shift factors relative to some reference temperature[4]. Therefore a prediction of the modulus versus time curve of the polymer is

needed in addition to this tool in order to evaluate the stiffness change of the material with temperature.

1.2.1.2.3 Spring and dashpots models

Mechanical models have been established to describe the behavior of polymers with time. The simplest of these models are the Maxwell and Voight models[1]. The Maxwell model consists of the association of a spring and dashpot in series. The equation of motion for this system is:

**Equation 14**

$$\frac{de}{dt} = \frac{1}{E}\frac{ds}{dt} + \frac{s}{h}$$

where E is the elastic constant associated with the presence of the spring, $\eta$ the viscosity coefficient associated with the dashpot, $\varepsilon$ is the strain, and $\sigma$ is the stress.

The response of the Maxwell model to a stress relaxation experiment can easily be calculated from Equation 14 and leads to:

**Equation 15**

$$E(t) = E\exp\left(-\frac{t}{t}\right)$$

where $\tau$ is a characteristic relaxation time.

The response to a creep experiment is:

**Equation 16**

$$D(t) = D + \frac{t}{h}$$

where D is the compliance of the system.

The Voight model is the assembly of a spring and dashpot in parallel. The equation of motion for such a system is:

**Equation 17**

$$s(t) = e(t)E + h\frac{de(t)}{dt}$$

Leading to Equation 18 for stress relaxation and Equation 19 for creep.

**Equation 18**

$$E(t) = E$$

**Equation 19**

$$D(t) = D\left(1 - \exp\left(\frac{-t}{t}\right)\right)$$

Clearly Equation 16 and Equation 18 do not correspond to experimental results. More complex models have been established, combining several springs and dashpots in series and parallel. Any modulus versus time plot can be fitted by combining a large number of mechanical elements and varying the numerical values of the characteristic relaxation times. However, the choice of the adequate model for a material results from curve fitting and is not based on chemistry or related to the microstructure of the polymer.

1.2.1.2.4 KWW equation

Another model of importance relating the modulus of a polymer to time is the KWW[19,20] equation:

**Equation 20**

$$E(t) = \exp\left[-\left(\frac{t}{t^*}\right)^{1-n}\right]$$

where the parameter n indicates the degree of intermolecular coupling and $\tau^*$ is the characteristic segmental relaxation time. This last parameter depends on the coupling parameter and the longer of two relaxation times in the Hall Helfand relaxation function describing segmental relaxation of an isolated chain[21,22] ($\tau_o$):

**Equation 21**

$$t^* = \left[(1-n)w_c^{\,n} t_o\right]^{1/(1-n)}$$

where $1/\omega_c$ defines a characteristic time for the onset of intermolecular coupling. Once again, Equation 20 is not based on the chemistry of the material and to the author's knowledge no model enables systematic computations of n and $\omega_c$. The relaxation times are also still being discussed and other equations such as the empirical Vogel-Fulcher[21] can be used in Equation 20.

1.2.1.2.5 Other viscoelastic models

Several other models attempt to explain the rapid coordinate molecular motion happening in this region. Rouse[23], Bueche[24], Zimm[25] and Peticolas[26], developed the bead and spring model to qualitatively explain the viscoelastic behavior of the material in this region. The main concept is explained here following the approach detailed in Aklonis and McKnight[4]. Assuming that a long freely orienting molecule behaves like a Hokean spring, one may attempt to model the polymer molecule by a series of springs and beads (where the mass of the submolecule is concentrated). The restoring force on each of the beads resulting from a unidirectional perturbation can be written as:

**Equation 22**

$$f = \frac{3kT}{\overline{r^2}}\Delta X$$

where f is the restoring force, T is the temperature, k is the spring constant, r is the end-to-end distance of the Gaussian segment, and $\Delta X$ is the amount of spring distortion. The viscous force on each bead is:

**Equation 23**

$$f_i = r\frac{dX_i}{dt}$$

where ρ is the segmental friction factor. For the Zimm[25] model (based on Brownian motion and hydrodynamic shielding), the relaxation times ($\tau_p$) can be related to the steady-flow shear viscosity of the bulk polymer (η) by:

**Equation 24**

$$t_p = \frac{6h}{NkTp^2p^2}$$

with p a running index and N the density of molecules. Finally, the time-dependent shear stress relaxation modulus can be calculated using Equation 25:

**Equation 25**

$$G(t) = NkT\sum_{p=1}^{z} e^{-t/t_p}$$

However, this theory contains several discrepancies. In particular it gives poor agreement for studies of the bulk polymer: Williams, Ferry, and Landel[27] suggested the presence of two friction factors; this model would therefore describe a two-transition master curve. Different values of the segmental friction factor are used for relaxation times shorter than a critical relaxation time $\tau_c$ ($\rho_o$ ) and for longer times ($\rho_o$), leading to the following set of equations:

**Equation 26**

$$t_p = \frac{r_o a^2 z^2}{6p^2 kTp^2} \qquad t_p < t_c$$

**Equation 27**

$$t_p = \frac{r a^2 z^2}{6p^2 kTp^2} \qquad t_p \geq t_c$$

The segmental friction factors are related to the critical molecular weight for the onset of entanglement ($M_c$):

**Equation 28**

$$\log \frac{r}{r_o} = 2.4 \log \frac{M}{M_c}$$

Application of the model to specific polymers, such as polystyrene, lead to poor correlation with experimental data. Aklonis and McKnight[4] explain this discrepancy by the fact that the normal mode analysis is based upon the assumption that the distribution of relaxation times varies as $1/p^2$ (inflexibly implying that the slope of G(t) versus log(t) is –1/2).

*1.2.1.3 The rubbery state (region 3)*

At higher temperatures (just above glass transition) a plateau can be observed (Figure 1, region 3). This plateau corresponds to the long-range rubber elasticity. The plateau typically indicates a modulus equal to 3 MPa[1]. The length of the plateau increases with increasing molecular weight. The end of this plateau is characterized by the presence of a mixed region: the modulus drop becomes more pronounced but not as

steep as in the liquid flow region. Short times are characterized by the inability of the entanglements to relax (rubbery behavior) while long times allow coordinate movements of the molecular chains (liquid flow behavior)[1]. The concept of reptation was initially introduced by De Gennes[28]. The polymer chain relaxation in this region can be modeled by a wormlike (reptation) movement around obstacles or by a chain movement restricted inside a tube. The diffusion coefficient of the chain in the gel (D) is proportional to the molecular weight (M):

**Equation 29**

$$D \propto M^{-2}$$

Therefore the relaxation time is found to be proportional to the third power of the molecular weight. Finally, this model leads to a proportionality of the steady-state viscosity proportional to the third power (3.4 empirically[1]) of the molecular mass while the modulus and the compliance are independent of the molecular weight (the number of entanglements are large for each chain and can occur at constant intervals). This concept has been particularly successful and will be given a special attention in our analysis. If the polymer is linear, its modulus will decrease slowly with temperature. For semi-crystalline polymers, the height of the plateau will depend upon the percent of crystallinity of the material[29]. An increasing crystalline phase content will lead to a higher modulus because crystallites act like physical cross-links by tying the chains together. For cross-linked materials, the plateau will remain very flat at a height corresponding to[30]:

**Equation 30**

$$E = \frac{rRT}{M_c}$$

where $M_c$ is the molecular weight between cross-links.

*1.2.1.4 The liquid flow region (region 4)*

For linear polymers, very high temperatures can cause translations of whole polymer molecules between entanglements. The thermal energy becomes high enough to overcome local chain interactions and to promote molecular flow[4]. Ultimately, the

polymer becomes a viscous liquid and the modulus of the material drops dramatically. According to Sperling[1], the modulus of semi-crystalline polymers decreases quickly until it reaches the modulus of the corresponding amorphous material. Cross-linked polymers will not exhibit such a behavior, due to the presence of chemical primary bonds. The modulus of the polymer will remain constant until degradation.

The ideal equation governing the viscous flow can be written as[4]:

**Equation 31**

$$t = h\left(\frac{d\,g}{dt}\right)$$

Where $\eta$ is the viscosity, $\tau$ the shear stress, $\gamma$ the shear strain and t is time. When flow occurs directly measuring the modulus becomes difficult. However the viscosity of the polymer can be evaluated by different means (falling-ball viscometers, capillary viscometers, rotational viscometers. For high temperatures ($>T_g+100K$) the change of viscosity varies with temperature according to an Arrhenius law:

**Equation 32**

$$h = B\exp\left(\frac{\Delta H}{RT}\right)$$

where $\Delta H$ is the activation enthalpy of viscous flow. This equation can also be used for the material in its glassy state (Equation 2). However in the glass transition and rubbery regions, a simple relation can not be used[31]. As Tg is approached, the activation enthalpy "becomes dependent on the availability of a suitable hole for a segment to move into, rather than being representative of the potential energy barrier to rotation. This approach suggests that the jump frequency decreases when there is an increasing co-operative motion among the chains needed to produce holes"[31]. The activation energies strongly depend on the frequency of the experiment: 1900kJ mol-1 for the glass transition of amorphous peek at 0.1 Hz and 1250kJ mol-1 at 30Hz[23].

The processes governing molecular motions in this region are complex and belong to the domain of rheology[32,33]. Therefore we will not go further into the details of the flow region.

### *1.2.2 Molecular simulations*

The effect of temperature has been studied for some specific 100% crystalline polymers using molecular dynamics models. Some models, for example, have been developed for polyethylene[34,35]. The modulus of a crystalline fiber has been theoretically computed by Rasmussen[36] then modified by Shimanouchi et. al.[37] for the force constants. From simple geometrical and energy considerations[38], the modulus is found to be related to the bond length (l) and the bond angle (θ) by:

**Equation 33**

$$E = \frac{l\cos q}{A}\left(\frac{\cos^2 q}{k_l} + \frac{\sin^2 q}{4k_p}\right)^{-1}$$

For values of $k_l$ and $k_p$ determined from low-frequency Raman shifts of normal carbons, and for l=1.53 ? and ?=34°, the value is found to be $3.2.10^{11}$ Pa. From Equation 33, one can deduce that an increase in the θ angle will translate in an increase of modulus that agrees with the physics of the process (a higher packing efficiency will result in a higher modulus). However, the different parameters involved in this equation are not constant and depend strongly upon temperature.

The longitudinal modulus for 100% crystalline polyethylene can decrease above a certain temperature or remain unchanged depending on the lattice parameters of the crystallites. "The origin of these differences and the characteristic parameter which governs the temperature dependence of $E_1$ [longitudinal modulus] of polyethylene are not clear now"[34]. However, a model developed by Nishino et. al.[34] is relatively successful in fitting experimental data, and can predict a steep drop in modulus sometimes experimentally observed for polyethylene at elevated temperatures. Nishino's model is based upon the direct geometry of the molecule: in the kinked chain model, "two gauche conformations are introduced in the otherwise all-trans deformation"[34]. The main equation used in this model for the longitudinal modulus $E_1$ can be written as:

**Equation 34**

$$\frac{1}{E_1} = \frac{1 - X_k}{E_1^{\,o}} + \frac{X_k}{E_{kink}}$$

Where $E_1^{\,o}$ is $E_1$ at room temperature, $X_k$ is the amount of kink introduced, and $E_{kink}$ is the elastic modulus of the kinked portion.

More complex studies have been conducted on polypropylene crystallite by Lacks et al.[39,40,41]. Starting from Lennard-Jones[1] potentials and using a Monte Carlo simulation, the changes in the dimensions of the crystalline lattice can be successfully predicted (Lacks[39,40,41]). Therefore the elastic constants can be predicted with accuracy as a function of temperature.

A very small number of molecular dynamic simulations deal with the case of amorphous polymers. Rigby et. al.[42] reported the results of computer simluations of poly(ethylene oxide). Thermodynamic properties and cohesive properties were calculated for the amorphous polymer over extended ranges of at least 200K in temperature. The predicted densities were within 1% of the experimental data.

The case of semi-crystalline polymers is even more complex. The various theories for the molecular interpretation of the relaxation processes in semi-crystalline polymers were summarized by Boyd[43]. However, most of these models are only applicable to one given relaxation. The correlation between experimental data and the models derived from these theories was not found to be successful[43] for relaxations other than the glass transition.

Despite some success of this rigorous approach, molecular dynamics simulation studies are very specific and no effort has been made so far to generalize the different theories that closely depend on the nature of the polymer. The calculations involved are also very complex and are difficult to integrate into mechanical models.

### *1.2.3 Micromechanics*

#### *1.2.3.1 Tensile experiments*

Unidirectional fiber reinforced polymer matrix composites are often considered as "fiber controlled", i.e., the strength (X) of the composite in the fiber direction is directly proportional to the strength of the fibers[44], i.e.,

**Equation 35**

$$X_{fiber\,direction} = X_{fiber} V_{fiber}$$

where $V_{fiber}$ is the volume fraction of reinforcement.

The temperature dependence of the strength of the fibers is often negligible (e.g. carbon fibers). Therefore a very small number of studies deal with the influence of temperature on unidirectional carbon fiber reinforced polymer matrix composites. However, recent studies[45,46] have shown that the mechanical properties of a unidirectional composite can significantly vary with temperature in the fiber direction. The stiffness and strength of unidirectional AS4/PPS samples have been found to drop by 7% and by 20% respectively[45] over a 100°C range as illustrated by Figure 3 and Figure 4. Crews and McManus[46] model the degradation of the composite's strength by relating the degradation state $\alpha$ to the percentage of mass loss:

**Equation 36**

$$a = \frac{m_{initial} - m}{m_{initial} - m_{nonreactive\ fraction}}$$

The rate of degradation was calculated by:

**Equation 37**

$$\frac{\partial a}{\partial t} = k(1-a)^n \exp\left(-\frac{E}{RT}\right)$$

where k is the rate constant n is the reaction order and E an activation energy. These three values can be obtained via curve fitting. The modeling of the unidirectional strength was fairly successful but the unidirectional stiffness was assumed constant (and equal to the fibers' stiffness). Contradicting experimental results are shown in Figure 3 and Figure 4 from Walther[45]: the tensile stiffness and strength of unidirectional AS4/PPS exhibited a 7% and 20% drop respectively over a 130°C temperature range.

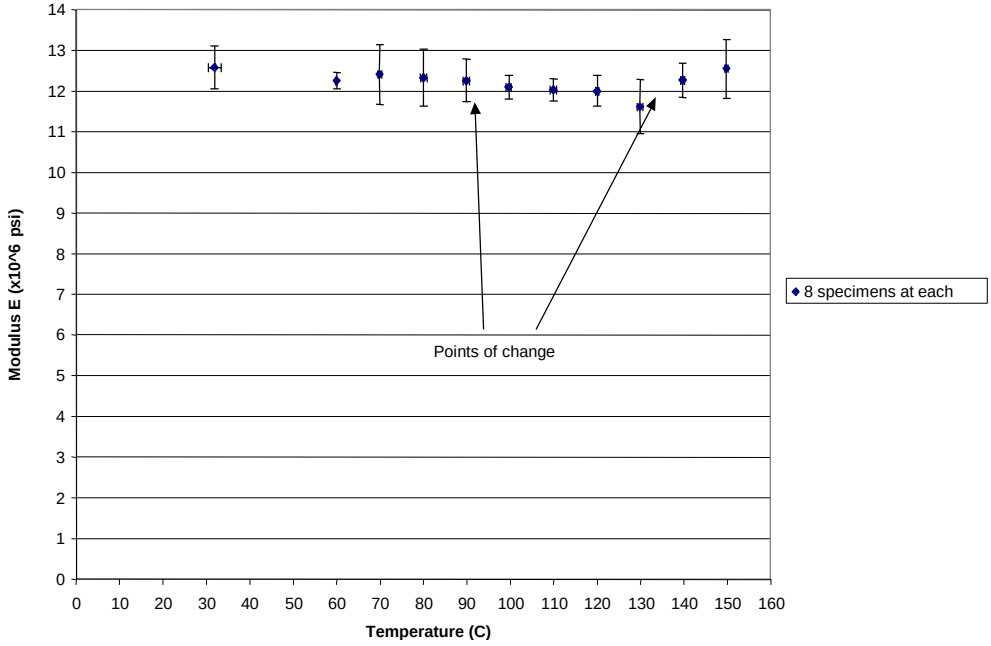


**Figure 3. Stiffness versus temperature for unidirectional AS4/PPS. From Walther[45]**

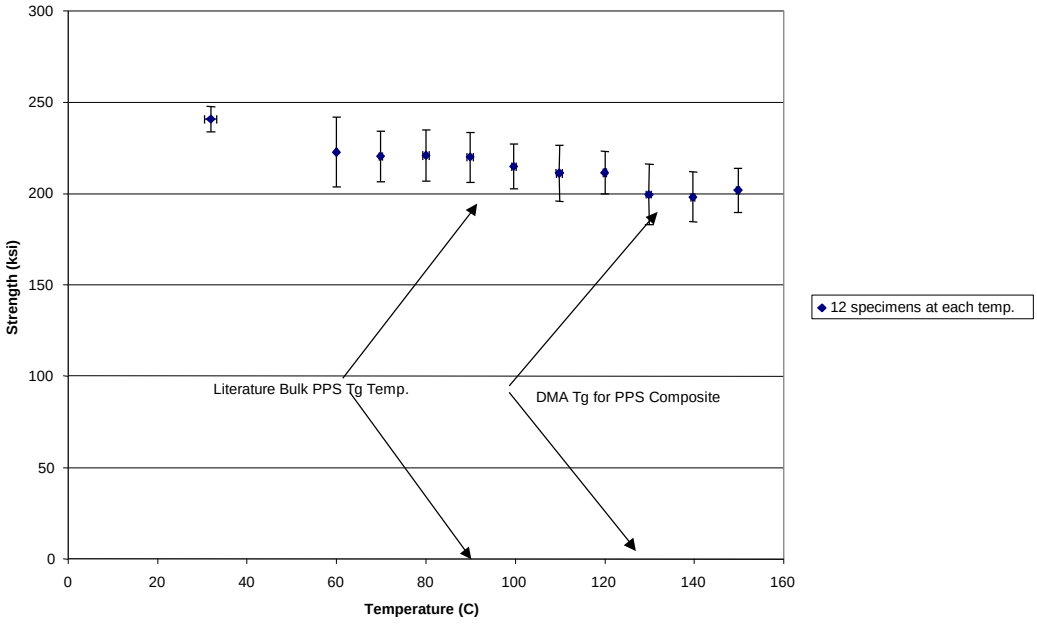


**Figure 4. Strength versus temperature for unidirectional AS4/PPS. From Walther[45]**

*1.2.3.2 Rule of mixtures*

The properties of composite materials can be calculated from the constituents' properties according to the well-known rule of mixtures[44]. In the longitudinal direction, the modulus $E_{11}$ can be related to the modulus of the matrix $E_m$, of the fibers $E_f$, and the volume fraction of fibers $V_f$ by:

**Equation 38**

$$E_{11} = V_f E_f + (1 - V_f) E_m$$

In the transverse direction, the modulus $E_{22}$ can be approximated by:

**Equation 39**

$$E_{22} = \frac{1}{\frac{V_f}{E_f} + \frac{1 - V_f}{Em}}$$

These equations assume a perfect bonding between the fiber and the matrix. These equations describe a two-phase model and do not consider the presence of an interface.

To better fit experimental data, the rule of mixtures has been modified to lead to the Halpin-Tsai equation[47] for the calculation of the transverse properties of the composite:

**Equation 40**

$$E_{22} = \frac{E_m (1 + chV_f)}{(1 - hV_f)}$$

with

**Equation 41**

$$h = \frac{((E_f / E_m) - 1)}{((E_f / E_m) + c)}$$

$\chi$ being an adjustable parameter.

*1.2.3.3 End-loaded bending stress-rupture*

The time and temperature dependent character of unidirectional polymer matrix composites has also been evidenced by end-loaded bending stress rupture experiments at elevated temperatures[48,49,50,51]. The life of bent AS4/PPS specimens was found to vary

tremendously with applied strain and temperature. To the author's knowledge, no model exists that allows us to predict the time to failure of such materials for any time and any strain level.

*1.2.3.4 Macromechanics*

On a macroscopic scale, the challenge is to predict the life of composites undergoing combined loads. The MRLife$^{TM}$ concept was introduced by Reifsnider and Stinchomb[52]. The remaining strength, used as a damage metric, can be calculated as a function of time and applied conditions. If a particular fraction of life at a two different load levels gives the same reduction in remaining strength then they are equivalent. "In addition, the remaining life at a second load level is given by the amount of generalized time required to reduce the remaining strength to the applied load level. In this way, the effect of several increments of loading my accounted for by adding their respective reductions in remaining strength"[53]. An explicit relationship between matrix stiffness and temperature could allow us to predict the changes in the stresses and life of composites under combined loads.

## 1.3 Objective

No general model was found in the literature that explicitly related the modulus of the polymer to the temperature. The goal of this study is to establish an explicit engineering relationship between stiffness and temperature that can be easily integrated into micromechanics models. This relationship can be applied to any polymer (thermosets, thermoplastics, amorphous, linear, semi-crystalline, cross-linked, low molecular weight, high molecular weight materials, etc) for the entire range of temperatures: from the glassy state to the flow region. This model will enable us to quantitatively describe the stiffness changes across the transition region (without making or testing the material) and to evaluate the overall composite performance through the entire temperature range. The feasibility of this approach will be demonstrated by studying some cases of interest.

# Chapter 2 Stiffness versus temperature predictions for polymers

## 2.1 Preliminary comments

We would like to adopt a more general approach than the existing theories listed in the literature review (section 1.2.1), to be able to describe the polymer behavior over the entire temperature spectrum, including the transitions, and to relate the mechanical response of the polymer to its microstructure. From a thermodynamical standpoint, one can relate the Gibbs energy G to the temperature T, the pressure P and the compressibility K[54] by:

**Equation 42**

$$\left[\frac{\partial^2 G}{\partial P^2}\right]_T = -K \cdot V$$

If we knew the form of the Gibbs free energy in the property transition regions, we could directly integrate Equation 42 to obtain an explicit relationship between modulus and temperature. To the author's knowledge, such a description of Gibbs energy for a polymer over the entire temperature range (glassy to flow) has not yet been established. For this reason, the present study introduces the concept of statistics of bond survival as a possible scheme to predict the temperature dependence of the modulus of any polymer.

The nature and magnitude of relaxation mechanisms in polymers vary as a function of various parameters. We can divide the parameters influencing the modulus of a polymer into two categories: intrinsic and extrinsic parameters. Examples of intrinsic parameters are the nature of the polymer (cross-linked, semi-crystalline, amorphous), the percent of crystallinity, the density, the molecular weight, the transition temperatures and the chemical structure. Examples of extrinsic parameters (experimental conditions) are strain and deformation state, strain rate and frequency, moisture, time and temperature. Variation of the extrinsic parameters can induce a variation of the intrinsic parameters. For example, a variation of straining temperature can induce a change in the percent of crystallinity of the material, modify the glass temperature of the polymer, and alter the

molecular conformation of the molecules. The different parameters previously stated are not independent and are often related. We will focus on the influence of temperature on the state of the polymer and try to integrate microstructure into the analysis. As molecular weight and crystallinity are the most widely studied in the literature among all of these parameters, we will focus on these two parameters. However our study can be extended to the case of crosslinked polymers.

In the following section, the molecular behavior of a typical polymer with temperature is summarized. The discussion focuses on the evolution of the states of the inter/intra-molecular bonds when the temperature changes. The statistics of the process are discussed and a scheme is established to enable the direct calculation of the elastic modulus of the polymer as a function of temperature. In section 2.3, analytical results are compared to experimental data excerpted from different sources in the literature. Results for various polymers exhibiting secondary relaxations and copolymers are shown. Our own experiments on various polymers are presented in section 2.4 and compared to the analytical predictions in section 2.5. Finally, the implications and the limits of this polymer model are discussed (section 2.6) before its application to the case of polymer matrix composites (Chapter 3).

## 2.2 Theoretical modeling

The well-known modulus versus temperature curve for a typical polymer exhibiting a secondary relaxation is illustrated by Figure 5. We chose to divide the master curve into 3 regions instead of 4 (Figure 1, section 1.2.1) because we will consider the number of relaxation phenomenon occurring rather than the number of distinct regions that can directly be observed on the characteristic mechanical response.

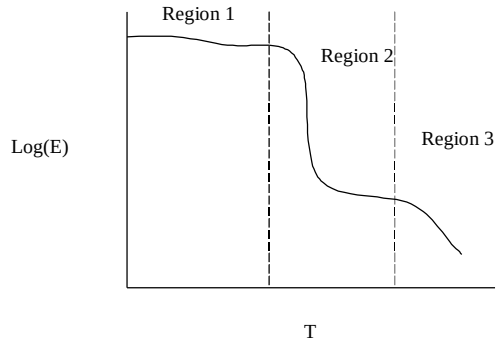


**Figure 5. Modulus versus temperature for a typical polymer**[55]

In order to establish a general engineering model, we will not detail the molecular motions that have been carefully reviewed in other studies cited in the literature review (section 1.2). We will rather focus on the behavior of the inter- and intra-molecular bonds, as discussed by Ashby[56]. The bonds in polymers can be divided into two major groups: the primary bonds and the secondary bonds. The first class includes the strong covalent intramolecular bonds. The dissociation energy of such bonds varies between 50 and 200 Kcal/mole[57,58]. Secondary bonds include weaker bonds, e.g., hydrogen bonds (dissociation energy[57,58]: 3-7 Kcal/mole), dipole interactions (1.5-3 Kcal/mole[57,58]), Van der Waals interactions (0.5-2 Kcal/mole[57,58], and ionic 10-20 Kcal/mole[57,58]). The two types of bonds are shown schematically in Figure 6.

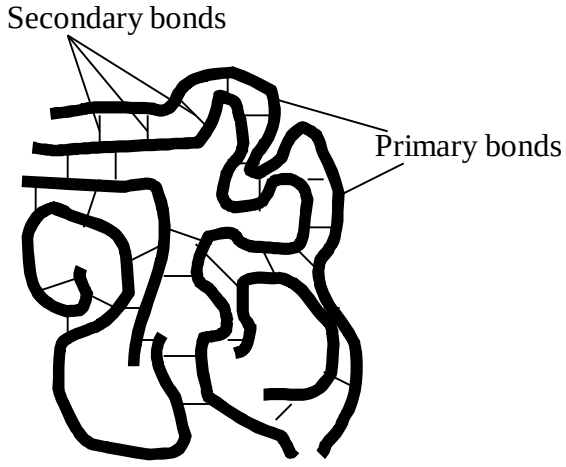


**Figure 6. Schematic of bonds in polymer materials**

Region 1, commonly referred as the glassy region, is characterized by a quasi-elastic behavior of the polymer. The modulus is constant over a wide range of temperatures and most of the bonds stretch without breaking. However, for some

polymers, the thermal energy is high enough to allow rotation of side groups. For this situation one (or several) secondary relaxations can be observed, characterized by a significant drop in the modulus. In this case, the secondary bonds must break to allow the side groups to rearrange. However the activation energy required for this very local movement is low, and these relaxations can occur at low temperatures (lower than the glass temperature).

The alpha transition, also referred as the glass transition, results in a dramatic drop in Young's modulus (region 2) followed by a plateau (rubbery region). In region 2, the molecules start sliding against each other[56]. However, the movement of the molecules is still restricted by the presence of entanglement, cross-links, crystallites, fillers, etc. The molecule can be thought as being trapped in a tube (the concept of reptation introduced by De Genne[28]), where the molecule can move in a snake-like fashion (Figure 7). In order to be able to reptate, the molecule needs to break secondary bonds (referred as "bond melting" by Ashby[56]) as in the case of the secondary relaxation, but over a large part of each molecule. However, in this region, some elastic parts still survive and the molecular chain will keep some memory of its original position. As temperature is further increased, all of the secondary bonds are broken and the molecules can move freely (unless crosslinks are present); the modulus of the polymer starts dropping again characterizing the viscous flow of Region 3.

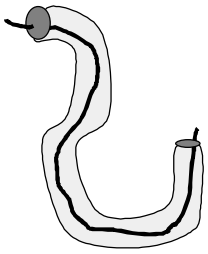

**Figure 7. Reptation**[55]

Spring and dashpot models lead us to discuss relaxation times as a representation of local behavior. The relationship between modulus and temperature is often written as:

**Equation 43**

$$E(t) = \sum_{i=1}^{N} E_i \exp\left(-t/t_i\right)$$

Equation 43 is a generalization of Equation 15 presented in section 1.2.1.2.3, where $\tau_i$ are the relaxation times for the different transitions. One can define the distribution function H as:

**Equation 44**

$$H(t) = tE(t)$$

Therefore, Equation 43 can be written as:

**Equation 45**

$$E(t) = \int_{-\infty}^{+\infty} H(t) \exp\left(-t/t\right) d(\ln t)$$

In the viscoelastic region, reptation is sometimes[56] modeled by an equation of the type:

**Equation 46**

$$E \propto \exp\left(-\frac{Q}{RT}\right)$$

where Q is the activation energy of the process. Such a Boltzman distribution denotes a random process, i.e. the bonds are breaking in an undetermined sequence, while Weibull statistics enables the description of interactive failure. Intuitively, when one bond breaks, the stresses in the other bonds are redistributed, and previous failure events have a non-negligible influence on the failure of the remaining bonds. Therefore, if we describe the process of secondary bond rupture, a Weibull distribution[59] would seem to be more appropriate than the Boltzman distribution of Equation 46. Let us first consider the beta transition. The mechanical response is driven by the motion of small chain segments (only a few monomers long). Considering the number and strength of the bonds involved in this relaxation process we can associate a Weibull coefficient $m_1$ to the beta relaxation. In this case Equation 45 becomes for the beta transition:

**Equation 47**

$$H_1^t(t) = \exp\left(-\left(\frac{t}{t_1}\right)^{m_1}\right)$$

or exchanging time for temperature[4] for instantaneous response and introducing a conversion constant:

**Equation 48**

$$H_1(T) = H_0^1 \exp\left(-\left(\frac{T}{b_1}\right)^{m_1}\right)$$

Where $\beta_1$ is the characteristic temperature (i.e. beta transition temperature) and $H_0^1$ a reference value for the beta transition (i.e. magnitude of the relaxation). For the following transitions (alpha, flow), the number of segments involved in the relaxation increases. For each relaxation, new Weibull coefficients related to the number of bond failures required for a given relaxation to occur and to the strength of the intermolecular bonds can be associated with the relaxation.

Finally, as we have different mechanisms occurring, we can sum the different components:

**Equation 49**

$$E = \sum_{i=1}^{N} H_i \exp\left(-\left(\frac{T}{T_{ref_i}}\right)^{m_i}\right)$$

In the present case, we will consider one to three transitions (1<N<3). The $H_i$ coefficients (magnitude of the transition step) can be obtained by different means. We can subtract the value of the material's stiffness before and after the transition, leading to Equation 50 (case of a material that does not undergo any transition prior to flowing), Equation 51 (material with two transitions, e.g., glass and flow) and Equation 52 (material undergoing three transitions, e.g., beta, glass and flow):

**Equation 50**

$$E = E_1 \exp\left(-\left(\frac{T}{T_3}\right)^{m_3}\right)$$

**Equation 51**

$$E = (E_1 - E_3)\exp\left(-\left(\frac{T}{T_2}\right)^{m_2}\right) + E_3\exp\left(-\left(\frac{T}{T_3}\right)^{m_3}\right)$$

**Equation 52**

$$E = (E_1 - E_2)\exp\left(-\left(\frac{T}{T_1}\right)^{m_1}\right) + (E_2 - E_3)\exp\left(-\left(\frac{T}{T_2}\right)^{m_2}\right) + E_3\exp\left(-\left(\frac{T}{T_3}\right)^{m_3}\right)$$

The $T_i$ (Figure 8) correspond to the temperatures at each transition (as given by the maximum of the peaks on the tangent delta versus temperature of a DMA curve, or by the inflection point of a DSC plot) in Kelvin. The remaining difficulty is for the flow region. In this first approach, we will not try to detail the behavior of the material in the flow region. We will only show the applicability of this approach to the flow region by using flow temperatures given in the literature.

The $E_i$ (Figure 8) represent the intantaneous stiffness of the material at the beginning of each plateau or region. $E_1$ is the instantaneous modulus at very low temperature of the polymer, $E_2$ is the instantaneous modulus immediately after the beta transition, $E_3$ is the instantaneous stiffness at the beginning of the rubbery plateau. A reliable experiment leading to consistent values for stiffness measurements is the ultrasound method. The modulus obtained in this fashion corresponds to a uniaxial experiment performed at very high strain rate or cyclic frequency. The drops in modulus in the different regions ($H_i$) represent the "importance" of the relaxation processes. These values depend on the chemistry of the polymer (stiffness of the backbone), molecular weight, crystallinity and degree of crosslinking. An increased crystallinity will produce only a slight increase in the glassy state stiffness but can produce a large rise in the value of the modulus of the rubbery plateau. Therefore, the magnitude of the glass transition step will decrease as the crystallinity is increased. The transition temperatures will also be increased as the crystallites impede the rearrangement of the molecules under the applied stress. Increased molecular weight and cross-linking will stiffen the material to a lesser extent.

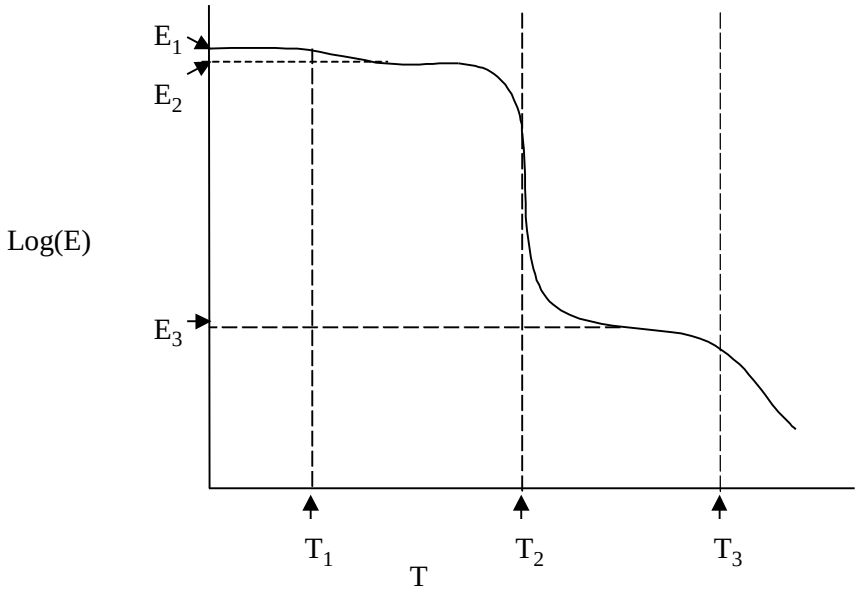


**Figure 8. Inputs of Equation 52. Schematic.**

The last parameters ($m_i$) are Weibull moduli, corresponding to the statistics of the bond breakage. To allow rotations of side groups for the secondary relaxations, the strength of the bonds that need to be broken depends on the relative position of the side group to the other molecular chain. Therefore there will be a wide distribution of bond strengths and we would expect *m* to be small. Reptation involves translation of the main chains. If the material is very homogenous (narrow distribution of bond strengths) as in the case of amorphous materials, we would expect *m* to be very large. However, this parameter depends on the degree of impediment of the molecular motion (cross-linking, molecular weight and crystallinity…). If the movement of the molecular chains is severely restricted at precise locations (by crosslinking, etc), we would expect *m* to be low (approaching a Boltzman distribution). For crosslinked materials, the slope of the drop in the viscous flow region will decrease with increasing degree of crosslinking. For heavily crosslinked materials, the flow region can even disappear.

One might question the form of these equations, thinking that these equations would fit any curve, given that we fix the height of the plateau and the temperatures. However, we must first remember that these equations have a physical basis: in order for the relaxations to occur, the secondary bonds need to break. In polymers, there is a

distribution of these molecular bond strengths. The number of segments involved also varies from one relaxation to the other (always increases as the temperature increases). Finally when one of the secondary bonds break, other bonds are influenced (in the manner that broken fibers interact with unbroken fibers in a fiber bundle). Secondly, the reference temperatures and moduli can be independently measured or calculated. The reference temperatures correspond to the inflection point of the transitions and not the temperature ($T_i$) corresponding to the plateau's height ($E_i$). Therefore we are not forcing the value of the modulus at any temperature. The reader might also notice the similarity of the mathematical form of Equation 52 with the KWW equation (Equation 20). These two equations are stretched exponentials. However the differences can be noted as follow:

- Equation 52 is based on physical considerations (bond failure)
- Equation 52 refers to measurable, well defined physical quantities (transition temperatures and instantaneous stiffnesses)
- Equation 52 is applicable on the entire temperature range (up to flow of the polymer).

## 2.3 Feasibility

To validate the feasibility of this approach some data from the literature were taken at random. We will not get into the detail of the fitting in this section. The parameters will be discussed in great detail in section 2.6.

### *2.3.1 Literature data*

For details on how the experimental results were obtained, we will refer to the different authors.

Equation 52 was first used with PMMA. The experimental data from Ashby[56] were taken on the amorphous linear polymer.

The second set of experimental data used was the variations of the loss shear modulus of PVDC from Schmieder and Wolf[60].

The storage modulus (measured at 1 Hz) of a high molar mass Thiophene-based poly(arylene ether ketone) from Brennan et. al.[61]: poly(1,4-BFB, BisA), $M_n$=20 000 g.mol$^{-1}$ was also compared to our model.

The model was also compared to the experimental data for the loss modulus of a polyethylene oxide-salt complex $(PEO)_{0.82}(Fe(SCN)_3)_{0.18}$ measured at 3 Hz ($M_w$=600 000) from Bartellota et. al.[62].

Two poly(ether ether ketone)-polymethylsiloxane block copolymers were also studied using data from Risch et. al.[63]. PEEK-PSX copolymers were obtained from PEEK block with a number average of 4900 (5K) and PSX block number-average molecular weights of 3200 (3K) and 4900 (5K). In this case we used Equation 52 to model the presence of two glass transitions.

The results are shown in Figure 9, Figure 10, Figure 11, Figure 12, Figure 13, and Figure 14. $m_1$, $m_2$, and $m_3$ were chosen to obtain the best fit of the overall shape of the master curve (therefore we are not trying to minimize the error). Surprisingly the $m_1$, $m_2$, and $m_3$ coefficients were consistently equal to 5, 20, 20 respectively for all materials except for the Thiophene-based poly(arylene ether ketone), where $m_2$=40 and $m_3$ = 1 due to the high degree of cross-linking (infinitely broad bond strengths distribution).

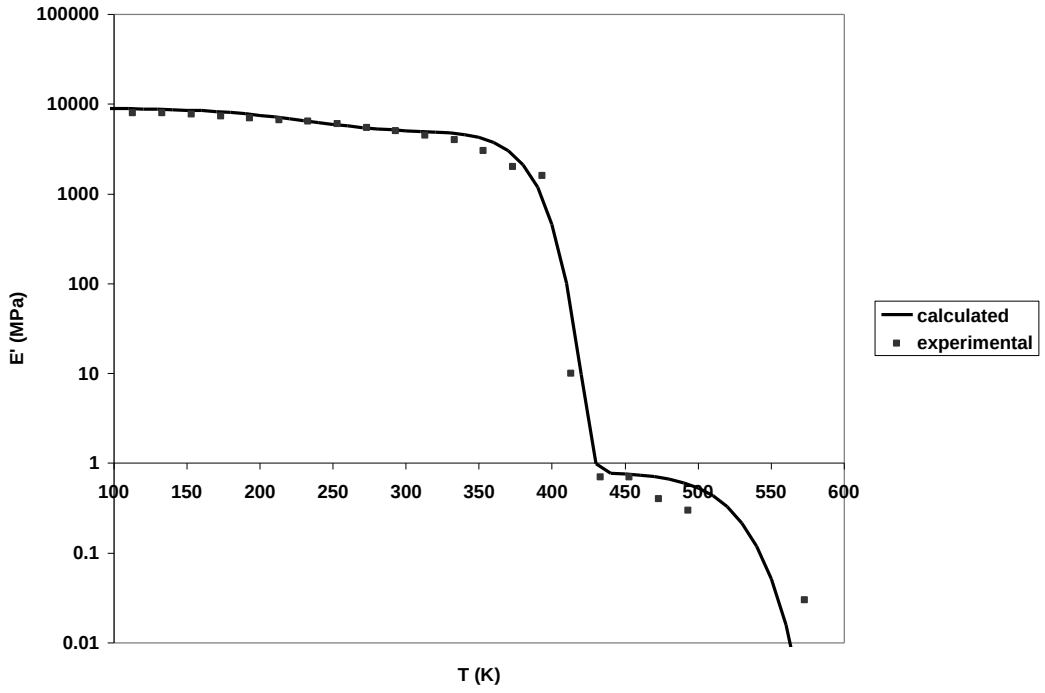


**Figure 9. PMMA**[56]

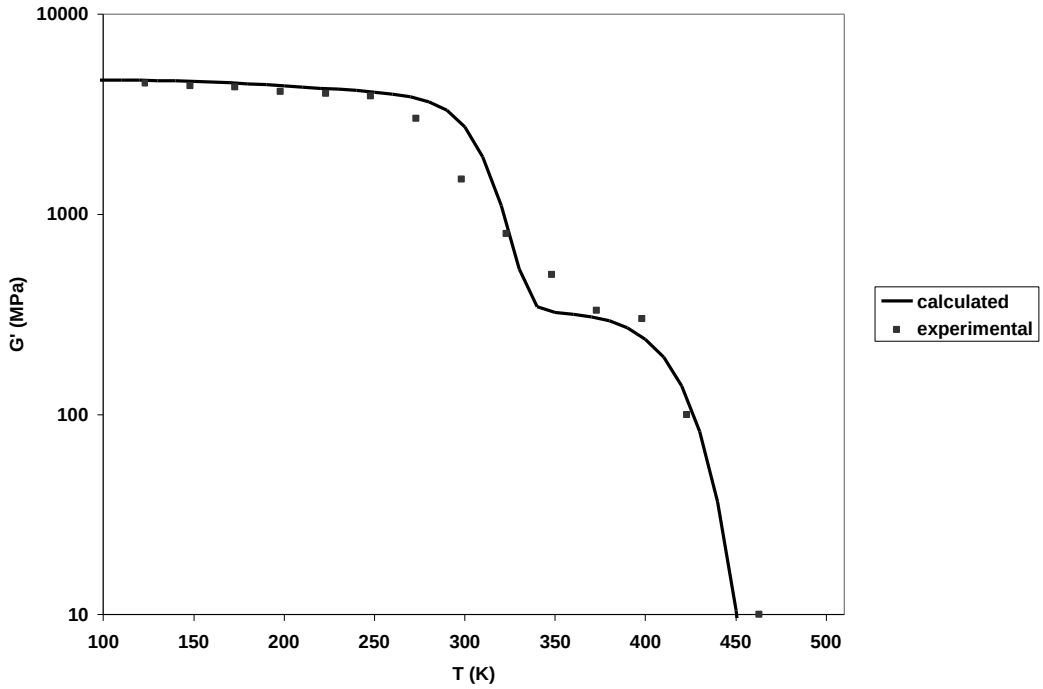


**Figure 10. PVDC**[60]

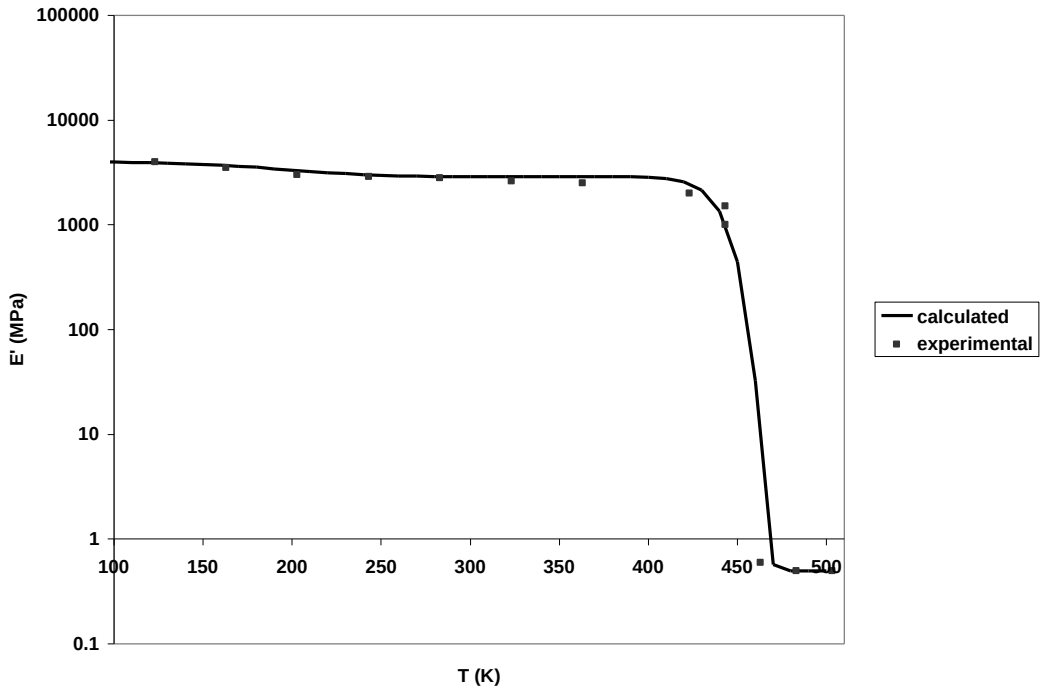


**Figure 11. Poly(1,4-BFB, Bis A)**[61]

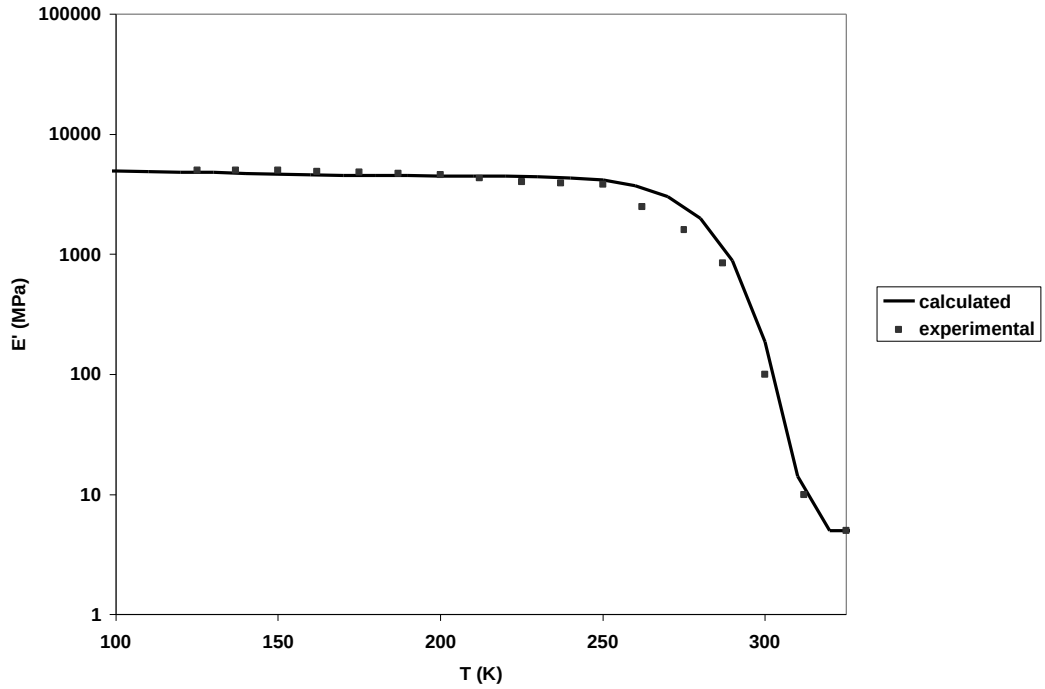


**Figure 12. $(PEO)_{0.82}(Fe(SCN)_3)_{0.18}$**[62]

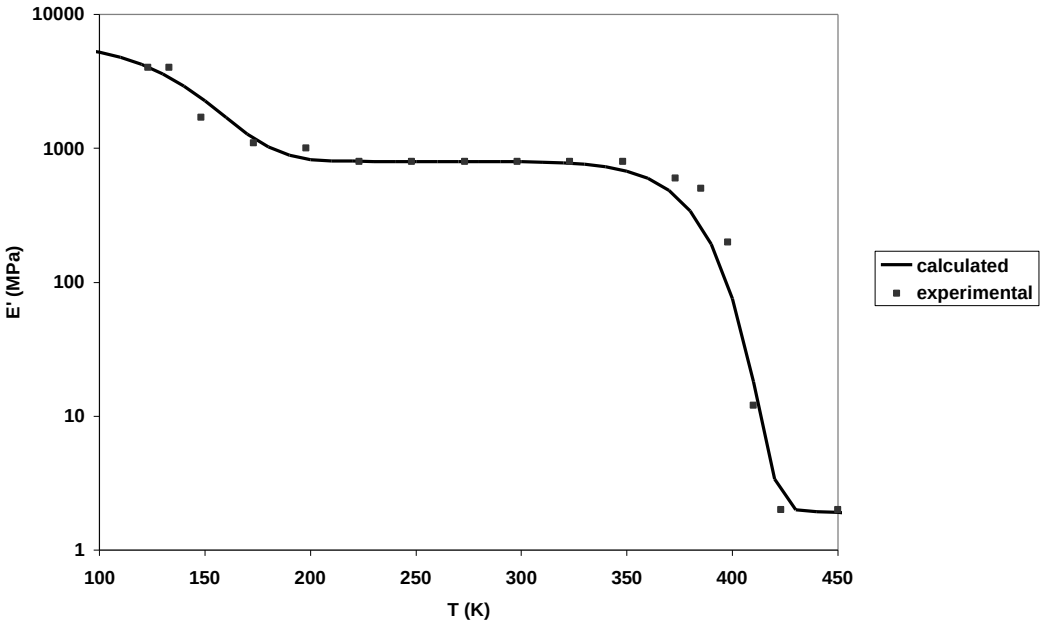


**Figure 13. PEEK(5K)PSX(3K)**[63]

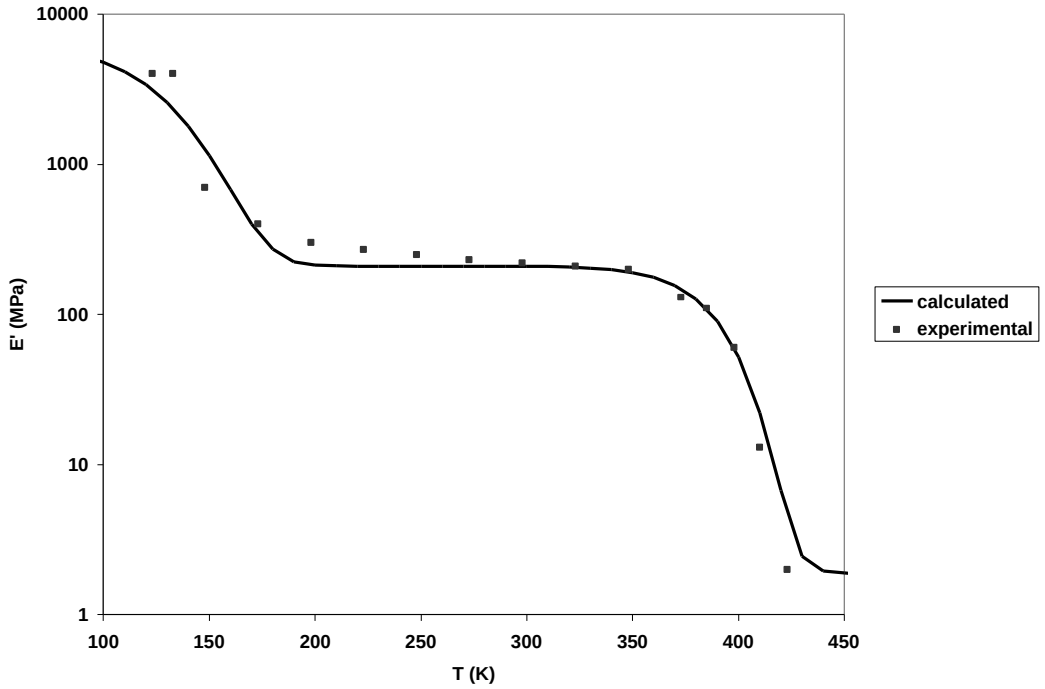


**Figure 14. PEEKt(5K)PSX(5K)**[63]

### *2.3.2 Discussion*

The model fits the data successfully even for extreme temperatures. Equation (6) seems to describe the behavior of polymers with temperature. However, in order to use Equation 50, Equation 51 and Equation 52 in a systematic manner, we need to be able to compute all the parameters or to obtain them from independent experiments.

The biggest challenge is to understand the significance of the $m_1$, $m_2$, and $m_3$ parameters in equations. The $m_1$ and $m_2$ coefficients were consistently equal to 20 for all the two-transition polymers described in section 2.3.1. Intuitively, it seems that the $m_2$ and $m_3$ coefficients must be related to the degree of impediment of the molecular motion in the different regions, i.e., crystallinity, crosslinking, molecular weight… We can observe the fact that the $m_2$ coefficient drives the slope of the glass transition. The $m_2$ coefficient, almost constant for our previous cases, might be related to the breadth of the molecular weight distribution or to the percent of crystallinity. However it is difficult to obtain details on the chemical properties of the materials used in the experiments excerpted from the literature.

Further experiments were required to determine if these coefficients remain constant for polymers with very different properties (i.e., molecular weight and crystallinity). Careful systematic experiments were performed and are presented in section 2.4.

## 2.4 Experimental work

The purpose of the experimental study was to establish if the model could be applied to various commercial polymers, thermoset and thermoplastic with very different properties (molecular weight and crystallinity).

### *2.4.1 Material selection*

The different polymers were arbitrarily chosen. Three thermoplastics: Poly(methyl methacrylate) (PMMA), Poly(ether ether ketone) (PEEK) and Poly(phenylene sulfide) (PPS), one elastomer: Poly(butadiene), and one composite: AS4/PPS were selected.

#### *2.4.1.1 PMMA*

PMMA is a linear amorphous thermoplastic.

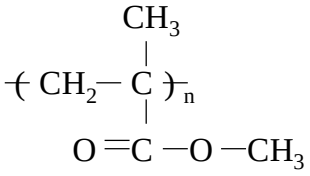

**Figure 15. PMMA molecule**

This polymer is characterized by its transparency. The glass transition for the polymer is 105°C (221°F), the heat deflection temperature is between 74°C (167°F) and 100°C (212°F)[64]. This polymer exhibits the presence of secondary relaxations. The beta transition occurs around 0°C[56]. The density of the polymer is 1.188 g/cm$^3$ [1]. Commercial PMMA (plexiglas) typically has high molecular weights with broad

distributions. High molecular weight material can be obtained by pouring low-molecular-weight polymer and monomer into a mold. During polymerization autoacceleration occurs (the molecular weight increases dramatically owing to a suppression of the termination step)[64]. The molecular weight may be over $10^6$ g/mole.

Two different grades of plexiglas were obtained from Rohm and Haas. Little information could be obtained from the company concerning the molecular details of the material.

- plexiglas MC: Low molecular weight PMMA Mw around 150 000 g/mole. Traces of ethyl acrylate (EA) can be found in the polymer.
- plexiglas G: very high molecular weight PMMA (around $10^6$ g/mole).

The samples were supplied as 10.15x10.15 mm (4"x 4") plates with a thickness of 3 mm.

*2.4.1.2 PEEK*

PEEK is a linear aromatic polymer.

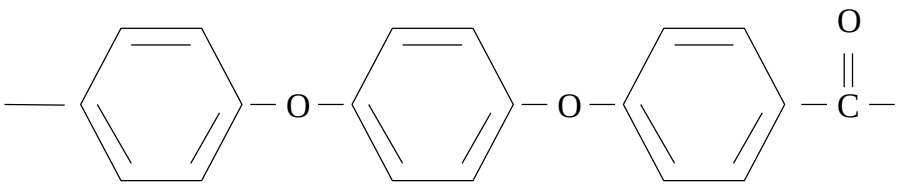

**Figure 16. PEEK molecule**

From the literature[65], the glass transition is 143°C (289F) and the melting point is 334°C (633F). PEEK also has a beta relaxation around –30°C for the crystallized material[7]. The temperature of maximum crystallization rate from melt is 256°C (493F) and 185°C (365F) from glass. The specific gravity of the amorphous phase is 1.265 and 1.320 for the fully crystalline state.

Different grades of PEEK were supplied by Victrex:

- 150 G: with a melt viscosity (MV) of 0.150 kN.s.m$^{-2}$.
- 450 G: with a melt viscosity (MV) of 0.450 kN.s.m$^{-2}$.

The molecular weight (as given by light scattering) can be calculated from these values[66]:

**Equation 53**

$$\log_{10}(MV) = -15.06 + 3.21\log_{10}(Mw)$$

- 150G: Mw = 27 000 g/mole.
- 450G: Mw = 38 000 g/mole.

The material was supplied as pellets.

*2.4.1.3 PPS*

PPS is a linear polymer.

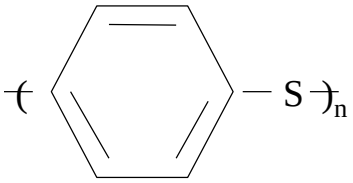

**Figure 17. PPS molecule**

The melting as found in the literature[65] is of 285°C. The temperature at maximum crystallization rate is around 230°C from melt and 130°C from glass. The glass temperature is around 85°C.

Two grades of PPS were supplied by Phillips Petroleum Company: PR09 and PR10X2. According to Phillips[67], the typical molecular weight for the grade PR09 is 65,000-70,000 g/mole. PR10X2 has a lower molecular weight, around 55,000 to 65,000 g/mole. These numbers were determined by exclusion chromatography. The supplier claimed that scatter of the results is typical and stated that these numbers can vary by as much as 10%. The PPS from Phillips was in a powder form.

Another grade of PPS (0320 PO) was supplied by Fortron Celanese. The molecular weight for this material could not be determined. The PPS Celanese was received as pellets.

For the last two thermoplastics, one must keep in mind that the molecular weights are approximate, considering the difficulties in measuring the molecular weight of these two materials (due to the poor solubility). Also the different temperatures are just indications and vary depending on the molecular weight and crystallinity of the polymers.

*2.4.1.4 Rubber*

Polybutadiene is a an elastomer with the following molecular structure:

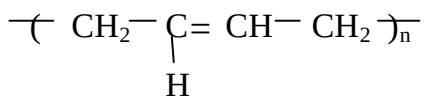

**Figure 18. Polybutadiene molecule**

Polybutadiene was supplied by Goodyear in three different grades: 50,000 g/mol, 100,000 g/mol and 240,000 g/mol. The first molecular weight was too low and the material exhibited flow even at room temperature. Two samples of filled 100,000g/mol polybutadiene were also provided: brw30 filled with 23% of carbon black by weight and brw60, filled with 37.5% of carbon black by weight.

*2.4.1.5 Composite*

AS4/PPS material was provided by Baycomp. The volume fraction of fibers was 50% in volume. The material was supplied as a 0.5" x 0.04" rolled tape.

### *2.4.2 Materials processing and samples preparation*

Unlike PMMA and polybutadiene that did not need any further modification before testing, PPS and PEEK needed to be molded into a plate form in order to be tested.

*2.4.2.1 PEEK processing*

The first attempt to process the PEEK was done by compression molding of the pellets of PEEK 150 following the instructions from Victrex[68]. The mold was charged with 102% of the theoretical weight of the polymer required to form the component (225 grams). The 152 x 152 mm (6"x 6") mold was then placed in a hot press at 400°C (752°F) for 20 minutes. Then the heat and pressure loads were disabled and the mold was left on the lower plate of the press until room temperature was reached. At this point we realized that most of the material had escaped from the mold, leaving only an extremely thin film of material on the bottom of the mold.

The second attempt to process the PEEK was made by injection molding. Robert Young (Department of Chemical Engineering, Virginia Tech) injected the polymer

according to the procedure described in the literature[69]: the polymer was injected using an Arburg Allrounder Model 221-55-250 in a 75 x 80 x 1.6 mm mold. The injection pressure was held constant at 5 MPA, the holding pressure at 10 MPa and the flow at 10 $cm^3/s$. The temperature varied from the "solids conveying zone to the nozzle": Zone 1: 380°C, Zone 2: 400°C, Zone 3: 400°C, and Zone 4: 400°C. The temperature of the mold was 200°C.

*2.4.2.2 PPS processing*

The PPS Celanese was received as pellets. The PPS from Phillips was received as powder straight from the reactor. The material was pelletized in an extruder at around 290°C. The PPS powders were injection molded following the same procedure than in the PEEK case. The temperatures of the different zones were Zone 1: 250°C, Zone 2: 290°C, Zone 3: 280°C, and Zone 4: 270°C. The mold was at 140°C.

*2.4.2.3 Samples manufacturing*

For each material, the samples were prepared by cutting the plates using a band saw in dry conditions. The final samples had a size of 25.4 x 6.35 mm (1" x ¼") for the DMA samples ("long samples"). Some additional smaller samples were also cut off the plates for DSC testing ("short samples"). The thickness of the final samples was approximately 3 mm for the PMMA and 1.5 mm for PEEK and PPS.

### *2.4.3 Crystallinity modifications*

Each semi crystalline material: PEEK 150, PEEK 450, PPS PR9, PPS PR10, PPS Celanese, AS4/PPS composite, was tested as received. Then various heat treatments were applied to the samples in order to modify the crystallinity of the various polymers.

*2.4.3.1 Obtaining the maximum crystallinity of the material*

2.4.3.1.1 PEEK

In order for the material to reach a higher crystallinity level, the specimens were annealed at elevated temperatures for relatively long times (PEEK and PPS are fast crystallizers). The PEEK samples (2 long samples, 1 short sample) of each grade were placed on an Aluminum plate in an oven (Fisher Scientific Isotemp Vacuum Oven Model 282A) at 180°C (crystallization temperature) for one hour.

2.4.3.1.2 PPS

Similarly, the PPS samples were placed in the oven at 130°C for 1 to 3 hours (for Celanese material).

2.4.3.1.3 Composite

The composite was placed at 130°C for 3 hours in the oven.

*2.4.3.2 Obtaining amorphous material*

The process of obtaining amorphous polymers is more complex because of the fact that PEEK and PPS are very fast crystallizers. Several attempts were necessary to achieve satisfactory results. One must also note that very high temperatures are involved and the use of a tube furnace (Labline model 4305, inner diameter: 78 mm) was necessary. The temperature was recorded by a thermocouple twisted on a screw attached to the aluminum plate. The temperature in the oven varies by 5°C when compared to the set point of the furnace.

2.4.3.2.1 PPS

The first attempts were made on the PPS Celanese material. The first sample was placed on a 10 mm thick plate coated with release agent (TFE release agent for preheated molds, Miller Stephenson, MS-136 N(CO2)), then placed in the furnace at 330°C for approximately two minutes then quenched in ice water. This sample was found to have a crystallinity similar to the fully crystalline material. We assume that the specimen did

not have sufficient time to reach the melting temperature. In fact it was observed that the specimen even crystallized more.

A second specimen was placed in the oven for 1 hour 30 minutes at a temperature of 330°C then quenched in ice water. The sample maintained its overall shape. However the corners of the sample became a bit rounder and some small bubbles (less than 0.5mm diameter) appeared on the side that was in contact with the aluminum plate. The specimen thus obtained was dark brown and transparent.

As the feasibility of the process was established, the specimens were treated in a more systematic way. For each type of PPS, 2 long specimens and 1 short specimen were placed on the 75 x 38 x 10 mm aluminum plate (the preheated mold was previously sprayed with release agent) at a temperature of 330°C for more that 1 hour then quenched in ice water (Figure 19 and Figure 20).

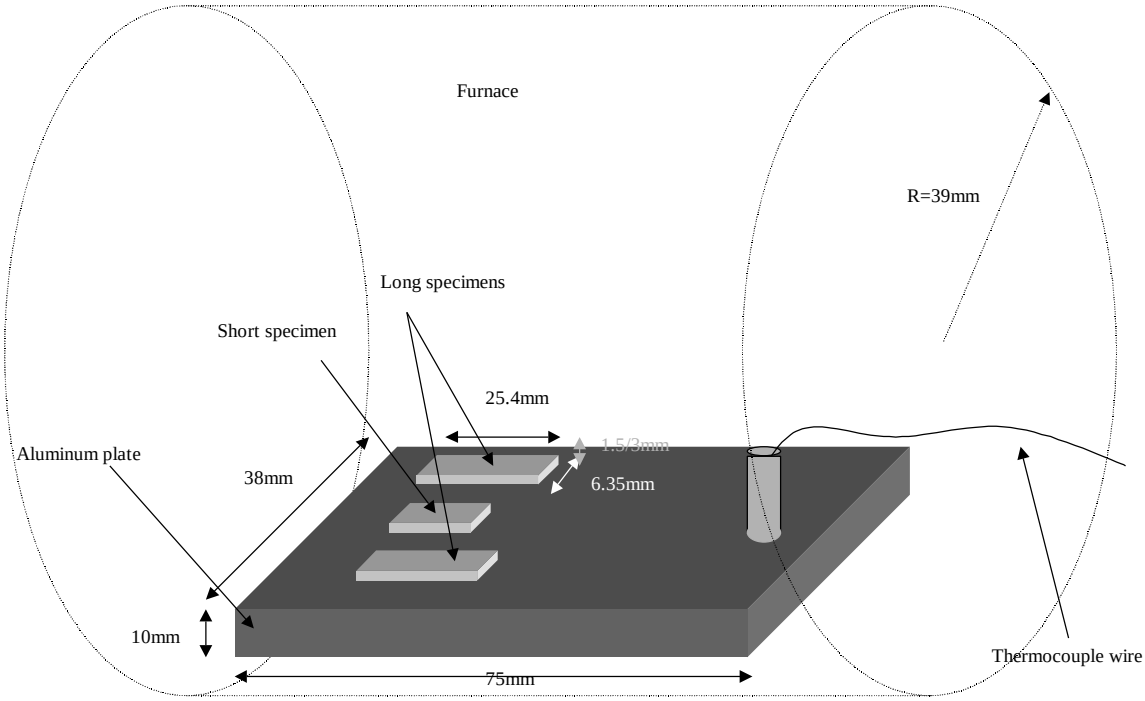


**Figure 19. Specimens in the tube furnace**

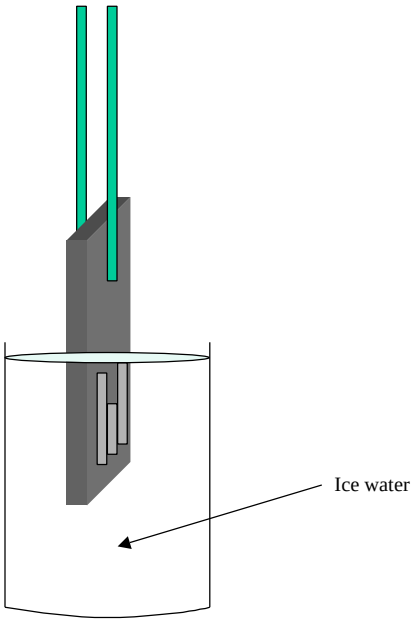


**Figure 20. Quenching of the samples**

The exact procedure for each sample and observations can be summarized as follows:

-PPS Celanese: the samples were left in the oven at 330°C for 1 hour 30 minutes then quenched in ice water. The resulting samples had a regular shape, small bubbles on one side (contact with Aluminum plate) and are very transparent.

-PPS PR09: the samples were left for 1 hour at 330°C then quenched ice water. The resulting specimens maintained most of their original shape but exhibited a large number of bubbles on one side (up to 2 mm diameter). The samples were transparent.

-PPS PR10: the samples were placed in the oven for 2 hours at 330°C and then quenched in ice water. As the specimens were still opaque, they were placed back in the furnace at a slightly higher temperature (340°C) for one hour. The specimens were quenched again in ice water. The specimens retained their shape, no bubbles appeared on the surface of the samples, and the color turned very dark brown but remained opaque.

2.4.3.2.2 PEEK

Using the same methods, the crystallinity of the PEEK samples were modified:

-PEEK 150: the 3 samples were placed on the aluminum plate and in the tube furnace at 365°C for 1 hour 30 minutes, then quenched in ice water. Due to the low molecular weight, the samples flowed. They were reshaped to their original shape by using the alternating saw. The samples obtained in this fashion are a little bit smaller and wider than the original samples. The samples were mainly transparent. However, one could note the presence of darker spots (clouds).

-PEEK 450: the changes for the higher molecular weight PEEK were more difficult to perform, due to the facts that the material retains its chemical and mechanical integrity at higher temperatures. The first samples were placed in the furnace at 365°C for one our then taken out of the furnace. At this point it was clear that the specimens did not melt entirely. The specimens were placed in the oven for two extra hours. The furnace went up to 455°C and the specimens were burnt. Three more samples were placed in the oven at an intermediate temperature: 365°C for two hours. At this temperature and in air, it is possible for some crosslinks to form. The resulting samples retained their shapes, did not exhibit the presence of bubbles, and were fully transparent.

*2.4.3.3 Obtaining intermediate crystallinity*

2.4.3.3.1 PEEK

Intermediate crystallinity values were obtained for PEEK by placing the amorphous specimens in the oven at 180°C for one to two minutes then taking them out of the oven, and letting them cool at room temperature. PEEK is a very fast crystallizer. If the specimen was in the oven for more than 2 minutes, the sample became highly crystallized. But one minute was just enough for the specimen to get to temperature, and the percent of crystallinity was very low.

2.4.3.3.2 PPS

Intermediate crystallinity samples were obtained similarly: the specimen was put in the oven at 130°C for 2 minutes then taken out and let cool down at room temperature.

2.4.3.3.3 Composite

The composite was taken as received and placed in the oven at 130°C for two minutes.

### *2.4.4 Material characterization*

Two methods were used to measure the crystallinity of the different samples.

#### *2.4.4.1 Density measurements*

Density measurements were performed on the different polymers as received and on the highly crystallized samples. Density measurements are only valid if the material is gas free. To check if our samples met this requirement, the material as received and highly crystallized was X-rayed. This method would detect the presence of macroscopic voids. It can be observed in Figure 21 that the material seems to be adequate for this testing.

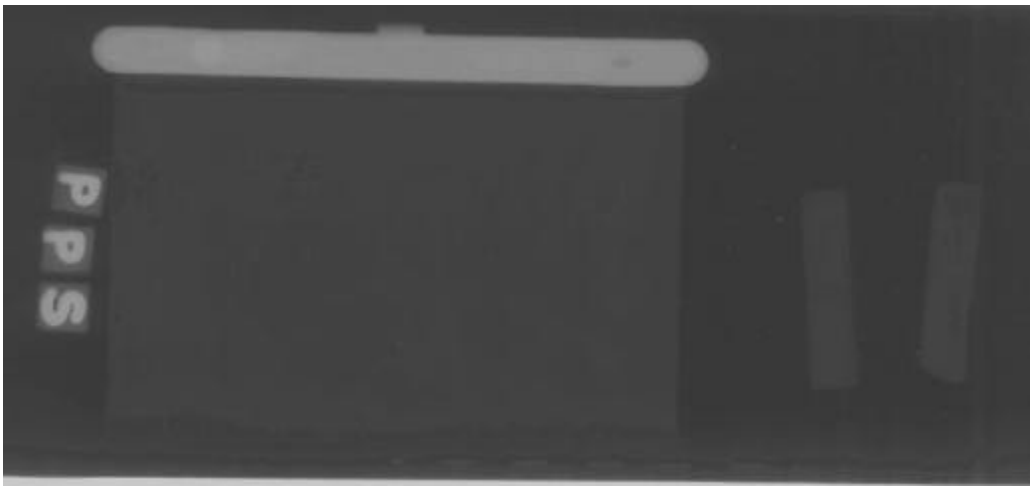


**Figure 21. X-rays of PPS Celanese. Plate as received and two specimens after 1 hour at 130°C**

The specimens were first weighed in air then in distilled water, making sure that no air bubbles were trapped around the specimen. The temperature of the water was recorded at the beginning and at the end of the series of measurements. The procedure

set up using a Mettler Toledo kit for AT/AG and PG/PG-S/PR balances is shown in Figure 22.

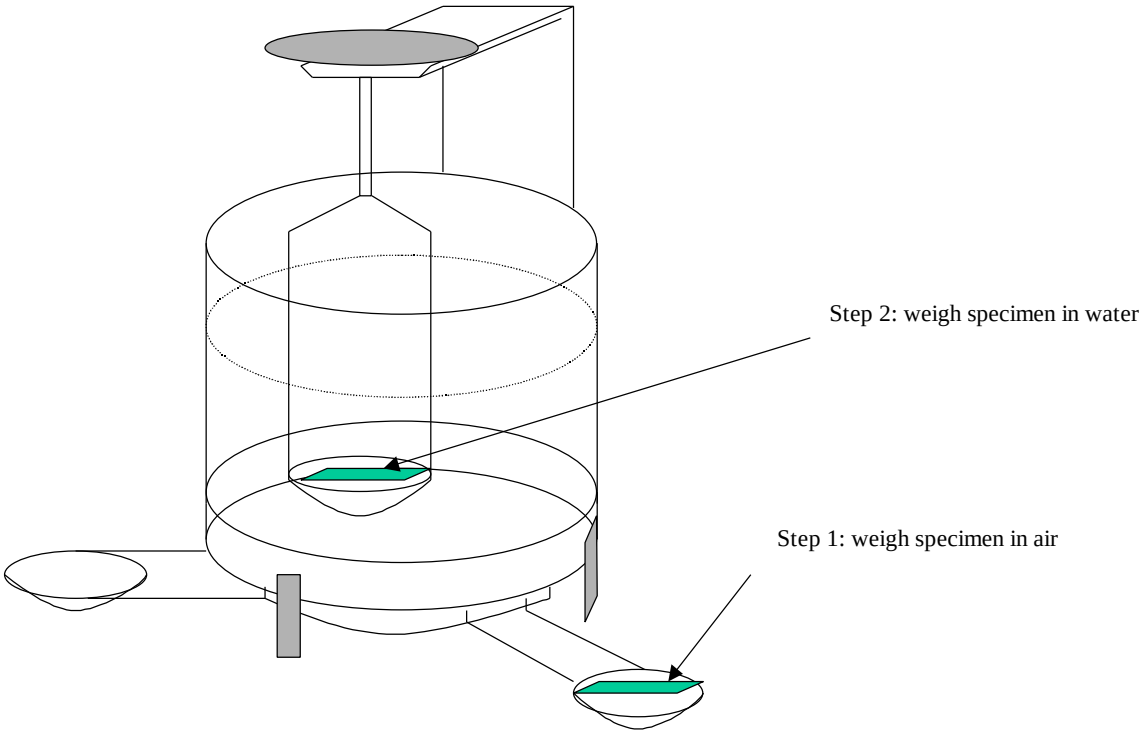


**Figure 22. Density measurements apparatus**

Three measurements were performed per sample. The measurements in air were very reproducible. The measurements in water show an error smaller than 1%.
The density is determined by Archimedes's principle:

**Equation 54**

$$\rho = \frac{A}{A - B} \times \rho_o$$

Where $\rho$ is the density of the sample, A is the mass of the sample in air, B is the apparent mass in distilled water, and $\rho_o$ is the density of the distilled water. This last quantity varies with temperature[70].

Table 1 summarizes the different measurements at a temperature varying between 26.5°C and 27°C. The error indicated in Table 1 is the absolute error ($Max_{i=1,3}(abs(d_i - d_{av}))$). To verify the results, the density of the PMMA G sample was

also measured. The density of this amorphous polymer was found equal to 1.181. In the literature[1] the reported density is 1.188 (relative error $\frac{d_{theory} - d_{experimental}}{d_{theory}} \times 100$ of 0.6%).

**Table 1. Density Measurements**

| Specimen | In air (g) (average) | In water (g) (average) | Calculated density (g/cc) |
|---|---|---|---|
| PPMA G as received | 0.360 | 0.0570 | 1.184 ± 0.003 |
| PPS Celanese as received | 0.264 | 0.0673 | 1.338 ± 0.005 |
| PPS Celanese annealed | 0.263 | 0.0679 | 1.344 ± 0.003 |
| PPS PR09 as received | 0.308 | 0.0792 | 1.341 ± 0.003 |
| PPS PR09 annealed | 0.299 | 0.0782 | 1.348 ± 0.005 |
| PPS PR10 as received | 0.414 | 0.103 | 1.328 ± 0.001 |
| PPS PR10 annealed | 0.419 | 0.108 | 1.343 ± 0.004 |
| PEEK 150 as received | 0.292 | 0.0676 | 1.296 ± 0.006 |
| PEEK 150 annealed | 0.277 | 0.0638 | 1.296 ± 0.003 |
| PEEK 450 as received | 0.301 | 0.0675 | 1.284 ± 0.003 |
| PEEK 450 annealed | 0.279 | 0.0631 | 1.289 ± 0.006 |

The crystallinity content can be calculated according to the following rule of mixtures:

**Equation 55**

$$d_{sample} = (1-x)d_{amorphous} + xd_{100\%crystalline}$$

where d refers to the density and x is the percent of crystallinity present in the polymer samples. For our material systems, the following typical values from the literature were used:

- PPS: $d_{amorphous}$[71] = 1.32
- PPS: $d_{crystalline}$[71] = 1.43
- PEEK: $d_{amorphous}$[72] = 1.263
- PEEK: $d_{crystalline}$[72] = 1.4

However these values can vary significantly depending upon the crystallization conditions[76,73]. The corresponding crystallinity contents were calculated and are summarized in the graph of Figure 23. The specimens as received seem to have a

crystallinity very close to the annealed samples except for the PPS PR10 samples. This result is logical considering the fact that the temperatures of the injection molding process were chosen in order to maximize the crystallinity of the polymers.

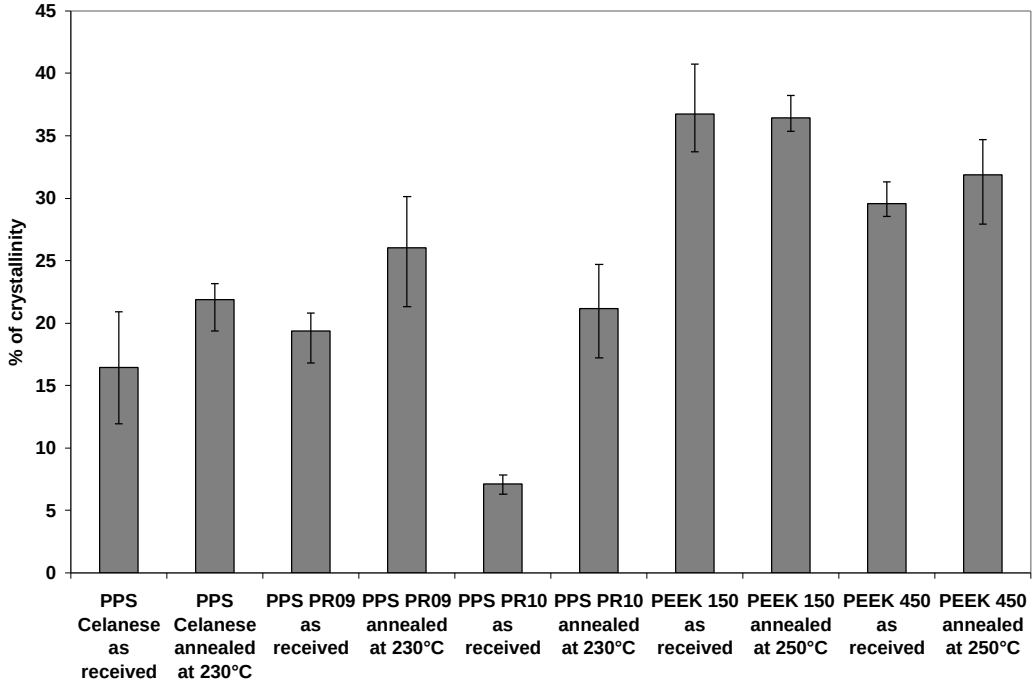


**Figure 23. Crystallinity contents**

The advantage of the crystallinity determination via density measurements is that it is a non-destructive test. Also the determination is done on the exact same sample that will be mechanically tested. However, this method could not be used for the amorphous samples due to the presence of air bubbles in the material. Furthermore, some of these results seemed strange intuitively (i.e. PPS PR10) and the crystallinity contents are low for highly crystallized polymers. A source of error can be that we assume a two-phase polymer when using Equation 55. We also rely on the values of the amorphous and crystalline phase densities found in the literature. These might be different for our materials and crystallization conditions. All the samples have not been scanned and we suspect the presence of air bubbles in some of the samples.

*2.4.4.2 DSC*

In order to evaluate the crystallinity of all the samples, including the amorphous and intermediate crystallinity samples, and to validate the density measurements, Dynamic Scanning Calorimetry (DSC) experiments were performed. Unfortunately, this type of testing is a destructive evaluation: the measurements were performed on the short specimens that were heated and quenched at the same time than the long specimens for DMA.

The DSC used for these experiments was a DuPont DSC model 910. Measuring crystallinity via DSC is a delicate process and a careful calibration of the equipment was necessary and can be described as follows.

2.4.4.2.1 Calibration procedure

The DSC was first balanced with two empty pans, and a straight baseline was obtained. Three DSC were run on Indium sample. The melting enthalpy and melting point of this metal is well know ($\Delta H$ = 28 J/g, Tm = 156°C)[74]. The experimental melting temperature and enthalpy were recorded for 3 different testing rates: 10°C/min, 20°C/min and 30°C/min. The melting temperature increased with heating rate in a linear manner (Figure 24). The enthalpy measurements remained almost constant and equal to 25.7 at 20°C/min, showing an error of 2.3 J/g (~10%) when compared to the theoretical value for Indium.

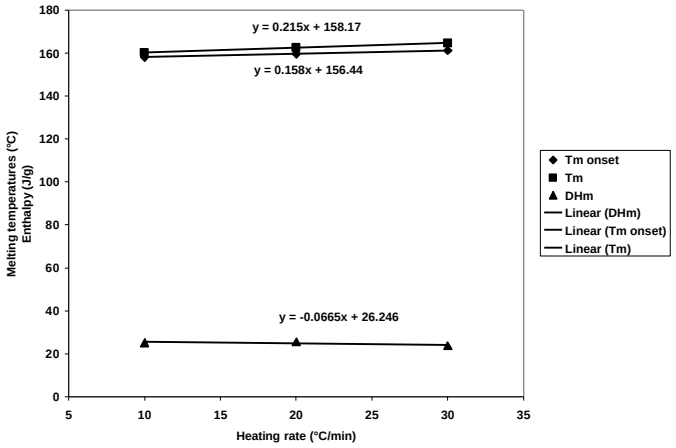


**Figure 24. Calibration curves**

Several of our specimens exhibited two peaks: one endotherm during crystallization and one exotherm during melting. The enthalpy of a transition is dependent on temperature. To get the crystallinity of the material, we need to know the enthalpy variations with temperature.

From thermodynamics[75] we know that:

**Equation 56**

$$\Delta H_f(T) = \Delta H_f(T_{ref}) + \int_{T_{ref}}^{T} \Delta C_p dT$$

The valued of $\Delta H_f(T_{ref})$ can be found in the literature for PEEK (160 $J.g^{-1}$ at 663 K)[76] and for PPS (111.6 $J.g^{-1}$ at 553 K)[77]. The variation of $C_p$ with temperature was obtained by molecular group additivity[13].

For PPS we find:

**Equation 57**

$$\Delta H(T) = -175.86 + 0.8188T - 0.00054T^2$$

For PEEK we find:

**Equation 58**

$$\Delta H(T) = -243.15 + 0.9336T - 0.000491T^2$$

The crystallinity can be calculated from Equation 59.

**Equation 59**

$$X\% = \frac{\Delta H(T_f) - \Delta H(T_c)}{\Delta H_{100\% crystalline}} \cdot 100$$

The DSC measurements for crystallinity purposes are not very accurate for the following reasons:

-the DSC was giving an initial error on the Indium sample during calibration

-the measure of the enthalpy depends on our choice of the starting and ending point of the peak, necessary to measure the area underneath the peak

-only a small piece of a sample was tested. This precise piece was not the one that will be tested in the DMA. If the samples are heterogeneous, the results will not be exact.

Another source of error is the theoretical value for the melting enthalpy. Disagreement on the theoretical values for PEEK and PPS are common in the literature.

However, the DSC measurement will give an approximation of the amount of crystallinity in the material. It is recommended to consider the calculated values as indicators of the relative differences from one sample to another (rather than considering the absolute values).

2.4.4.2.2 DSC Results

DSC of all the specimens was performed at 20°C/min (standard heating rate to minimize molecular rearrangement). The DSC results are summarized in Table 2.

**Table 2. Crystallinity measurements**

| Material | Tc (K) | Tm (K) | ΔHc measured (J/g) | ΔHm measured (J/g) | Crystallinity via DSC (%) | Crystallinity via density (%) |
|---|---|---|---|---|---|---|
| PPS Celanese amorphous | 413 | 561 | 22 | 39 | 2 | |
| PPS Celanese intermediate | 432 | 561 | 5 | 42 | 30 | |
| PPS Celanese as received | | 536 | | 38 | 36 | 17 |
| PPS PR09 amorphous | 413 | 561 | 22 | 38 | 2 | |
| PPS PR09 intermediate | 410 | 558 | 15 | 49 | 21 | |
| PPS PR09 as received | | 557 | | 59 | 52 | 20 |
| PPS PR10 amorphous | 427 | 547 | 5 | 19 | 10 | |
| PPS PR10 intermediate | 441 | 546 | 89 | 28 | 15 | |
| PPS PR10 as received | 403 | 560 | 5 | 62 | 47 | 7 |
| PPS PR10 annealed | | 561 | | 43 | 38 | |
| PPScomposite asreceived | 409 | 556 | 6 | 13 | 2 | |
| PPS composite annealed | | 556 | | 31 | 28 | |
| PEEK 150 amorphous | 453 | 620 | 22 | 38 | -2 | |
| PEEK 150 intermediate | 458 | 624 | 10 | 27 | 5 | |
| PEEK 150 as received | | 624 | | 36 | 24 | 37 |
| PEEK 450 amorphous | 456 | 617 | 21 | 35 | -2 | |
| PEEK 450 intermediate | 450 | 620 | 13 | 33 | 5 | |
| PEEK 450 as received | | 619 | | 36 | 24 | 29 |

As can be observed, the crystallinity results are very different when obtained by density measurements and DSC. Several reasons for this discrepancy have already been suggested. We will consider the DSC measurement in our analysis because we need values for all our samples. The crystallinity contents seem a little high for PPS as received (typical crystallinity of 30%)[77], but are still acceptable. The transparent samples also lead to crystallinities close to zero (the negative values are close to zero, and will be considered as null).

As previously indicated, intermediate crystallinity contents were difficult to obtain, as PEEK crystallizes very fast (3 minutes at 180°C result in a highly crystallized material and 1 minute leads to very low crystallinity contents). For the two PEEK samples, the crystallinities for the intermediate samples are very low. We will later discover that DMA of these specimens will lead to results too close to the amorphous samples. For this reason, another scheme was used to obtain results on intermediate crystallinity values. The intermediate sample that will be used later was obtained by running a DMA up to melting at 2°C/min then cooling down the specimen in air. The same sample was then placed again in the DMA. Due to this process, no crystallinity was measured for these samples.

### *2.4.5 Summary of the samples and properties*

The samples and their properties of interest are summarized in Table 3.

**Table 3. Summary of the samples**

| Material | Molecular weight (g/mol) | Crystallinity (%) |
|---|---|---|
| PMMA MC | 150 000 | 0 |
| PMMA G | $10^6$ | 0 |
| PPS Celanese amorphous | ? | 2 |
| PPS Celanese intermediate | ? | 30 |
| PPS Celanese as received | ? | 36 |
| PPS PR09 amorphous | 65 000-70 000 | 2 |
| PPS PR09 intermediate | 65 000-70 000 | 21 |
| PPS PR09 as received | 65 000-70 000 | 52 |
| PPS PR10 amorphous | 55 000-65 000 | 10 |
| PPS PR10 intermediate | 55 000-65 000 | 15 |
| PPS PR10 as received | 55 000-65 000 | 47 |
| PPS PR10 annealed | 55 000-65 000 | 38 |
| PPS composite as received | ? | 2 |
| PPS composite annealed | ? | 28 |
| PEEK 150 amorphous | 27 000 | 0 |
| PEEK 150 intermediate | 27 000 | ? |
| PEEK 150 as received | 27 000 | 24 |
| PEEK 450 amorphous | 38 000 | 0 |
| PEEK 450 intermediate | 38 000 | ? |
| PEEK 450 as received | 38 000 | 24 |
| PB 240 000 unfilled | 240 000 | |
| PB 100 000 unfilled | 100 000 | |
| PB 100 000 brw30 | 100 000 | 23% carbon black (by weight) |
| PB 100 000 brw60 | 100 000 | 37.5% carbon black (by weight) |

We will keep in mind that the crystallinity and molecular weight measurements are extremely difficult for PEEK and PPS. The above values will be considered as indications for trends and not absolute values.

### *2.4.6 DMA*

Dynamic Mechanical Analysis was performed by Polymer Solutions (Blacksburg, VA) on the different samples on a Polymer Laboratory MkII dynamic thermal analyzer (DMTA, DMA). DMA experiments are based on the measurement of the storage modulus E' and the loss modulus E'' (or the loss tangent, tan d): a sinusoidal stress is applied at various frequencies, and the stresses and strains are recorded as temperature increases. Due to the viscoelastic nature of the material, the sinusoidal strain lags the stress by a phase angle (d) which is a measure of viscoelastic damping. In the present case, the deformation geometry was a single cantilever as illustrated in Figure 25.

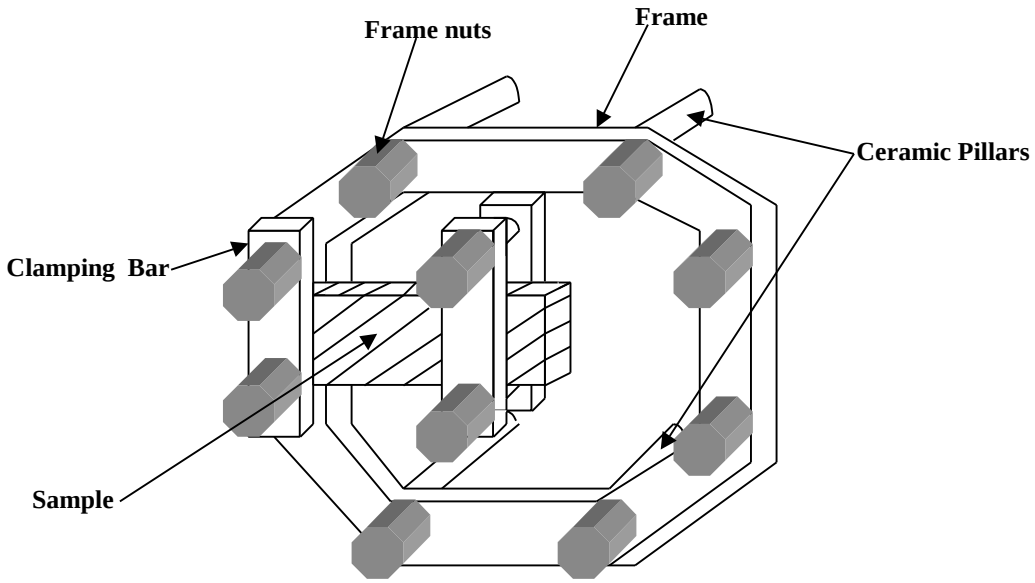


**Figure 25. Single cantilever sample arrangement**

Each sample was tested from −100°C up to flow of the material at different frequencies: 50 Hz, 20 Hz, 10 Hz, 5 Hz and 1 Hz. Tangent delta and elastic modulus were recorded in bending as a function of temperature. The samples were tested at a heating rate of 2°C/min. We will not deal in the present paper with rate effects. The results at 20 Hz were arbitrarily chosen and are shown in section 2.5.

## 2.5 DMA results and model validation

### *2.5.1 Varying the crystallinities*

For the two thermoplastics (PEEK and PPS) and the composite it is possible to study the influence of crystallinity on the parameters used in Equation 50, Equation 51, and Equation 52.

#### *2.5.1.1 PPS*

##### 2.5.1.1.1 PPS Celanese

The experimental results and theoretical fit are shown in Figure 26 for the amorphous material, the intermediate crystallinity and the sample as received. As the specimen "as received" was not fully crystallized, a sample was left in the oven at 130°C for several hours. The crystallinity content increased 6%, but the effect on the DMA is not significant. It seems that above a given crystallinity content the results of the DMA remain almost constant. Similar experiments on the other materials showed the same trend. The results of the DMA for the different samples of PPS show the trend expected from the literature: the magnitude of the stiffness drops during the transition increases with a decreasing amount of crystallinity in the material. All the curves meet after the melting point of PPS Celanese (540K). The melting and flow regions are not distinct. The material starts flowing immediately after the melting temperature. The amorphous sample exhibits a rise in modulus immediately after the glass transition, due to the fact that the material reaches the crystallization temperature. The rate of the testing is slow (2°C/min) and therefore the material is allowed to recrystallize. Consequently, the model was only applied to the section of the curve located before the crystallization temperature.

No secondary transition could be observed. Therefore Equation 51 was used to model the behavior. The necessary parameters are the heights of the glassy and rubbery plateaus and the transition temperatures (glass transition and melting-flow as indicated by the DSC or tan delta). We also require the two Weibull moduli associated with the different transitions. All these parameters are summarized in Table 4. The glass transition temperature increases slightly with increasing crystallinity. The glass

temperature varies between 97°C (amorphous) and 112°C (crystallized). The flow temperature is hard to define from our experimental results and the temperature chosen was the beginning of the final drop.

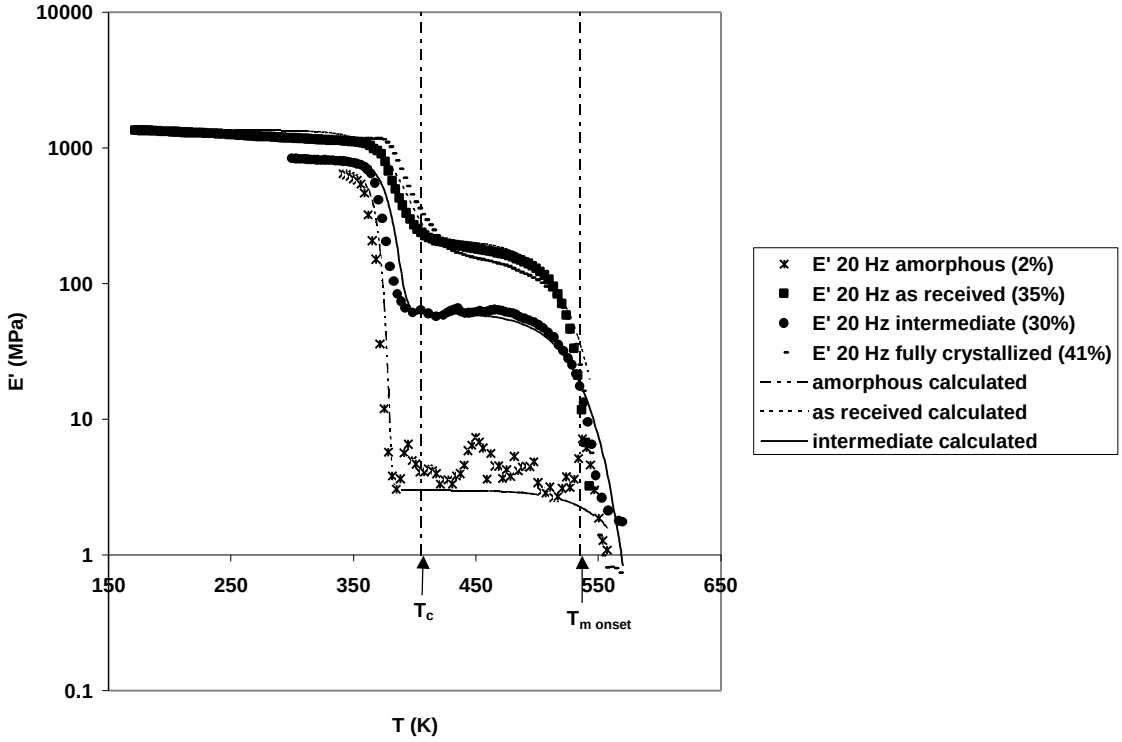


**Figure 26. Experimental and theoretical results for various crystallinities of PPS Celanese**

**Table 4. Parameters for PPS Celanese**

| Material | $T_2$ (K) | $T_3$ (K) | $E_2$ (MPa) | $E_3$ (MPa) | $m_2$ | $m_3$ |
|---|---|---|---|---|---|---|
| PPS Celanese amorphous | 370 | 520 | 646 | 3 | 60 | 20 |
| PPS Celanese intermediate | 380 | 530 | 832 | 61 | 40 | 20 |
| PPS Celanese as received | 385 | 570 | 1348 | 212 | 20 | 20 |

2.5.1.1.2 PPS PR09

The results for the PPS PR09 samples are summarized in Table 5 and Figure 27. The intermediate crystallinity content is low and we can observe recrystallization for the amorphous sample as well as for the intermediate sample.

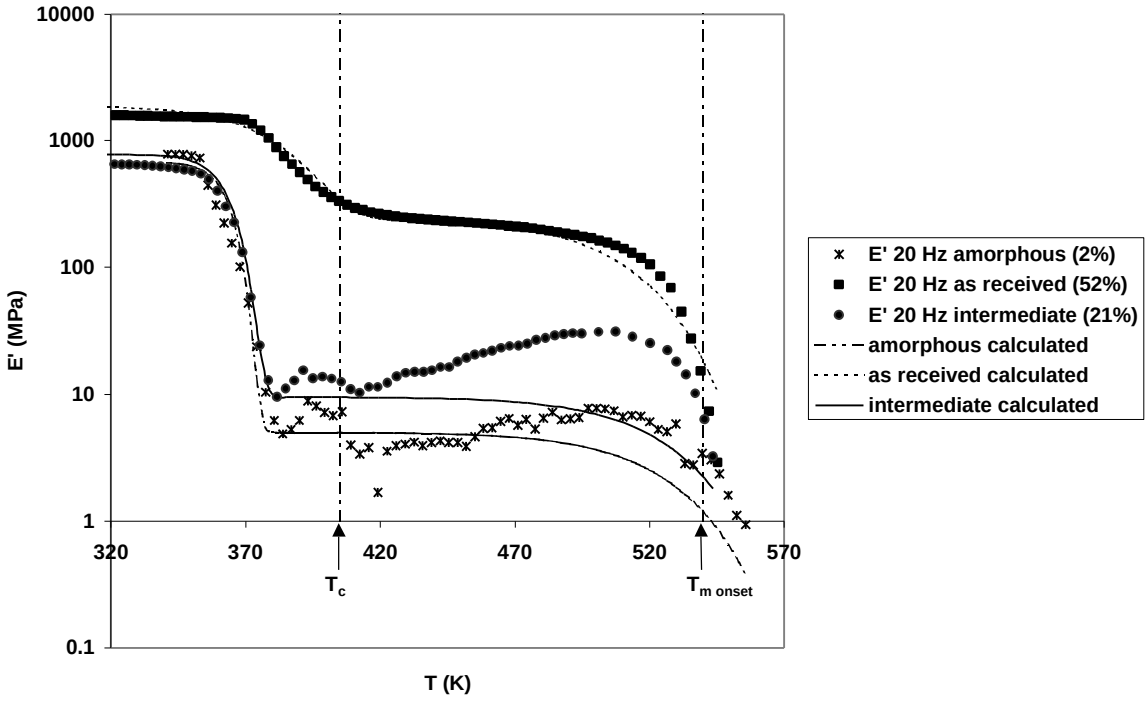


**Figure 27. Experimental and theoretical results for various crystallinities of PPS PR09**

**Table 5. Parameters for PPS PR09**

| Material | $T_2$ (K) | $T_3$ (K) | $E_2$ (MPa) | $E_3$ (MPa) | $m_2$ | $m_3$ |
|---|---|---|---|---|---|---|
| PPS PR09 amorphous | 365 | 530 | 682 | 5 | 60 | 20 |
| PPS PR09 intermediate | 365 | 530 | 780 | 9.5 | 50 | 20 |
| PPS PR09 as received | 385 | 515 | 1875 | 240 | 20 | 20 |

2.5.1.1.3 PPS PR10

The PR10 samples were also studied. However, during the experiments, strange behavior of the material indicates the presence of impurity in this sample (the material was very difficult to melt, a fully transparent material could not be obtained…). Intermediate samples with low crystallinity contents could not be obtained due to a very fast crystallization of the material. Two samples with crystallinity 25% and 38% were tested. The two curves superimpose perfectly and are very close to the material as received (47%). This corroborates the idea that a threshold value for the crystallinity content exists above which the mechanical response of the polymer does not vary significantly. In the glass transition region, the behavior of the material as received is also surprising: the drop is very steep and a bump immediately follows. This, again, can be explained by the presence of impurities in the polymer. The different results are shown in Figure 28 and Table 6.

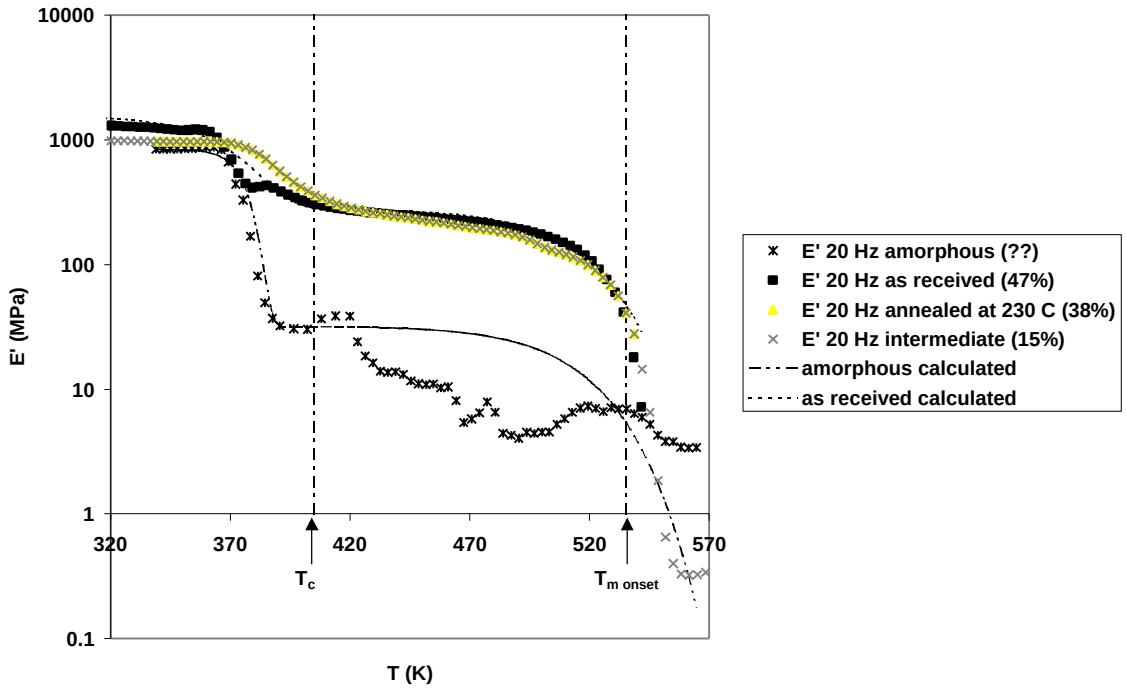


**Figure 28. Experimental and theoretical results for various crystallinities of PPS PR10**

**Table 6. Parameters for PPS PR10**

| Material | $T_2$ (K) | $T_3$ (K) | $E_2$ (MPa) | $E_3$ (MPa) | $m_2$ | $m_3$ |
|---|---|---|---|---|---|---|
| PPS PR10 amorphous | 373 | 520 | 841 | 32 | 60 | 20 |
| PPS PR10 as received | 373 | 520 | 1534 | 280 | 20 | 20 |

*2.5.1.2 PEEK*

2.5.1.2.1 PEEK 150

A similar approach was used for the different crystallinities of the PEEK 150 samples (amorphous, intermediate, as received). PEEK exhibits the presence of a secondary relaxation at low temperatures. Therefore Equation 52 was used to model the mechanical response of the polymer. Similar observations to the PPS samples can be made (Figure 29):

-the magnitude of the glass-transition stiffness drop increases with decreasing crystallinity,

-the transition temperatures increase with increasing crystallinity,

-the beta transition temperature varies between –60°C for the amorphous material to –30°C for a crystallized material, values that correspond to those given in the literature[7],

-the glass transition is between 144°C and 157°C, values that corresponds to literature data[65],

-a modulus increase can be observed for the amorphous sample at the crystallization temperature.

The different parameters are summarized in Table 7.

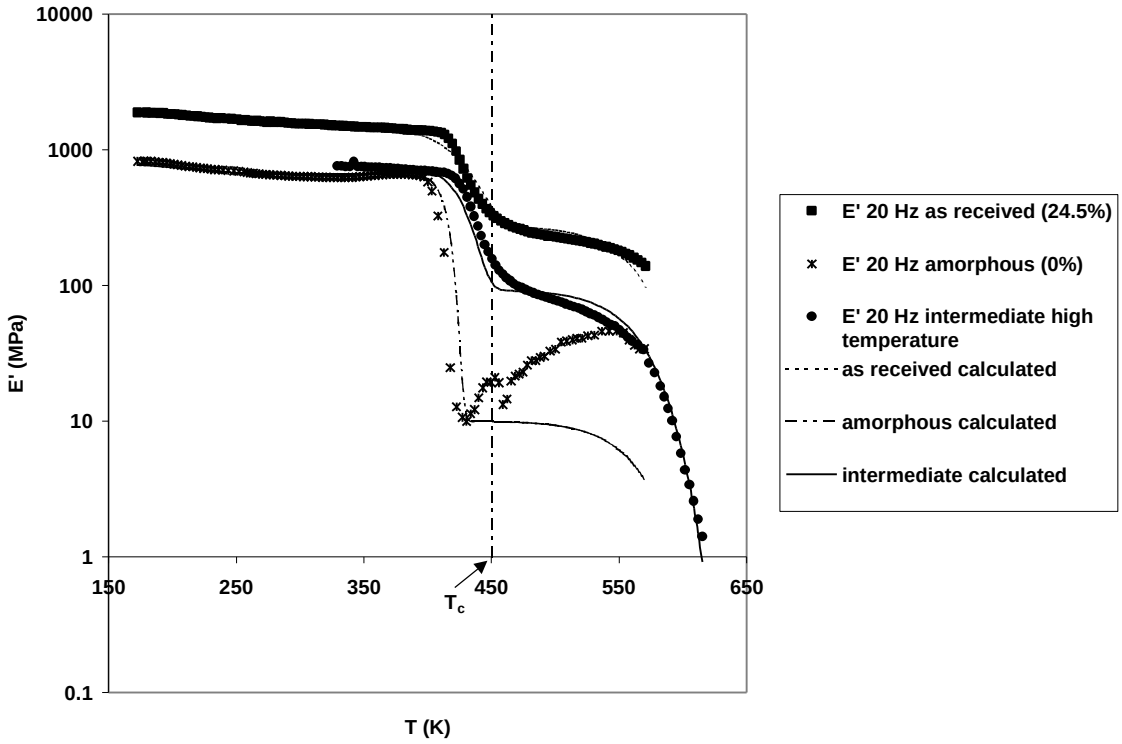


**Figure 29. Experimental and theoretical results for various crystallinities of PEEK 150**

**Table 7. Parameters for PEEK 150**

| Material | $T_1$ (K) | $T_2$ (K) | $T_3$ (K) | $E_1$ (MPa) | $E_2$ (MPa) | $E_3$ (MPa) | $m_1$ | $m_2$ | $m_3$ |
|---|---|---|---|---|---|---|---|---|---|
| PEEK 150 amorphous | 213 | 417 | 570 | 824 | 661 | 10 | 5 | 60 | 20 |
| PEEK 150 intermediate | 230 | 430 | 570 | 900 | 780 | 93 | 5 | 30 | 20 |
| PEEK 150 as received | 254 | 431 | 570 | 1875 | 1470 | 275 | 5 | 20 | 20 |

2.5.1.2.2 PEEK 450

The results for PEEK 450 are shown in Figure 30 and Table 8.

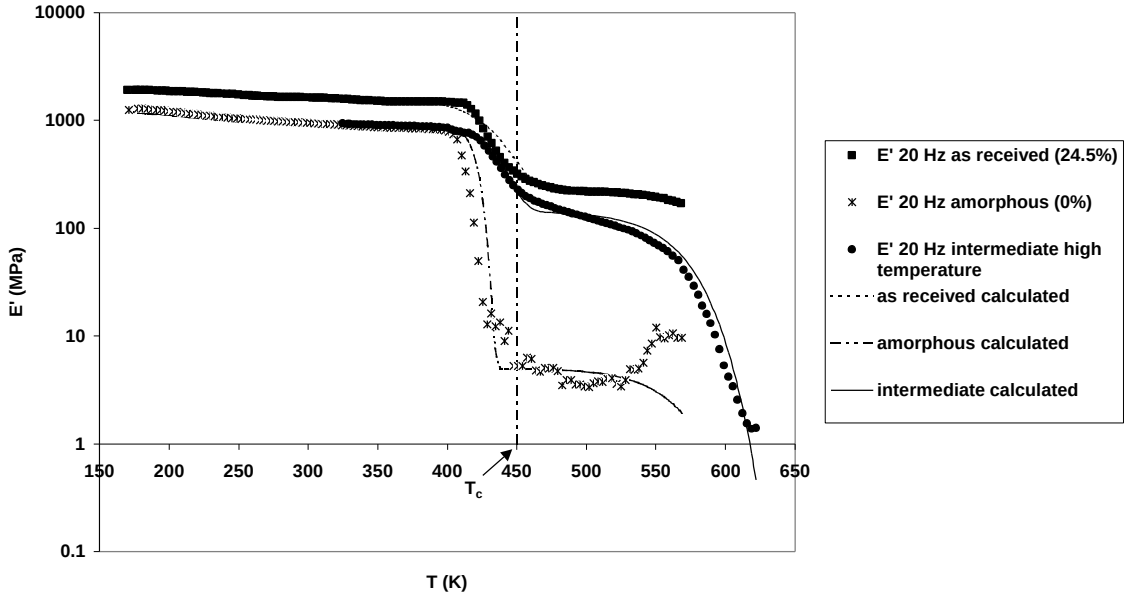


**Figure 30. Experimental and theoretical results for various crystallinities of PEEK 450**

**Table 8. Parameters for PEEK 450**

| Material | $T_1$ (K) | $T_2$ (K) | $T_3$ (K) | $E_1$ (MPa) | $E_2$ (MPa) | $E_3$ (MPa) | $m_1$ | $m_2$ | $m_3$ |
|---|---|---|---|---|---|---|---|---|---|
| PEEK 450 amorphous | 221 | 422 | 570 | 1279 | 920 | 5 | 5 | 60 | 20 |
| PEEK 450 intermediate | 221 | 435 | 570 | 1300 | 950 | 143 | 5 | 30 | 20 |
| PEEK 450 as received | 254 | 435 | 600 | 1920 | 1600 | 220 | 5 | 20 | 20 |

2.5.1.2.3 Composite

The DMA was also preformed on the composite as received (nearly amorphous) and crystallized. As the DMA was performed in bending, we can observe a large temperature effect. For the crystallized sample, the glass transition disappears. This

behavior was observed in other studies for highly crystalline materials[78]. In this case, we only need a "one transition" model (Equation 50).

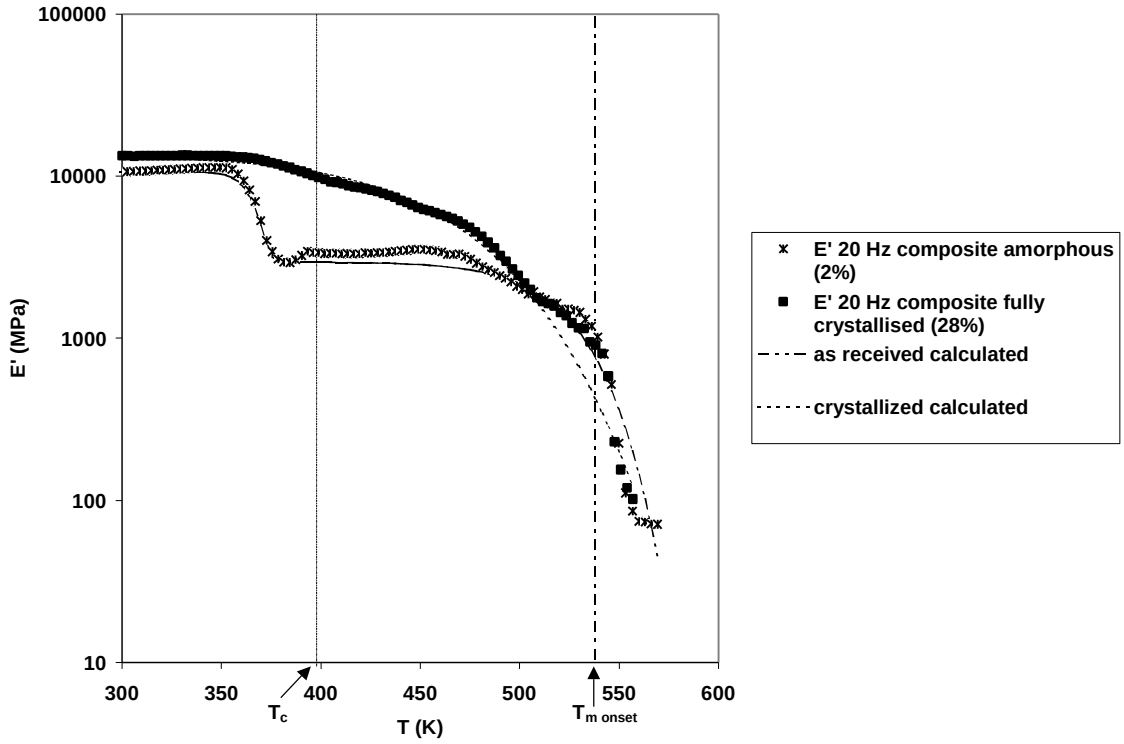


**Figure 31. Experimental and theoretical results for various crystallinities of AS4/PPS composite**

**Table 9. Parameters for AS4/PPS composite**

| Material | $T_2$ (K) | $T_3$ (K) | $E_2$ (MPa) | $E_3$ (MPa) | $m_2$ | $m_3$ |
|---|---|---|---|---|---|---|
| PPS/AS4 composite as received | 368 | 530 | 10690 | 2957 | 60 | 20 |
| PPS/AS4 composite crystallized | | 469 | | 11335 | | 9 |

### *2.5.2 Varying the molecular weights*

We also investigated the effect of molecular weight on the different parameters by testing different grades of a same polymer.

*2.5.2.1 PMMA*

To investigate the effect of molecular weight on our model, a completely amorphous material was chosen. The two molecular weight samples of PMMA were tested and experimental results are reported in Figure 32. The different parameters are summarized in Table 10. As expected the high molecular weight material was slightly stiffer than the low molecular weight sample. The different transitions also occurred for higher temperatures for the high molecular weight specimen.

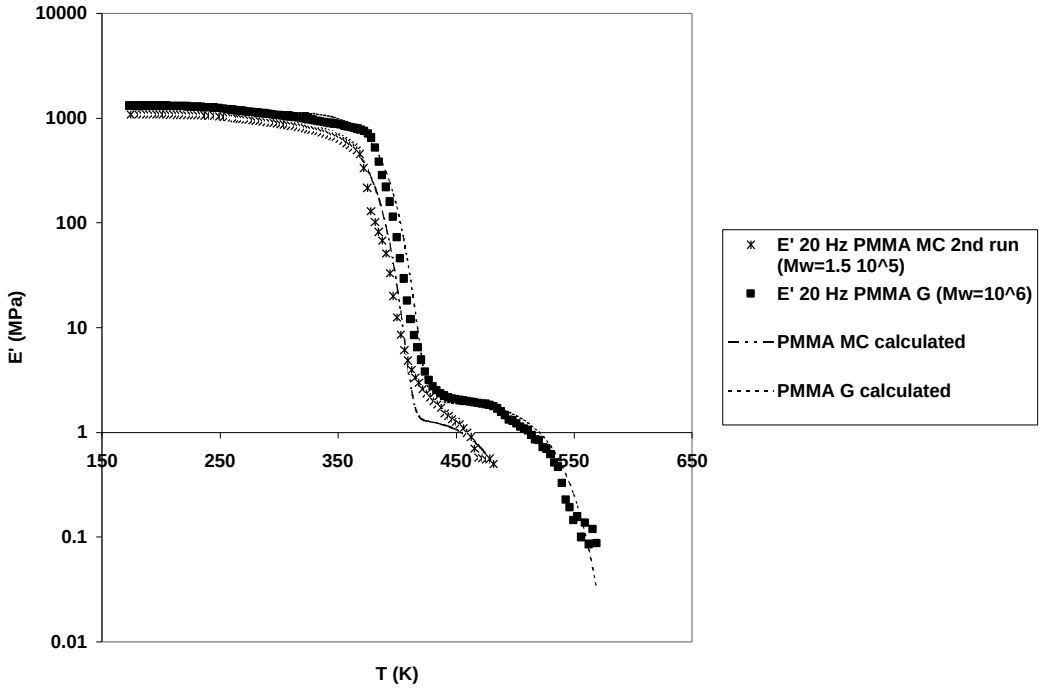


**Figure 32. Experimental and theoretical results for PMMA**

**Table 10. Parameters for PMMA**

| Material | $T_1$ (K) | $T_2$ (K) | $T_3$ (K) | $E_1$ (MPa) | $E_2$ (MPa) | $E_3$ (MPa) | $m_1$ | $m_2$ | $m_3$ |
|---|---|---|---|---|---|---|---|---|---|
| PMMA MC ($10^5$ g/mol) | 273 | 375 | 480 | 1080 | 867 | 1.4 | 5 | 20 | 20 |
| PMMA G ($10^6$ g/mol) | 273 | 385 | 530 | 1347 | 1150 | 2 | 5 | 20 | 20 |

*2.5.2.2 PPS*

For comparison purposes, the DMA of the PPS samples with different molecular weights were plotted on a same graph (Figure 33). The samples "as received" are being compared. One should note that the crystallinities are slightly different from one grade to the other. The higher molecular weight material is a little bit stiffer and flows for slightly higher temperatures. The PR10 grade crosses the other molecular weight curve. This phenomenon has been observed in other studies[79] but is not yet well understood.

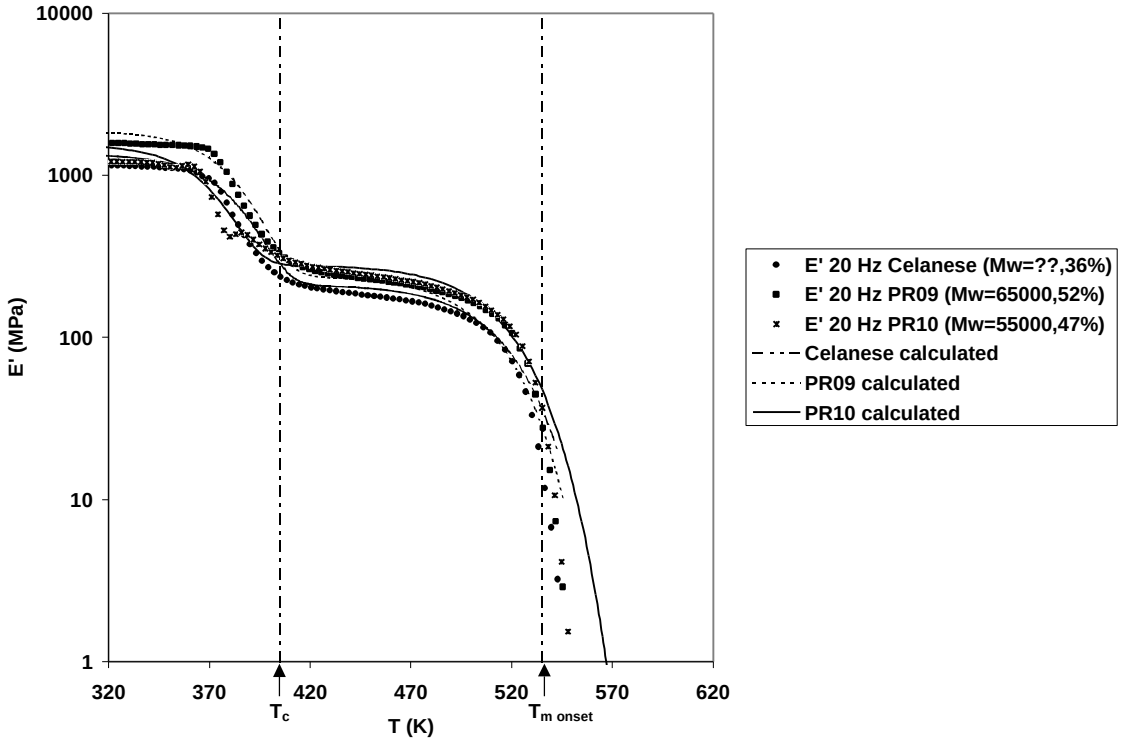


**Figure 33. Experimental and theoretical results for various molecular weights of PPS**

*2.5.2.3 PEEK*

The two grades of PEEK were plotted on a same graph (Figure 34). The as received samples had similar crystallinities. As can be observed, the higher molecular weight polymer is slightly stiffer and flows at temperatures slightly higher than the lower molecular weight. However, the difference between these two curves is not clearly significant.

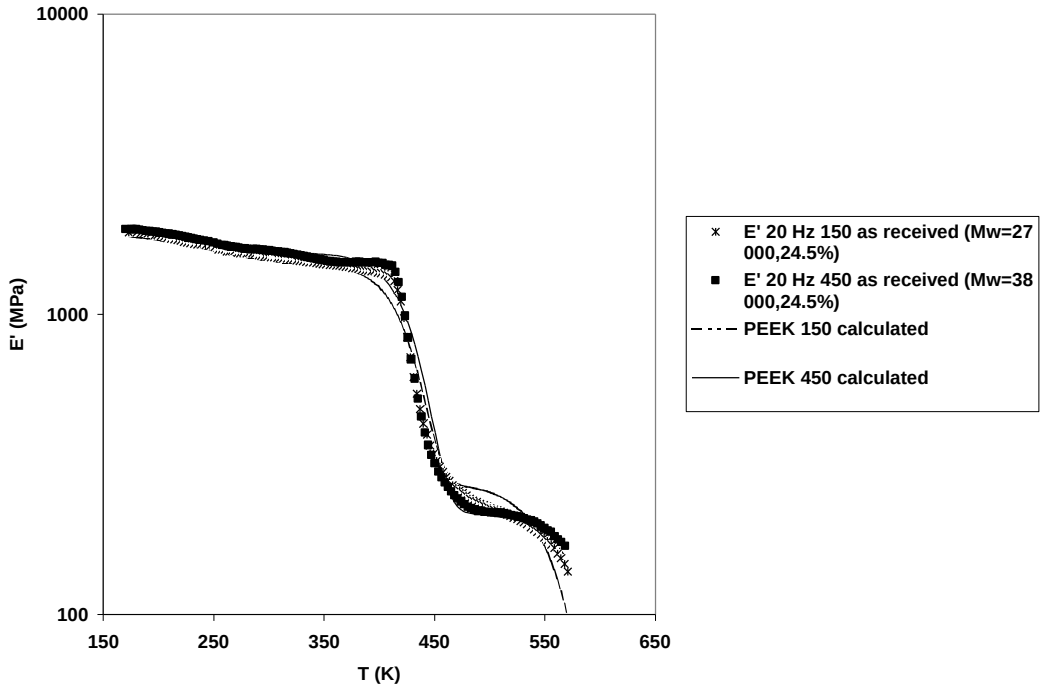


**Figure 34. Experimental and theoretical results for various molecular weights of PEEK**

*2.5.2.4 Polybutadiene*

The results of the DMA on the two grades of polybutadiene that were stiff enough to be tested are shown in Figure 35. The height of the glassy plateaus are similar for the two molecular weights but the higher molecular weight material becomes stiffer than the lower molecular weight elastomer above Tg. No significant flow could be observed for the high molecular weight material while the 100,000 g/mole polybutadiene sample started to flow below room temperature. The glass transition temperature was found to be -83°C, a value that compares well with the temperature indicated in the literature[78]. The other parameters used for the theoretical model are shown in Table 11.

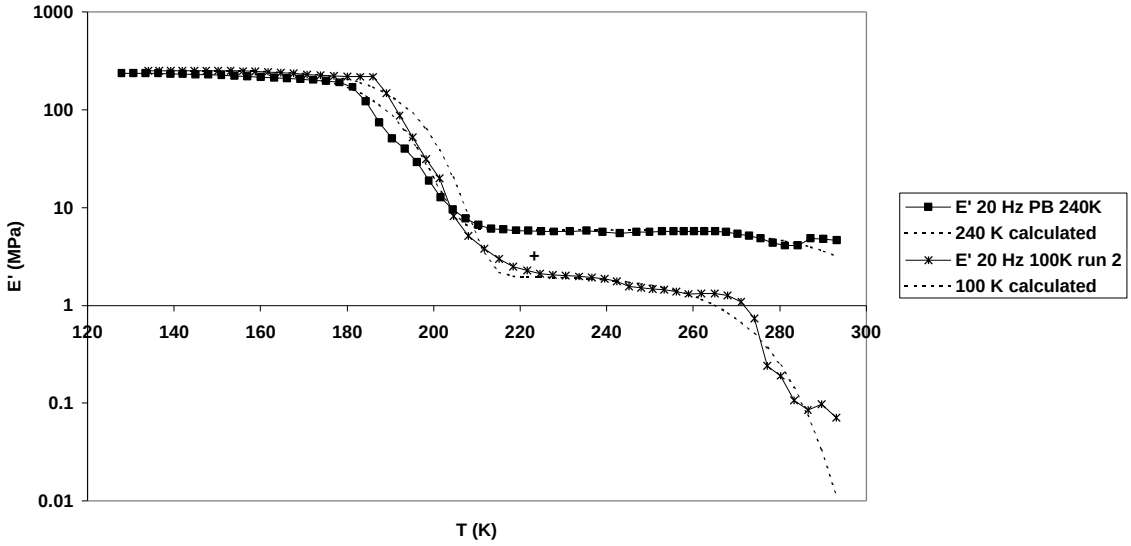


**Figure 35. Experimental and theoretical results for various molecular weights of unfilled polybutadiene**

**Table 11. Parameters for unfilled polybutadiene**

| Material | $T_2$ (K) | $T_3$ (K) | $E_2$ (MPa) | $E_3$ (MPa) | $m_2$ | $m_3$ |
|---|---|---|---|---|---|---|
| Rubber ($10^5$ g/mol) | 190 | 270 | 251 | 2 | 20 | 20 |
| Rubber ($2.4.10^5$ g/mol) | 190 | 300 | 236 | 6 | 20 | 20 |

### *2.5.3 Varying the filler content*

Three samples of polybutadiene with similar molecular weights but various filler content levels were tested (Figure 36). The Tg, as well as the height of the rubbery plateau, was found to increase with increasing content of carbon black (Table 12). Surprisingly, the height of the glassy plateau is higher for the unfilled polymer. This observation might be explained by that fact that at low temperatures, fillers can impede the orientation of the molecules, leading to a more compliant polymer at low temperatures. The Weibull moduli vary significantly (Table 12) with the amount of filler. These results are discussed in the following section.

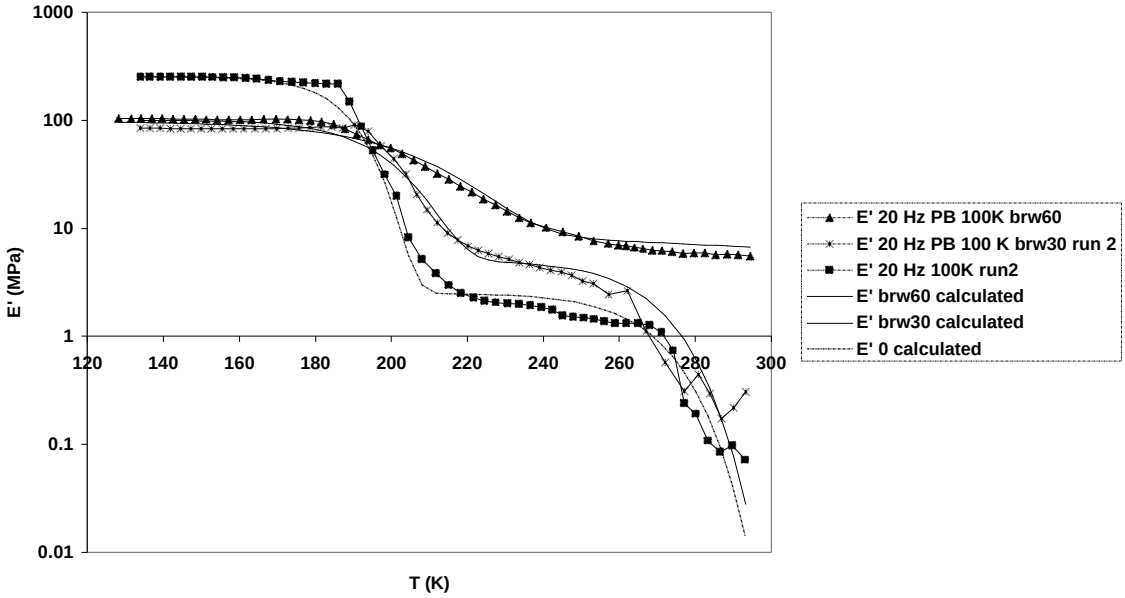


**Figure 36. Experimental and theoretical results for polybutadiene with different contents of carbon black**

**Table 12. Parameters for filled polybutadiene**

| Material | $T_2$ | $T_3$ | $E_2$ (MPa) | $E_3$ (MPa) | $m_2$ | $m_3$ |
|---|---|---|---|---|---|---|
| PB ($10^5$ g/mol) unfilled (0) | 190 | 270 | 251 | 2 | 20 | 20 |
| PB ($10^5$ g/mol) 23% CB (brw30) | 200 | 270 | 100 | 5 | 15 | 20 |
| PB ($10^5$ g/mol) 37.5% CB (brw60) | 210 | 270 | 104 | 20 | 10 | 1 |

## 2.6 Discussion

Using the model developed in section 2.2 lead to fairly successful representation of the various polymers having different chemical nature, molecular weights, crystallinity and filler contents. We could also successfully represent the behavior of the polymers in the different regions and transitions, from glassy state to melting and flow. However, the behavior of the amorphous polymers can only be analytically represented up to the crystallization temperature. After this temperature and at low heating rates, the material recrystallizes during the measurements leading to a rise in the modulus. At the present point, our model does not allow for bond re-formation.

The parameters needed to apply this equation are of two types: physical parameters and the statistical parameters. All of the physical parameters can be determined by independent experiments (e.g. transition temperatures, instantaneous moduli) and several models exist in the literature that relate these values to the microscopic details of the polymers (e.g. Tg-molecular weight relationship[1], magnitude of the glass transition drop-crystallinity relationship[80]). Therefore the main discussion will focus on the statistical parameters, the new feature of this study. The different parameters were obtained by fitting the model to the experimental data, in order to obtain the best fit for the shape of the curve (that does not necessarily correspond to the fit that minimizes the error). As discussed in section 2.2, we were expecting small values of the Weibull modulus to be associated with the beta transition (small number of molecular segments involved in the relaxation). We find $m_1$ constantly equal to 5. One needs to be careful about interpreting this result, however. This coefficient might slightly vary from one polymer to the other, but the magnitude of the relaxation was so small for our polymers that not much difference could be seen for a parameter varying between 2 and 40 (Figure 37). Higher values of the Weibull parameter lead to a slightly steeper transition while small values broaden the transition.

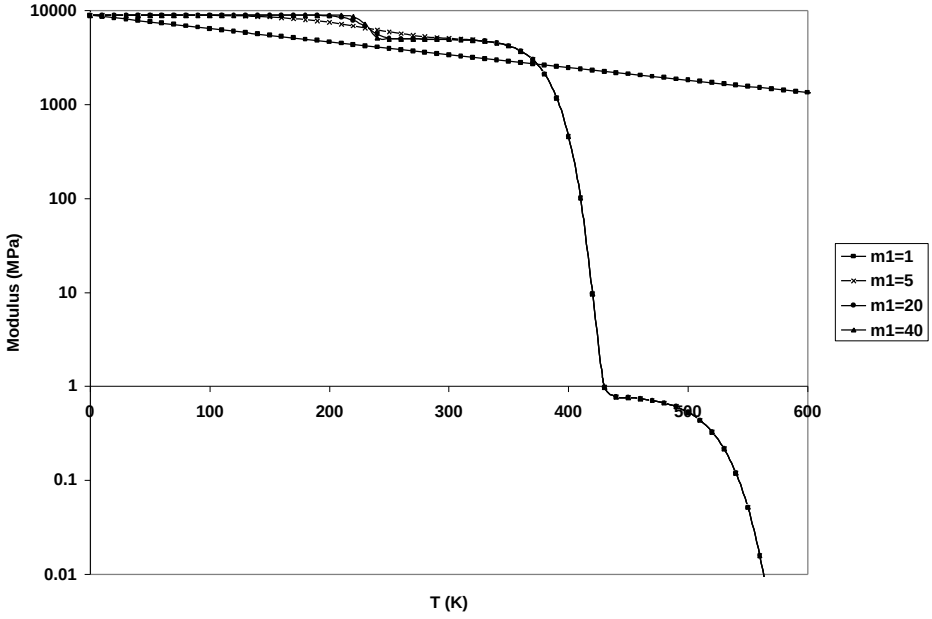


**Figure 37. Theoretical variations of the stiffness versus temperature curve. $m_2$=20, $m_3$=20, $m_1$=1, 5, 20, and 40**[55]

In the glass transition, we were expecting the Weibull coefficient $m_2$ to increase, as the number of molecular segments involved increases and the distribution of bond strength narrows. The sensitivity of the model to the variations of $m_2$ is illustrated by Figure 38. Large Weibull coefficients indicate a very simultaneous relaxation process and leads to a very abrupt glass transition. Lower values ($m_2$=5) broaden the transition. If flow occurs at relatively low temperatures, the glass transition might merge with the flow region and lead to a single transition.

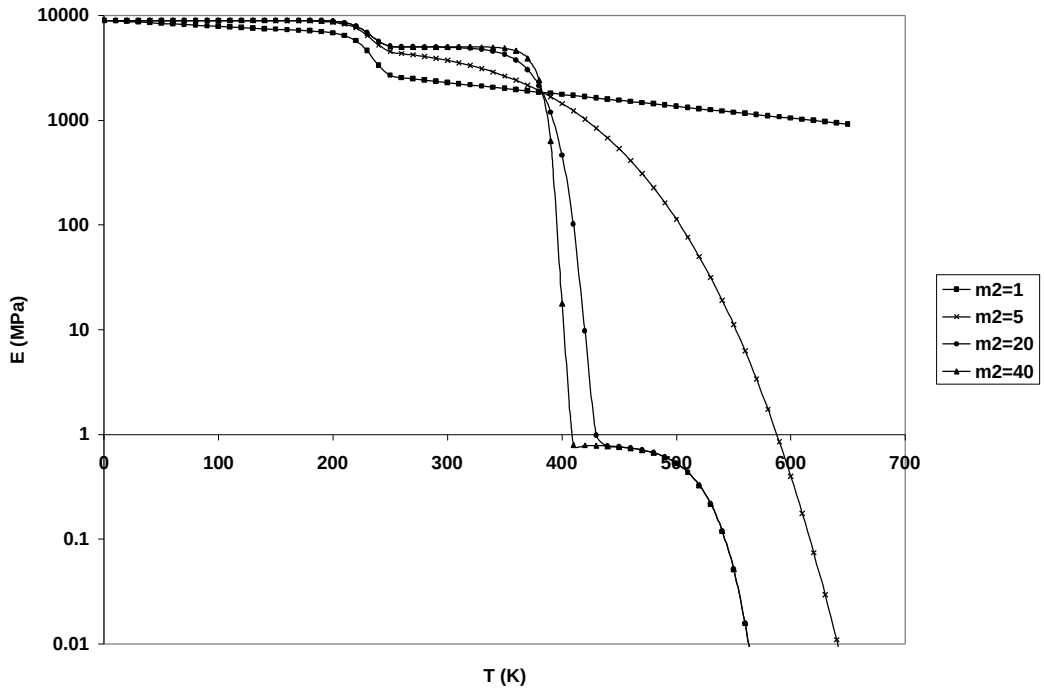


**Figure 38. Theoretical variations of the Stiffness versus Temperature curve. $m_1$=5, $m_3$=20, $m_2$=1, 5, 20, and 40**[55]

The Weibull coefficients were found equal to 20 for the unfilled elastomer, amorphous PMMA and thermoplastics as received. This coefficient does not seem to depend on molecular weight. Only the physical parameters ($T_i$, $E_i$) change according to already known rules[1]. However the Weibull coefficient ($m_2$) increases significantly with decreasing crystallinity: as the polymer becomes more homogenous, the distribution of

bond failure mechanisms narrows, leading to higher values of the Weibull modulus. The variations of $m_2$ with crystallinity content is illustrated by Figure 39. For the intermediate crystallinity PEEK samples, the content was assumed to be half of the maximum crystallinity. For a given material, the relationship between these two parameters appears to be linear. However, as already discussed, the crystallinity contents are only indicators for these materials and can not be taken as absolute value. A theoretical relationship between this coefficient and the percent of crystallinity still needs to be established, based on more extensive experiments, but is beyond the scope of the present dissertation.

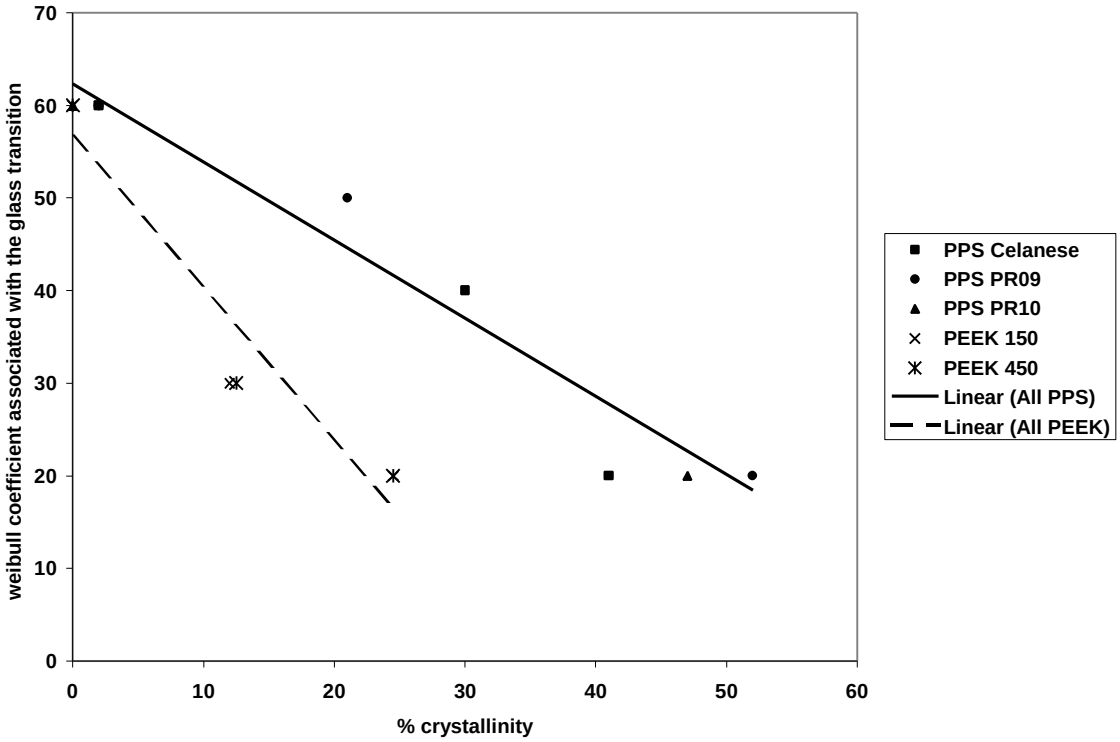


**Figure 39. $m_2$ versus crystallinity content**

According to section 2.5.3, $m_2$ also varies with the filler content. As the level of carbon black increases in polybutadiene, the Weibull coefficient associated with the glass transition ($m_2$) decreases. The filler has the same effect as crystallinity. Intuitively, the presence of impurities resemble the presence of crystallites: the distribution of secondary bond strength broadens with an increasing amount of fillers and the Weibull coefficient drops (consistent with crystallinity observations). Once again, the relationship between

$m_2$ and filler content seems to be linear (Figure 40). However, further experiments are required in order to establish a numerical relationship between these parameters.

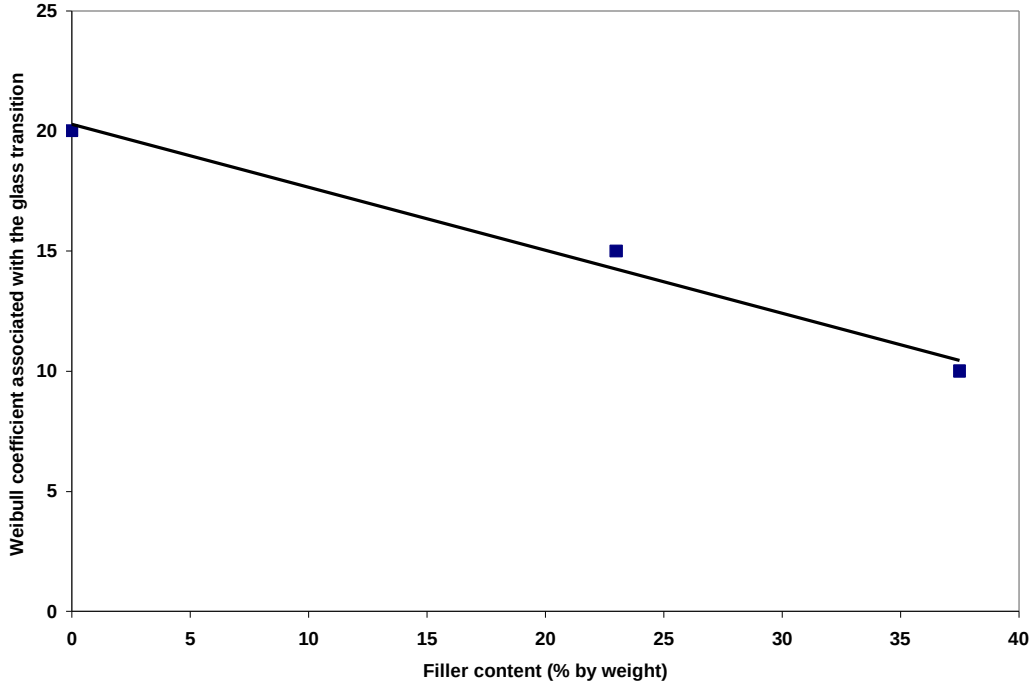


**Figure 40. $m_2$ versus carbon black content for polybutadiene**

The last coefficient related to melting and flow ($m_3$) was kept equal to 20. The flow region was not studied in detail in the present paper. However, the statistics of bond breakage seems to be applicable to this region of the material. It is remarkable that our model enables the curves associated with the different crystallinity degrees to meet after the melting temperature of the polymer. The effects of variations of this last coefficient are shown in Figure 41. The $m_3$ coefficient depends on the breadth of the melting transition (therefore on the polymer and the thermal history). We will only underline the fact that $m_3$=1 corresponds to a crosslinked polymer (infinite distribution of bond strength). Experiments on polymers with varying crosslinking content would enable the systematic study of this last parameter.

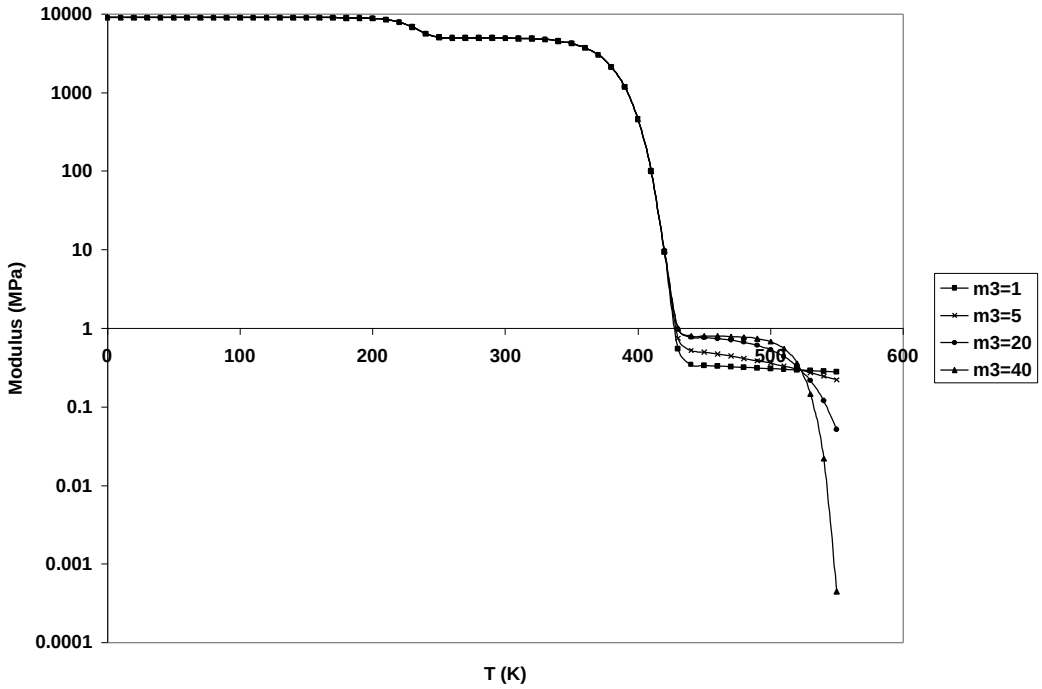


**Figure 41. Theoretical variations of the Stiffness versus Temperature curve. $m_1$=5, $m_2$=20, $m_3$=1, 5, 20, and 40**[55]

# Chapter 3 Effect of temperature on the mechanical behavior of polymer matrix composites

In Chapter 2, we established a model to calculate the modulus of a neat resin as an explicit function of temperature. In the present section, we will extend our study to the case of polymer matrix composites. First, we will use the stretched exponential in basic micromechanical models to try to reproduce experimental tensile data[45]. We will then turn to a more complex problem: the stress rupture of unidirectional composites in end-loaded bending at elevated temperatures. The life of unidirectional polymer matrix composites has been found to be very sensitive to temperature under an out-of-plane displacement[48,49,50,51]. We will seek to reproduce this sensitivity by making the modulus of the matrix a function of temperature in micromechanical models of compression strength. This study will also be extended to the life-prediction of polymer matrix composites under cyclic mechanical and thermal loads. Finally, the use of the model in classical macromechanical models will be illustrated by some examples of the integration of the stretched exponential into Classical Lamination theory[81].

## 3.1 Tensile experiments

The properties of unidirectional polymer matrix composites are in the fiber direction usually considered to be "fiber-controlled". According to this assumption, if the modulus of the fibers is almost independent of temperature (e.g. carbon fibers), the longitudinal modulus of the composite should also remain constant. Recent studies, however, have shown that the longitudinal modulus of unidirectional AS4/PPS and AS4/PEEK composites varies significantly with temperature[45].

The longitudinal modulus of a composite ($E_{11}$) can be approximated by a rule of mixtures:

**Equation 60**

$$E_{11} = E_f V_f + E_m V_m$$

where E refers to the modulus, V to the volume fraction, and the subscripts l to longitudinal, f to fiber and m to matrix. However a more refined model has been established by Subramanian et. al.[82] : an efficiency factor η is introduced and defined as the ratio between the longitudinal displacement $u_{f1}$ of the fiber and the displacement $u_{f2}$ of the matrix at the interface.

**Equation 61**

$$u_{m1} = h\, u_{f1}$$

This efficiency factor describes the ability of the matrix to transfer load to the fiber. This parameter varies between 0 (no transfer) to 1 (perfect bonding). From Subramanian[82] we know that the displacements follow Equation 62 and Equation 63.

**Equation 62**

$$u_z^f = h\, D z$$

**Equation 63**

$$u_z^m = D\, z$$

Where D is a constant and z is the fiber axial direction.

By definition, the strains (ε) are:

**Equation 64**

$$e_{zz}^f = \frac{d\, u_z^f}{d\, z}$$

**Equation 65**

$$e_{zz}^m = \frac{d\, u_z^m}{d\, z}$$

And following a rule of mixtures for the strain:

**Equation 66**

$$e_{zz}^{total} = V_f e_{zz}^f + V_m e_{zz}^m$$

Finally the longitudinal modulus is related to the strain and the applied stress ($\sigma_o$) by:

**Equation 67**

$$E_{11} = \frac{s_o}{e_{zz}^{total}}$$

From Equation 62, Equation 63, Equation 64, and Equation 65, we can easily relate the longitudinal modulus to the constituent properties:

**Equation 68**

$$e_{zz}^{f} = h\,D$$

**Equation 69**

$$e_{zz}^{m} = D$$

and

**Equation 70**

$$E_{11} = \frac{1}{V_f h + V_m} \times \frac{s_o}{D}$$

If there is no matrix-fiber load transfer then the modulus of the composite becomes the modulus of the matrix. This assumption can be discussed: a more realistic assumption would be that the modulus of the composite becomes equal to the modulus of the matrix multiplied by the volume fraction of matrix. However the establishment of the micromechanical model is not the purpose of the present paper and we will follow the assumption stated by Subramanian et. al.[82]. If there is perfect bonding then the rule of mixtures (Equation 60) should hold. These conditions can be expressed by the following set of equations:

**Equations 71**

$$\text{at } \eta=0 \quad E_{11} = E_m$$

$$\text{at } \eta=1 \quad E_{11} = E_f V_f + E_m V_m$$

Using these equations into Equation 70 we find that:

**Equation 72**

$$E_{11} = \frac{E_m V_m + h E_f V_f}{V_m + h V_f}$$

One can note that the composite modulus-efficiency factor relationship is non-linear. In the case of a unidirectional polymer matrix composite, the efficiency factor is going to vary as a function of temperature: at very low temperatures, the matrix-fiber bonding can be good and assumed to be almost “perfect”. At the other extremity of the temperature range, in the flow region, the matrix acts like a liquid and the load transfer ability is

significantly reduced. We can assume that the efficiency factor will be dependent on temperature in a manner similar to the modulus of the matrix. This assumption leads to the following system of equations (Equations 73):

**Equations 73**

$$h(T) = \sum_{i=1}^{N} l_i \exp\left(-\left(\frac{T}{T_i}\right)^{m_i}\right)$$

$$\sum_{i=1}^{N} l_i = 1$$

where $?_i$ is a constant for a given relaxation in a given material.

Finally, using Equations 73 in Equation 72, we obtain:

**Equation 74**

$$E_{11}(T) = \frac{E_m(T)\,V_m + \sum_{i=1}^{N} l_i \exp\left(-\left(\frac{T}{T_i}\right)^{m_i}\right) E_f V_f}{V_m + \sum_{i=1}^{N} l_i \exp\left(-\left(\frac{T}{T_i}\right)^{m_i}\right) V_f}$$

We can directly apply this last equation for unidirectional AS4/PEEK and AS4/PPS and compare the results to the experimental data of Walther[45]. For the AS4/PEEK composite, the volume fraction given by density measurements was 69%. The modulus of the fibers was assumed to be 2.26 MPa (values reported in the literature are a little bit higher[44], but this value remains realistic). $\lambda_1$ (Equations 73) was arbitrarily taken as 0.03, $\lambda_2$ as 0.05 and $\lambda_3$ as 0.92. The variation of the efficiency factor with temperature is shown in Figure 42.

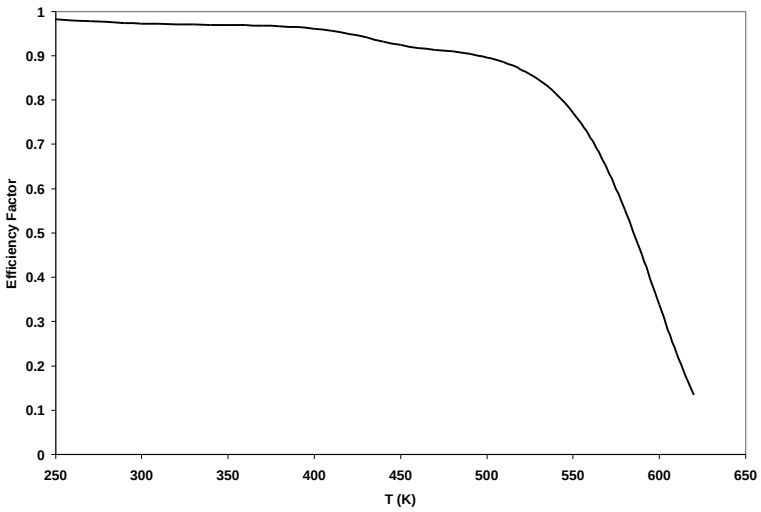


**Figure 42. Efficiency factor versus temperature for AS4/PEEK composite**

The prediction for the modulus variation with temperature of the matrix ($E_m(T)$) was calculated according to Equation 52. The statistical coefficients and transition temperatures were taken equal to those obtained for the crystalline PEEK 450 samples of chapter II (the AS4/PEEK composite of reference 45 exhibited the mechanical properties of a crystalline material). Theoretical results obtained through Equation 74 and Equation 52 are compared to experimental data in Figure 43.

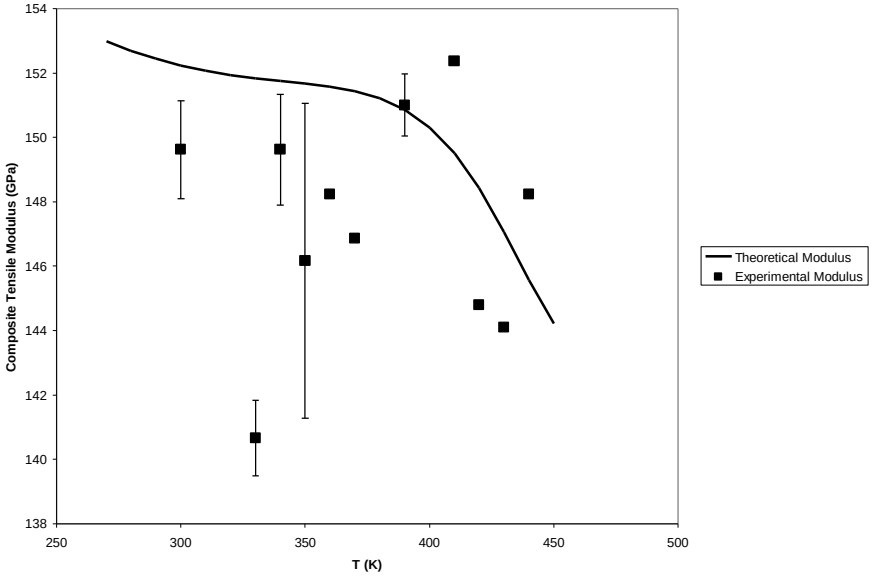


**Figure 43. Stiffness of unidirectional AS4/PEEK samples at various temperatures. Experimental data from Walther[45].**

A similar approach was used for unidirectional AS4/PPS with a volume fraction of 39% as computed by density measurements. In the following sections, we will differentiate the behavior of the crystalline and amorphous AS4/PPS composites. Therefore, two curves were generated:

- The "crystalline" curve was based on the statistical parameters used to relate the modulus of the highly crystalline neat PPS resin to temperature, and found in section 2.5.1.1.2. The efficiency factor ($\eta$) was taken constant and equal to 1 (if the material is very crystalline, the matrix is not going to flow as easily as in the amorphous case, giving a better load transfer capacity between the matrix and the fibers). The real value of the efficiency factor probably differs from 1, but we will consider this value as an upper bound for the following computations.
- The second curve ("amorphous" curve) was based on the statistical parameters of the fully amorphous PPS (see chapter 2). $\lambda_1$ (Equations 73) was arbitrarily taken as 0.03, $\lambda_2$ as 0.97.

The variations of the efficiency factors for the AS4/PPS composite with temperature are shown in Figure 44. The modulus versus temperature curves for the unidirectional composite in tension are compared to experimental data in Figure 45.

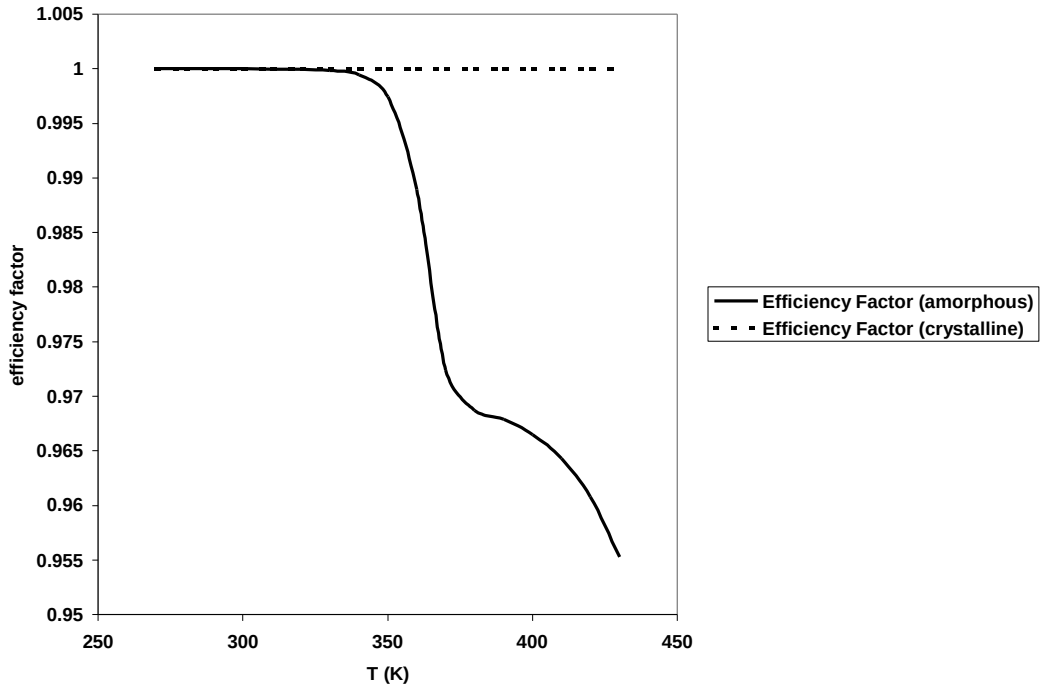


**Figure 44. Efficiency factors for the AS4/PPS composite.**

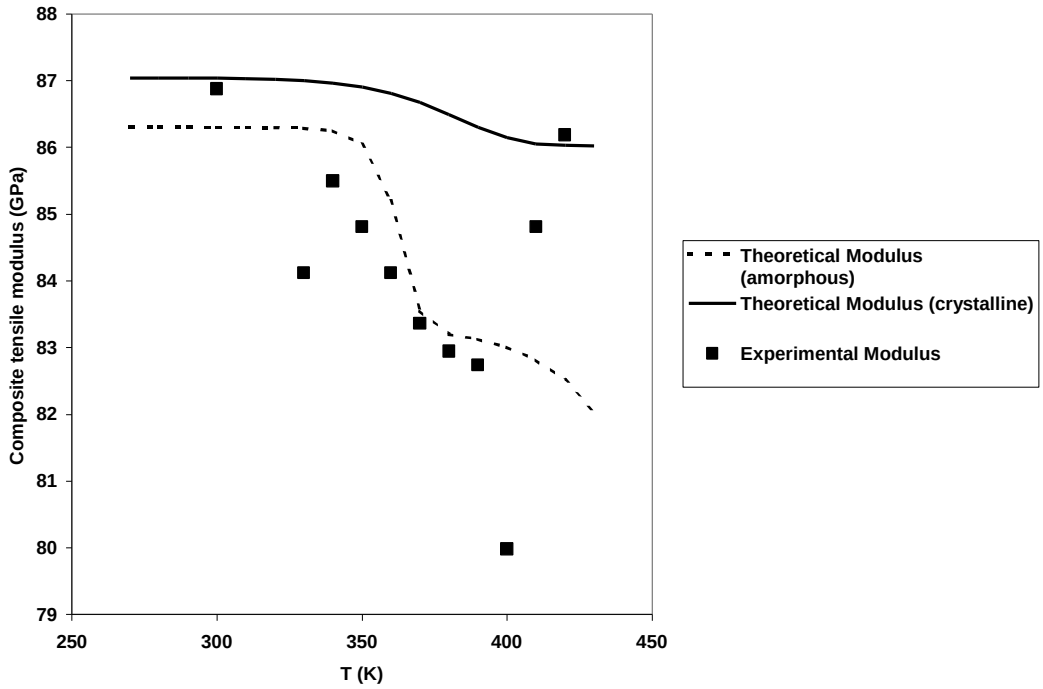


**Figure 45. Stiffness of unidirectional AS4/PPS samples at various temperatures. Experimental data from Walther[45]**

The experimental data for the AS4/PEEK material exhibit a lot of scatter. However, the calculations seem to follow the decreasing stiffness trend for increasing temperatures. The AS4/PPS data also show some scatter in the results. The decrease in the modulus of the overall composite seems to correspond to the shoulder of the calculated curve (around the glass transition temperature). The modulus starts increasing at 230°C, probably due to the crystallization of the matrix and reaches the curve for the composite calculated from the highly crystalline matrix with an efficiency factor of 1.

The $\lambda_i$ coefficients of Equations 73 can probably be measured directly by carefully studying the fiber/matrix interface. However, we will leave this topic as a recommendation for further study.

In the following sections, the $\lambda_i$ values chosen in order to calculate the efficiency factors seemed satisfactory and will be used (and never readjusted) in the other micromechanical and macromechanical models presented (section 3.2 and 3.3).

The calculations of section 3.4 will also require transverse properties. We can establish an equation similar to Equation 72 for the transverse modulus and shear modulus of the composite based on the following conditions:

**Equations 75**

At $\eta=0$ $E_{22}=E_m$

$$\text{At } \eta=1 \quad E_{22} = \frac{1}{\frac{V_f}{E_f} + \frac{V_m}{E_m}}$$

From these equations, we get Equation 76 for the composite transverse modulus:

**Equation 76**

$$E_{22}(T) = \frac{V_m + h(T)V_f}{\frac{h(T)V_f}{E_f} + \frac{V_m}{E_m(T)}}$$

We can extend this calculation to the shear modulus of the composite:

**Equation 77**

$$G_{12}(T) = \frac{V_m + h(T)V_f}{\frac{h(T)V_f}{G_f} + \frac{V_m}{G_m(T)}}$$

The variation of the transverse modulus with the efficiency factor is illustrated by Figure 46. The volume fraction of reinforcement was taken equal to be 50%, and the moduli were normalized by the value given by a rule of mixtures.

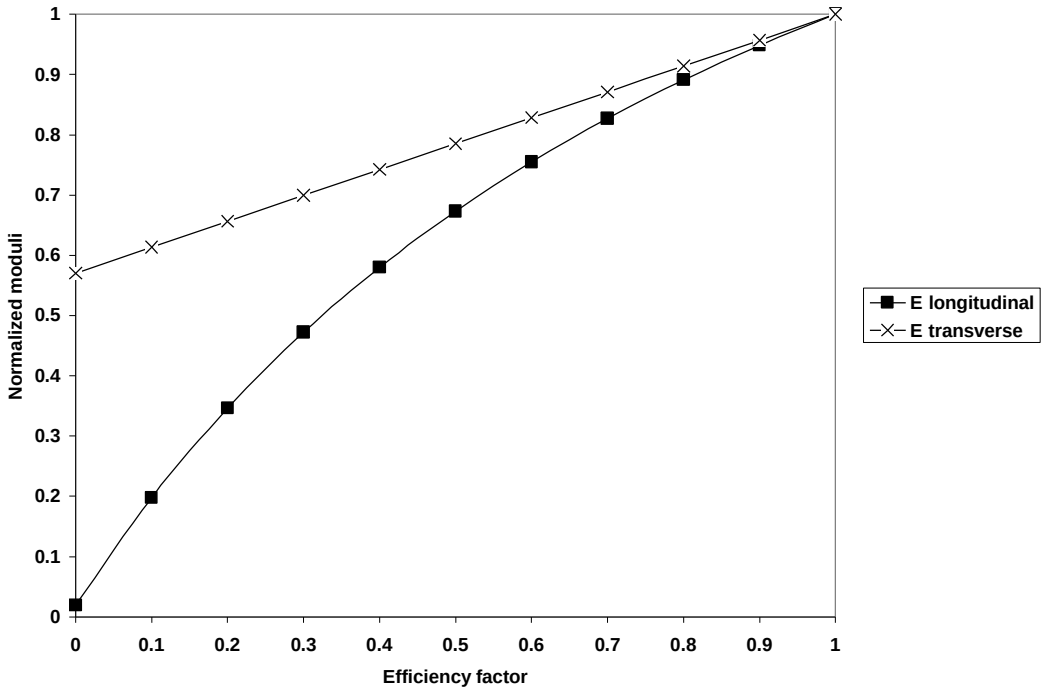


**Figure 46. Normalized longitudinal and transverse moduli versus efficiency factor for a 50% fiber volume fraction**

## 3.2 Stress rupture

### *3.2.1 Background*

Composites can encounter large out-of-plane displacements during storage or service. Temperature combined with bending can be very damaging for the material. Surprisingly, the literature concerning bending of polymer matrix composites is very

sparse, and generally focuses on three- of four-point bending. This type of experiment induces complex stresses at the loading points. End-loaded bending has been chosen over the conventional test methods in the present study to avoid any parasitic loading.

The design of a new end-loaded quasi-static bending fixture was reported in recent studies[50]. This fixture enabled stress rupture experiments: unidirectional carbon fiber polymer matrix composites were bent to fixed strain levels, held in position, and placed in an oven at two different temperatures. Rupture was observed and the time-to-failure was recorded[48,49,51]. Approaches to the non-linear geometry and material behavior were suggested. The major features of these previous studies can be summarized as follows:

- The experiments were run on unidirectional carbon fiber reinforced crystalline polymer matrix composite (AS4/PPS).
- The end-loaded fixture designed by Russell et. al.[50] and used for the quasi-static bending experiments is described in Figure 47. The specimens were placed flat on the fixture and bent by applying a compressive force on the fixture. The specimens were held in position by tightening the screws, and placed in an oven at different temperatures.

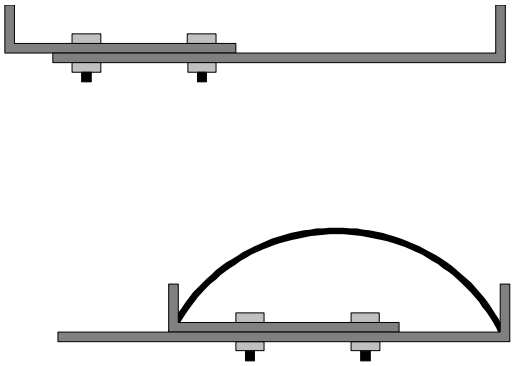

**Figure 47. End-loaded compression bending fixture. From Russell et. al.**[50]

- When bent, the specimen took the shape of a section of the elastica. The strain distribution along the length of the specimen can be calculated. The maximum strain occurred at the middle of the specimen and can be related to the end-to-end distance of the bent specimen[49].

- Microscopic observations revealed the presence of microbuckles on the compression side of the specimen (Figure 48). No significant damage could be observed on the tensile side (except at the failure location). It was concluded that stress rupture in end-loaded bending was compression driven for the material systems examined.

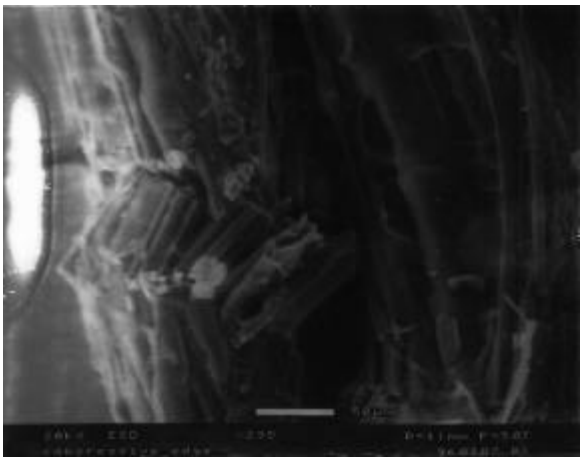

**Figure 48. Microbuckling in end-loaded experiments. From Mahieux et. al.**[48]

- Failure always resulted from the propagation of a fatal microbuckle located close to the middle of the specimen (location of highest strain level).
- Three ways of modeling the behavior of unidirectional carbon fiber polymer matrix composites in end-loaded bending at elevated temperatures were suggested[49]. The first model relied on the nucleation of the microbuckles. Budiansky's model for compression[83] was modified to suit the loading conditions. The local changes in modulus due to damage formation can be followed as a function of time at temperature. A second model was derived based on the propagation of a "fatal" microbuckle, assimilated to a thin crack. The third model was based on energy considerations, and related the time-to-failure to the local change of stiffness of the composite around the main microbuckle.

Although successful for one given temperature, these models did not explicitly relate the time-to-failure to temperature. The purpose of the present study was to predict

the behavior of the unidirectional composite at any strain level, for any temperature or range of temperatures.

### *3.2.2 Experimental work*

#### *3.2.2.1The material*

Stress rupture results have been reported earlier for crystalline PPS/AS4 with the following characteristics[48]: the material used for the experimental work was a polymer matrix/unidirectional continuous carbon fiber reinforced composite; polyphenylene sulfide (PPS) matrix/AS4 fibers. The matrix is a semi-crystalline thermoplastic and the fibers were oriented in the axial direction. This material was provided by Wellstream Inc (Panama city, FA). The percent of fiber by weight was 51.35%. The strain to failure was equal to 1.4% at room temperature and did not change at elevated temperatures. The average dimensions of the straight-sided coupon specimens were: length 15.2 cm, width 1.3 cm, and thickness 1mm.

A similar composite was also tested, but this time with an amorphous matrix. The composite with the crystalline material and the composite with the amorphous matrix were tested at 20°C/minute following the DSC procedure explained in chapter 2. Figure 49 compares the DSC graphs for these two materials.

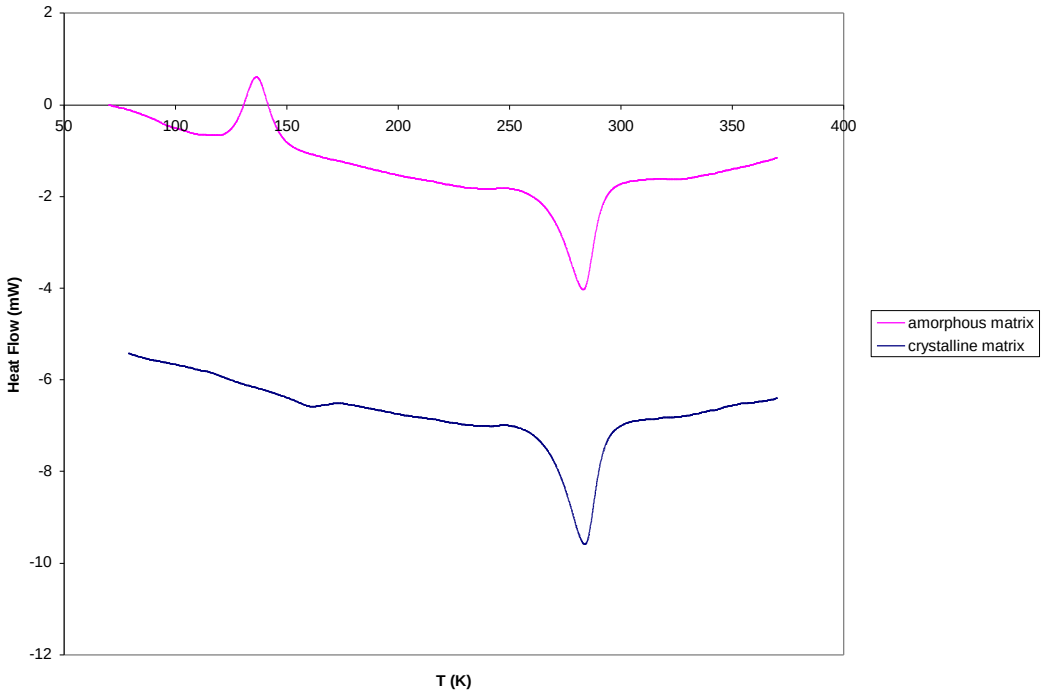


**Figure 49. DSC of the amorphous and crystalline AS4/PPS composite**

The composite with the amorphous matrix exhibits an endotherm and an exotherm peak indicating crystallization and melting phenomenon. The crystalline polymer only shows the presence of a melting peak. The measured enthalpies lead to a crystallinity of 30% (in volume) for the crystalline composite. The glass transition is different for the 2 materials. The amorphous material has a Tg (measured by DMA) around 90°C and the crystalline composite has a Tg around 120°C[84].

*3.2.2.2 Experimental apparatus and results*

Stress rupture experiments were performed in bending using the fixture shown in Figure 47, and following the procedure explained in section 3.2.1. The results of these tests for the crystalline material tested at 90°C and 120°C for various strain levels were reported in the literature[50] and are show in Figure 50 and Figure 51.

Note: The normalized maximum strain to failure corresponds to the maximum local strain of the bent specimen divided by the ultimate strain to failure in tension.

For the same crystalline material, isostrain data were also taken: the specimens were bent at 90% of their maximum strain to failure and the time-to-failures were recorded at different temperatures. The results are shown in Figure 52.

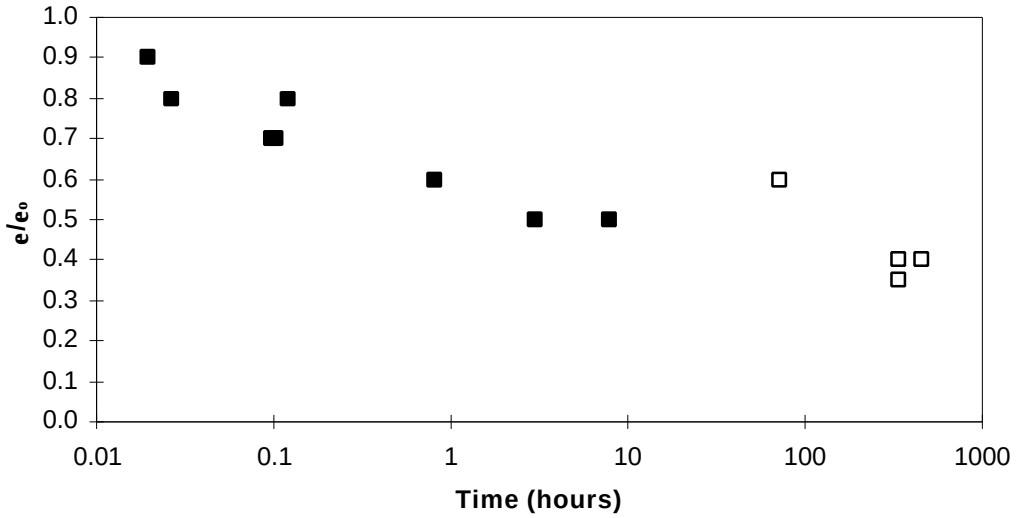


**Figure 50. Time-to-failure versus maximum applied strain at 90°C. (The empty squares indicate run-out experiments). From Russell et. al.**[50]

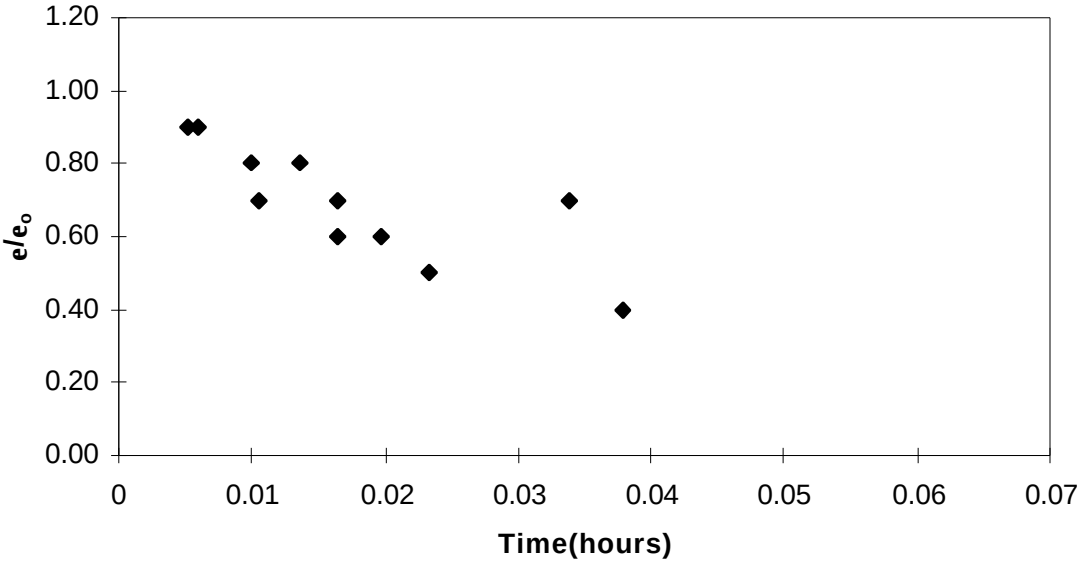


**Figure 51. Time-to-failure versus maximum applied strain at 120°C from Russell et. al.**[50]

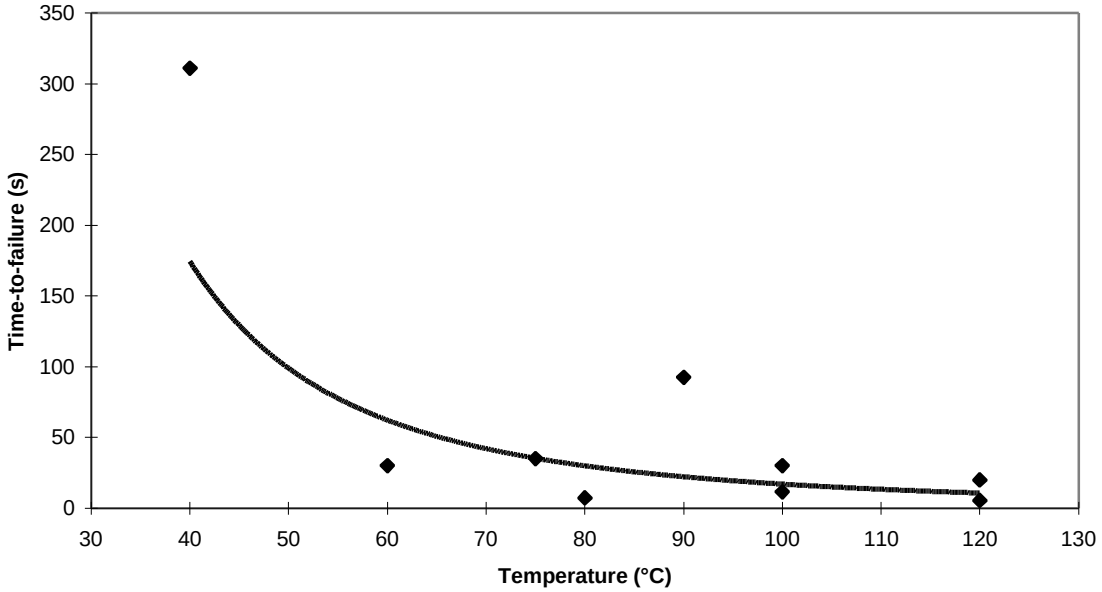


**Figure 52. Time-to-failure versus temperature for specimens bent at 90% of their strain-to-failure**[51]

The amorphous material was tested at two temperatures: 75°C and 90°C for various strains and at 75% and 90% for various temperatures. The results of these experiments are reported in Figure 53, Figure 54, Figure 55, and Figure 56.

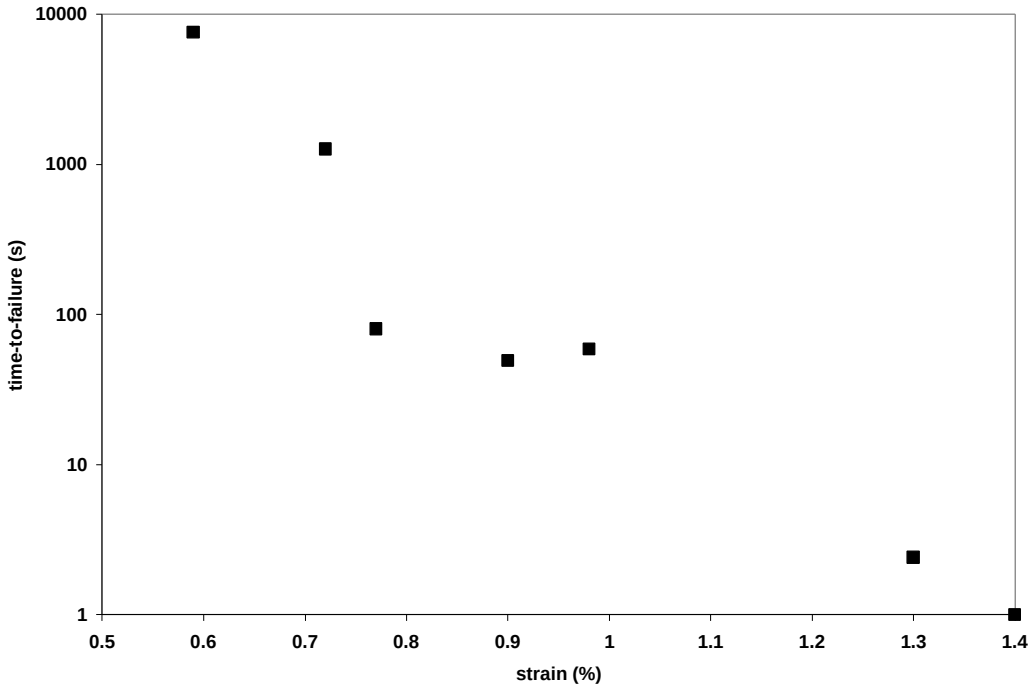


**Figure 53. Time-to-failure versus applied maximum strain at 75°C**

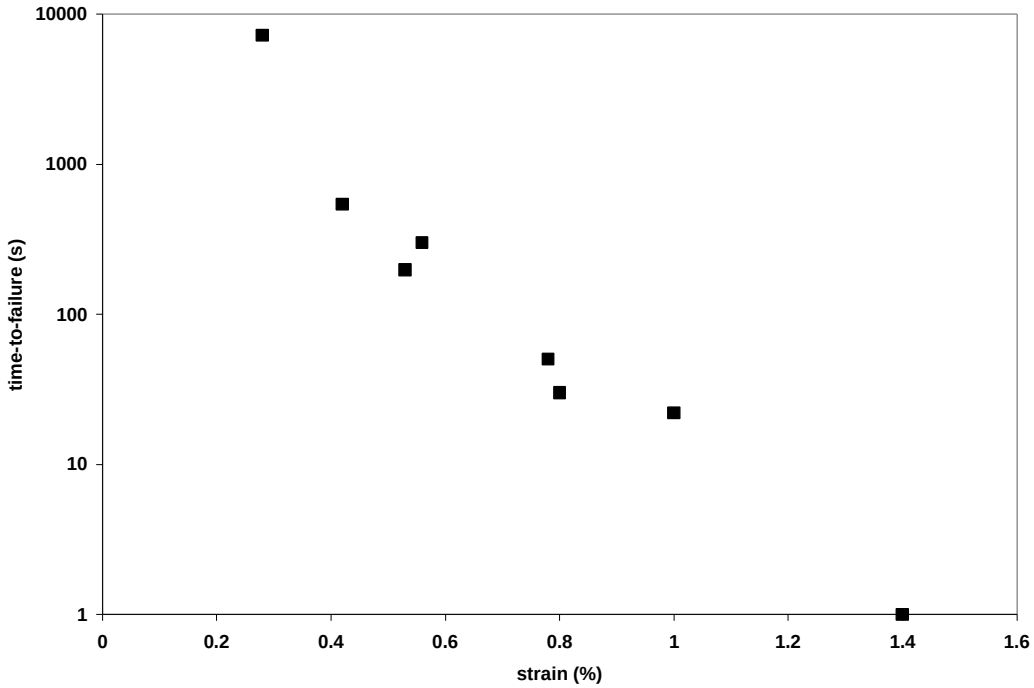


**Figure 54. Time-to-failure versus applied maximum strain at 90°C**

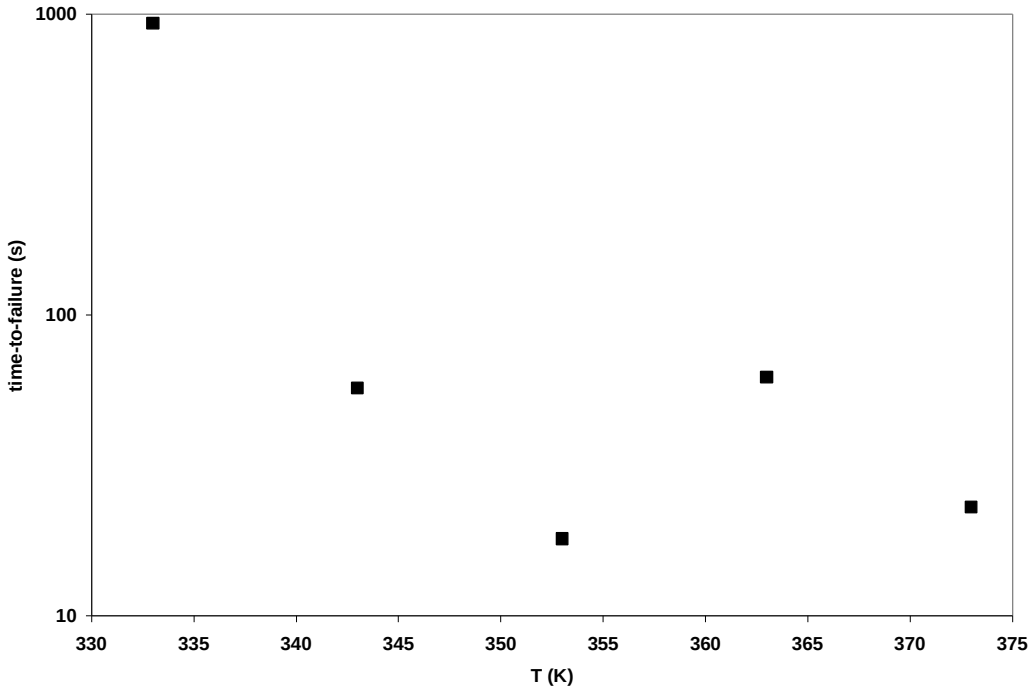


**Figure 55. Time-to-failure versus temperature at a maximum normalized strain of 75% (strain/ultimate strain-to-failure in tension)**

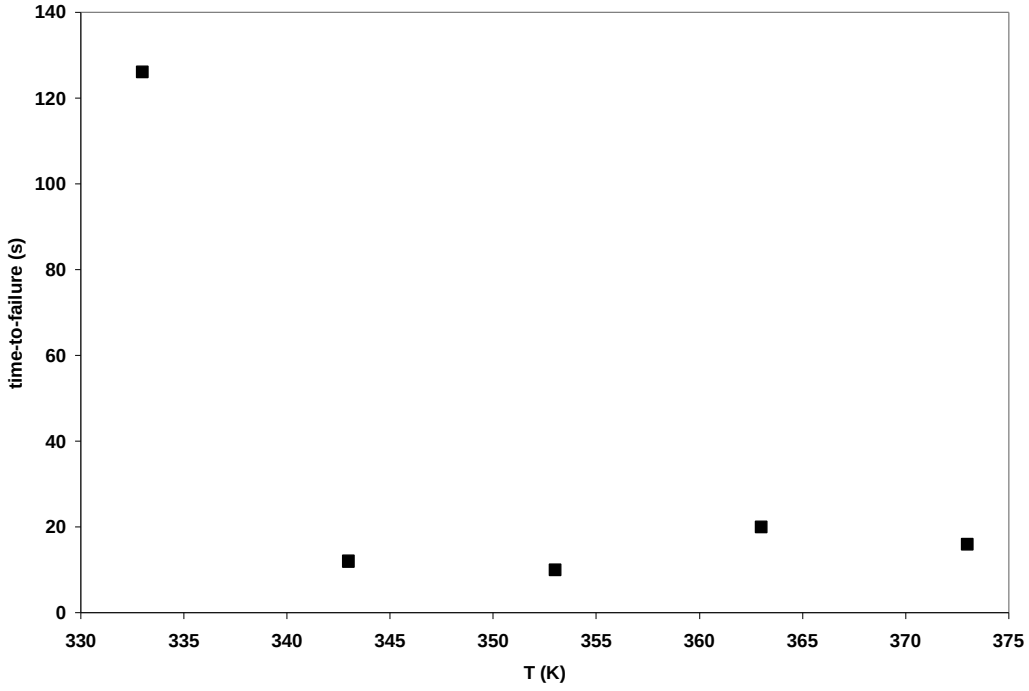


**Figure 56. Time-to-failure versus temperature at a maximum normalized strain of 90% (strain/ultimate strain-to-failure in tension)**

### *3.2.3Analysis*

We would like to reproduce the 7 previous curves (Figure 50, Figure 51, Figure 52, Figure 53, Figure 54, Figure 55, and Figure 56) using the explicit modulus-temperature relationship (Equation 52). For this purpose we will use Budiansky's model[83] derived for the propagation of a microbuckle under a compressive load with the modification suggested by Mahieux et. al.[49]. We will focus on the "fatal" microbuckle (microbuckle located at the center of the specimen, which propagation induces failure). A schematic of the microbuckle is given in Figure 57.

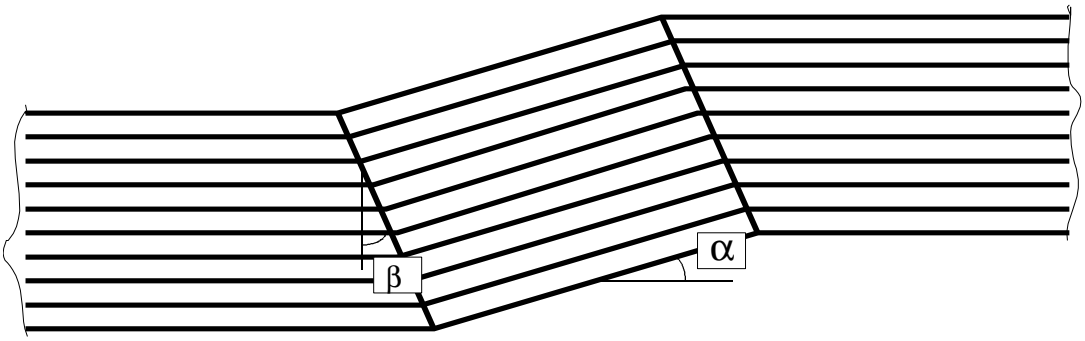


**Figure 57. Schematic of a microbuckle. a and b are the characteristic angles**[48]

Budiansky[83] assumes the following constitutive equation:

**Equation 78**

$$\frac{\dot{g}}{\dot{g}_{ref}} = \left( \frac{t}{t_{ref}} \right)^{M}$$

Where M is a material constant, $\dot{g}_{ref}$ is a reference value of the creep rate produced by the reference shear stress $t_{ref}$. The shear stress $\tau$ in the material depends on temperature. Therefore we can write:

**Equation 79**

$$\frac{\dot{g}}{\dot{g}_{ref}} = \left( \frac{t(T)}{t_{ref}(T)} \right)^{M}$$

We assume that the dependence of the reference shear stress follows the behavior of the modulus in temperature, i.e., can be described by Equation 80.

**Equation 80**

$$t_{ref}(T) = \sum_{i=1}^{N} m_i \exp\left(-\left(\frac{T}{T_i}\right)^{m_i}\right)$$

From Equation 79 we obtain

**Equation 81**

$$\frac{d\,g}{dt} = \dot{g}_{ref}\left(\frac{t(T)}{t_{ref}(T)}\right)^{M}$$

or

**Equation 82**

$$dt = \frac{1}{\dot{g}_{ref}}\left(\frac{t(T)}{t_{ref}(T)}\right)^{-M} d\,g$$

Knowing that for small ?

**Equation 83**

$$s = \frac{t}{g}$$

and integrating for a time varying between 0 and t and the microbuckle's angle varying from the initial misalignement of the fiber $\overline{f}$ to a greater angle $a = \overline{f} + f$, where $f$ is the additional angular displacement, we get:

**Equation 84**

$$\int_0^t dt = \frac{1}{\dot{g}_{ref}} \times \left(\frac{t_{ref}(T)}{s(T)}\right)^{M} \int_{\overline{f}}^{\overline{f}+f} g^{-M}\, d\,g$$

**Equation 85**

$$t = \frac{1}{M-1} \times \frac{1}{\dot{g}_{ref}} \times \left(\frac{t_{ref}(T)}{s(T)}\right)^{M} \times \left(\frac{1}{\overline{f}^{M-1}} - \frac{1}{\left(\overline{f}+f\right)^{M-1}}\right)$$

Assuming that failure occurs when the fibers reach 90° we can write the time to failure according to Equation 86.

**Equation 86**

$$t_f = \frac{1}{M-1} \times \frac{1}{\dot{g}_{ref}} \times \left( \frac{t_{ref}(T)}{s(T)} \right)^M \times \left( \frac{1}{\bar{f}^{M-1}} - \frac{1}{\left( \frac{p}{2} \right)^{M-1}} \right)$$

or

**Equation 87**

$$t_f = \frac{1}{M-1} \times \frac{1}{\dot{g}_{ref}} \times \left( \frac{\sum_{i=1}^{N} m_i \exp\left( -\left( \frac{T}{T_i} \right)^{m_i} \right)}{E_{11}(T) \times e_{\max}} \right)^M \times \left( \frac{1}{\bar{f}^{M-1}} - \frac{1}{\left( \frac{p}{2} \right)^{M-1}} \right)$$

The longitudinal modulus ($E_{11}(T)$) can be calculated according to Equation 74 and Equation 52 using the statistical values of the amorphous and crystalline neat PPS found in the previous part, results illustrated by the tensile results of section 3.1 (Figure 45). The only parameters that are not determined at this point are the $\mu_i$ parameters of the reference shear stress of Equation 80. These parameters were chosen to obtain a good fit for the first set of data (e.g. time-to-failure for crystallized specimens bent at 90°C for various strain level) but will never be readjusted to predict the 6 other sets of data. We used $\mu_1$ equals 60 and $\mu_2$ equals 40. These values can probably be experimentally measured. However this is being the scope of this work and will be suggested as further work.

The theoretical modulus-versus temperature curves for amorphous and crystalline neat PPS are shown in Figure 58.

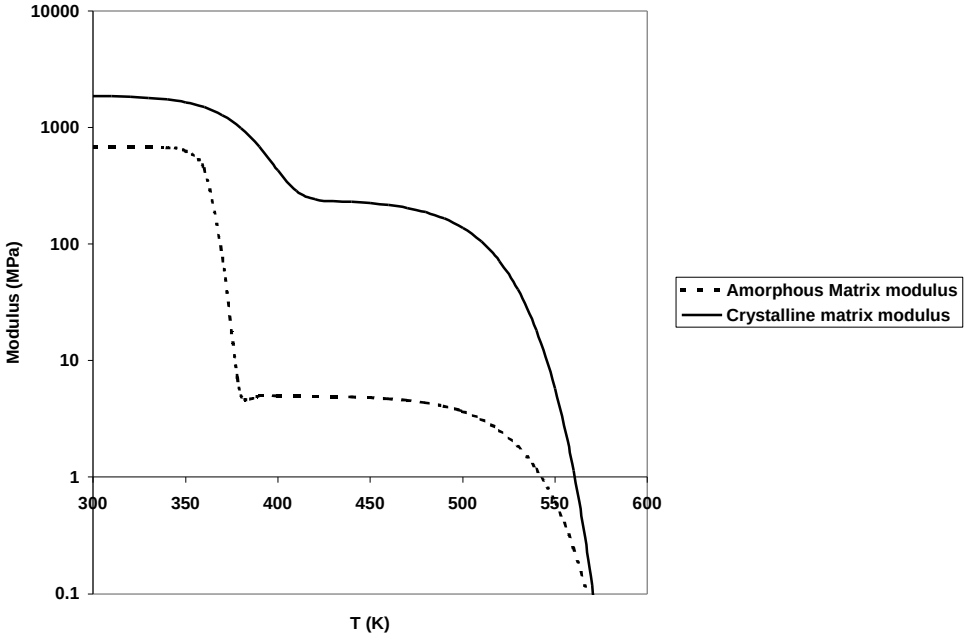


**Figure 58. Modulus versus temperature for PPS PR09 (low molecular weight)**

The variations of the efficiency factor and the reference stress are shown in Figure 59 and Figure 60 for the full range of temperatures.

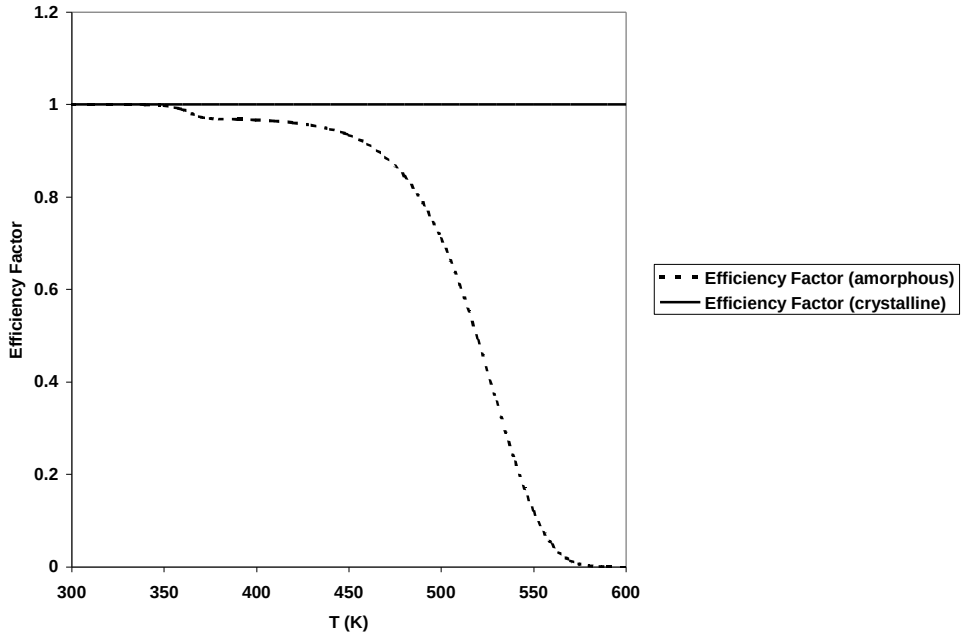


**Figure 59. Efficiency factor for AS4/PPS composite**

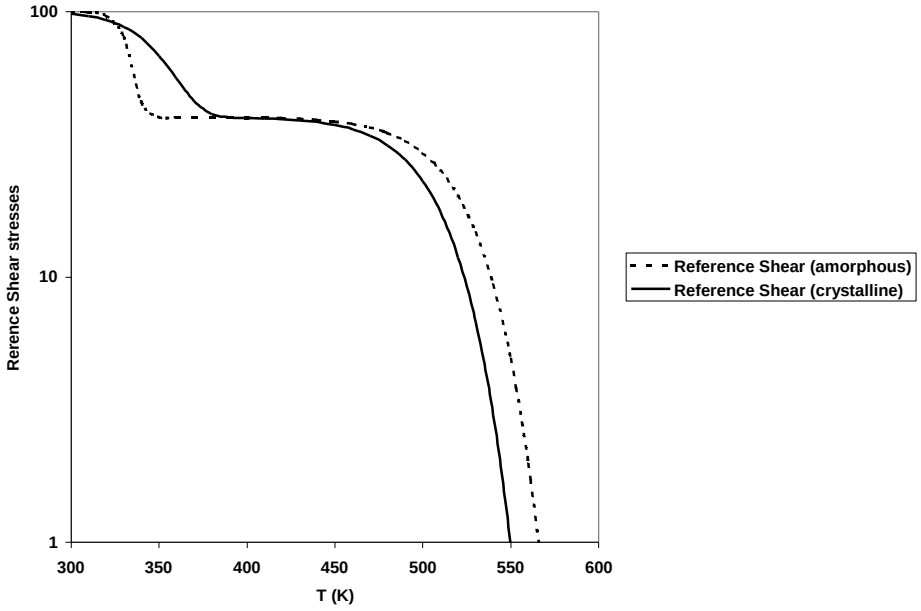


**Figure 60. Reference shear stress for AS4/PPS composite**

Using Equation 87 we can generate the stress rupture curves for the composite at various strain levels for a given temperature (isotemperature, Figure 61) and for various temperatures at a fixed strain level (isostrain, Figure 62).

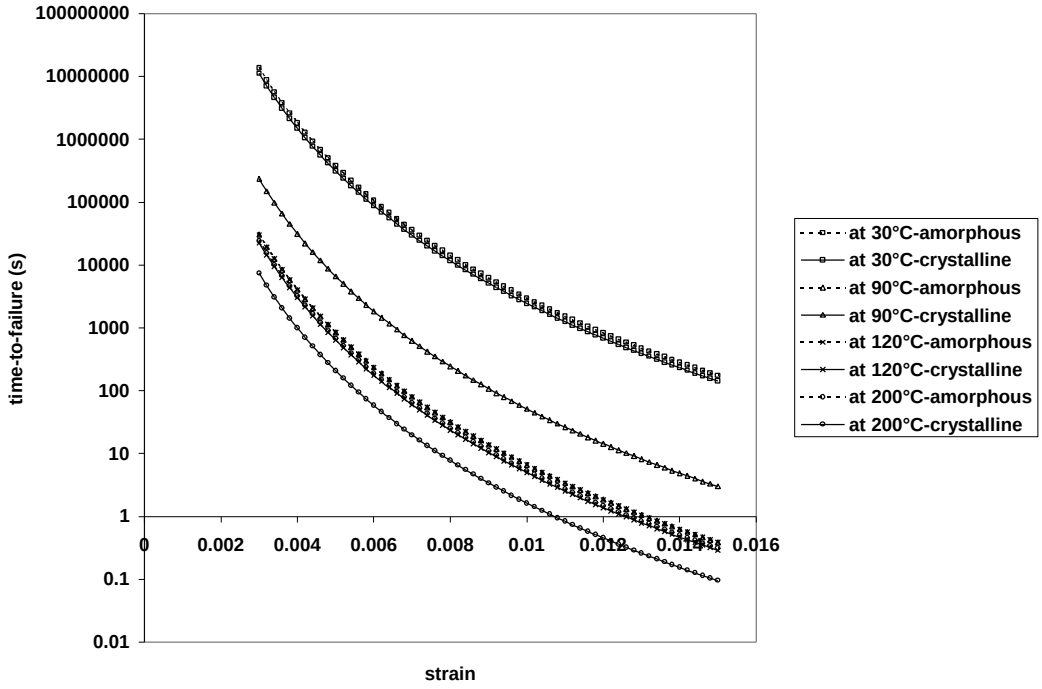


**Figure 61. Time-to-failure versus strain level prediction at 4 example temperatures (30°C, 90°C, 120°C, 200°C) for the crystalline and amorphous material**

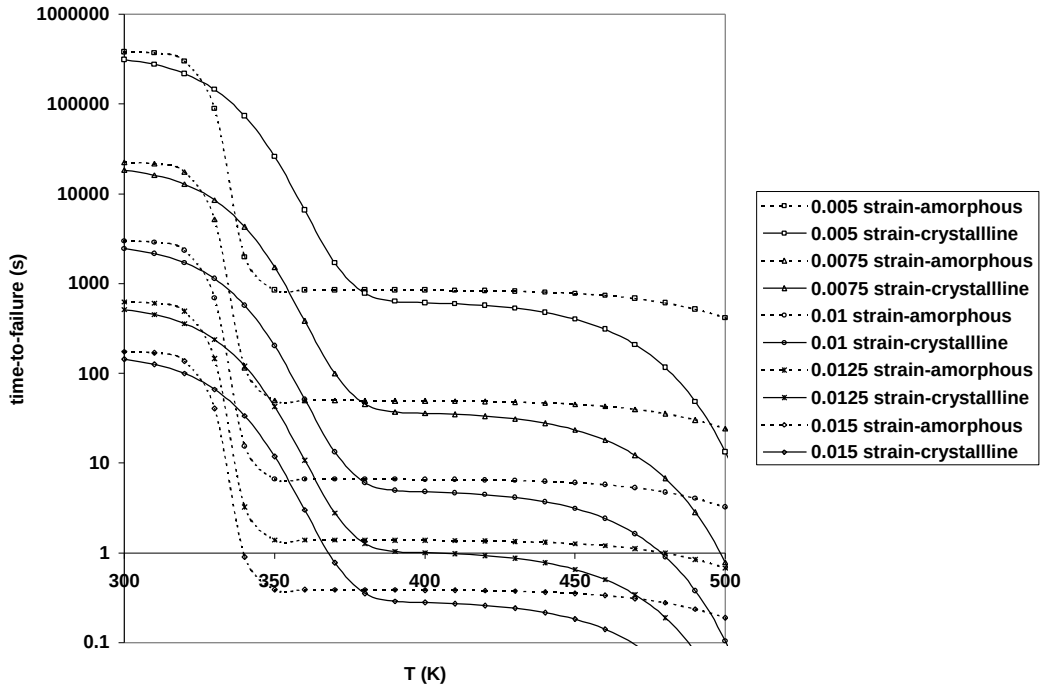


**Figure 62. Time-to-failure versus temperature prediction at 4 example strain levels (0.005, 0.0075, 0.01, 0.0125, 0.015) for the crystalline and amorphous material**

We can now compare these results to the experimental data. The experimental data and corresponding theoretical results are shown in Figure 63, Figure 64, Figure 65, Figure 66, Figure 67, Figure 68, and Figure 69.

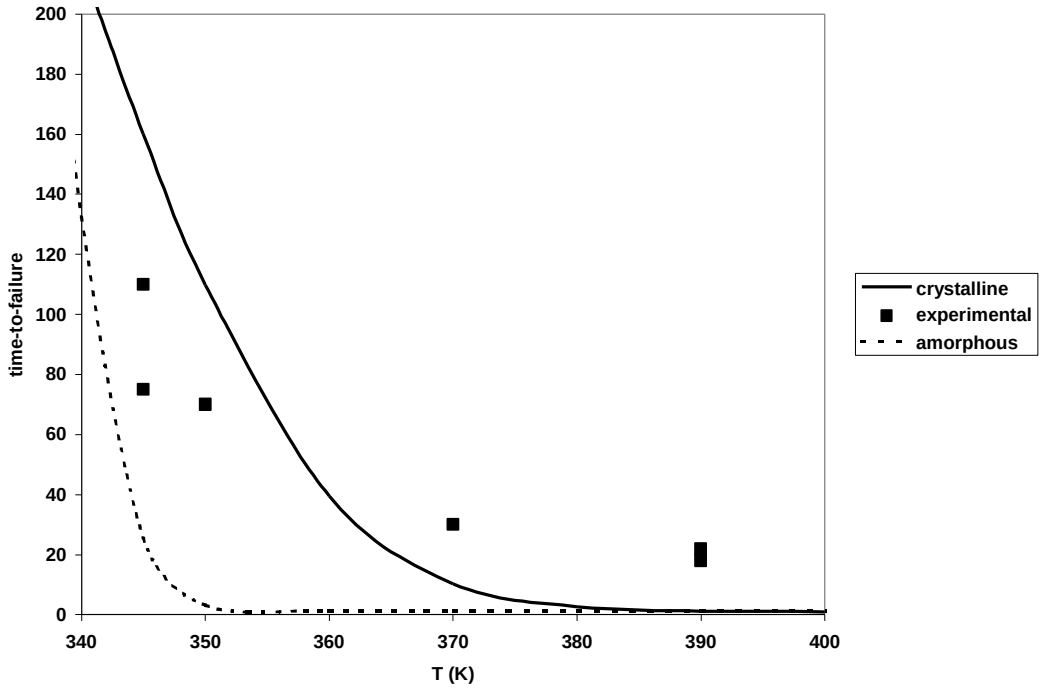


**Figure 63. Time-to-failure versus temperature for crystalline specimen bent at 90% of its maximum strain-to-failure**

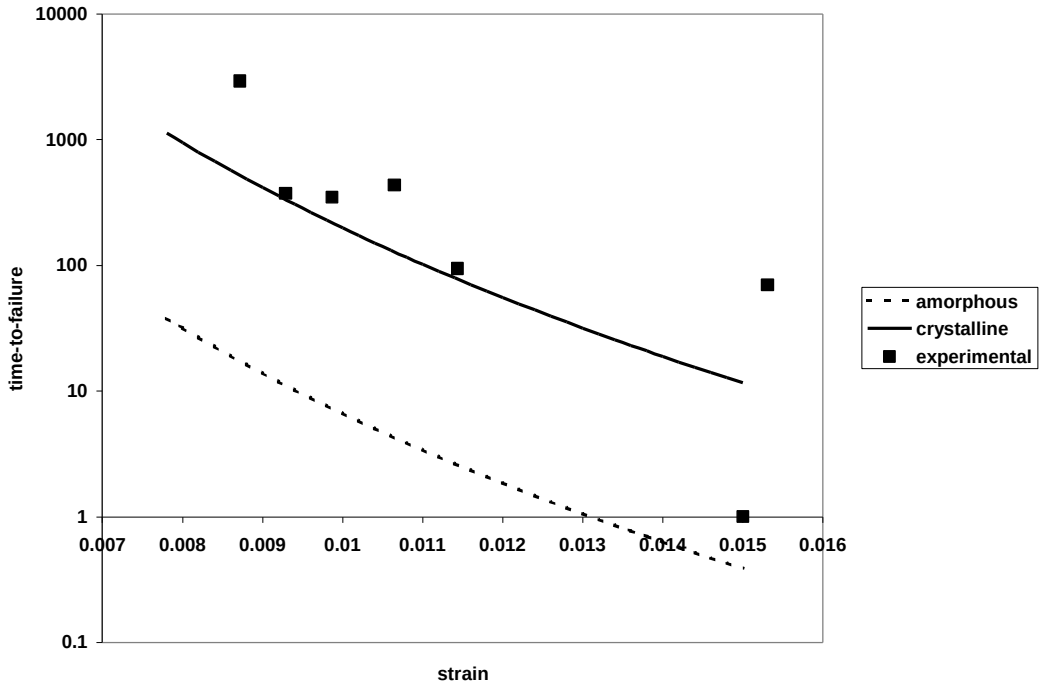


**Figure 64. Time-to-failure versus maximum strain-to-failure for crystalline specimen at 90°C**

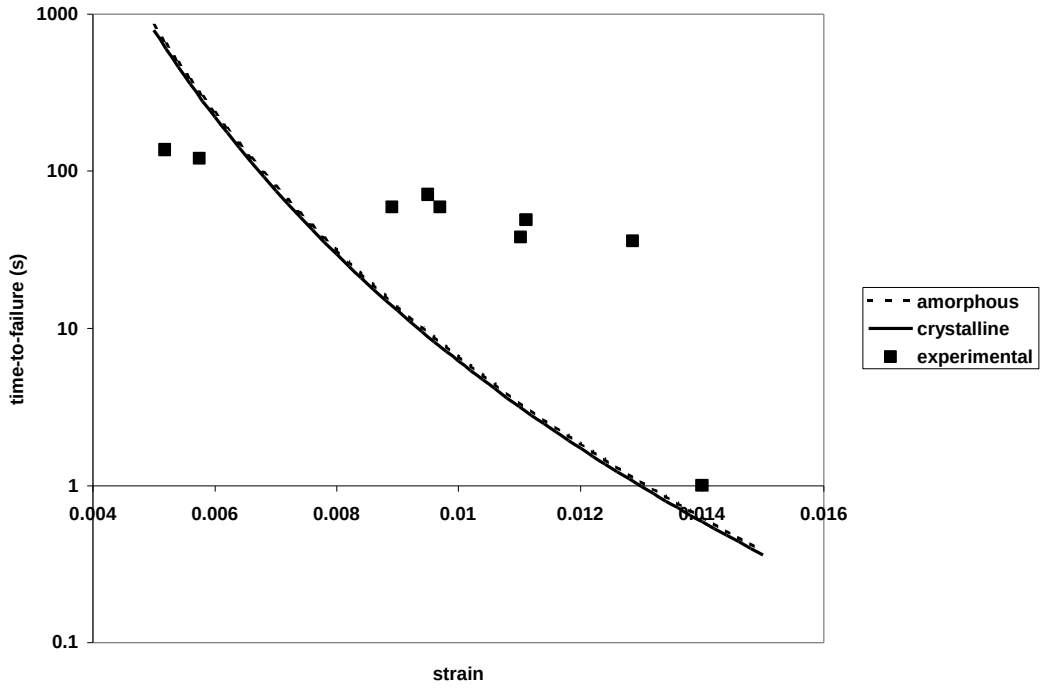


**Figure 65. Time-to-failure versus maximum strain-to-failure for crystalline specimen at 120°C**

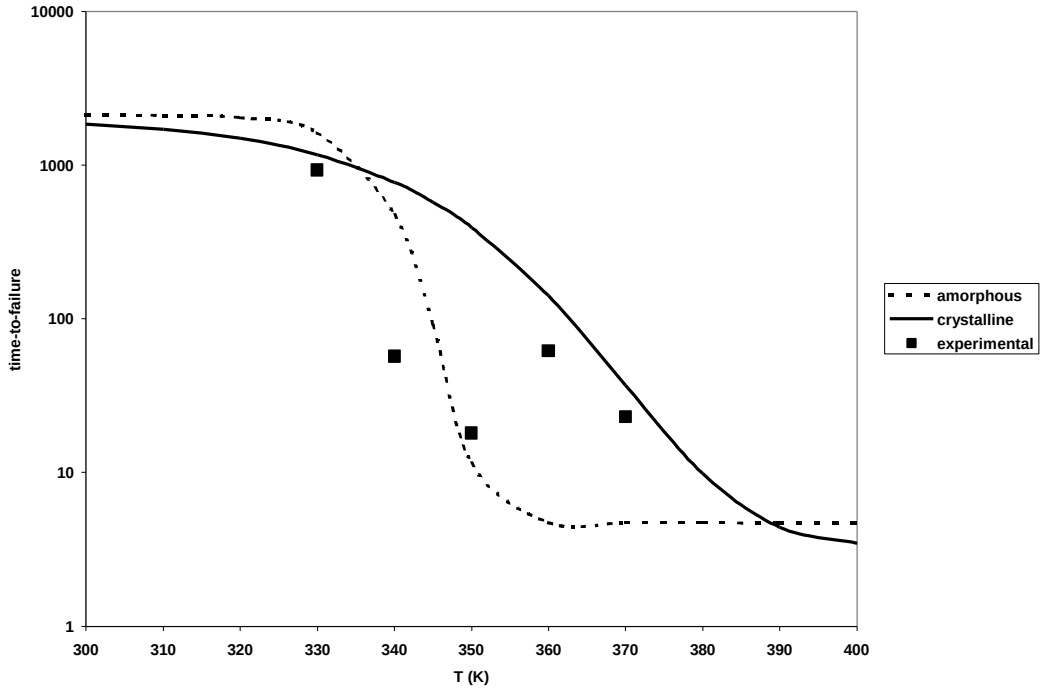


**Figure 66. Time-to-failure versus temperature for amorphous specimen bent at 75% of its maximum tensile strain-to-failure**

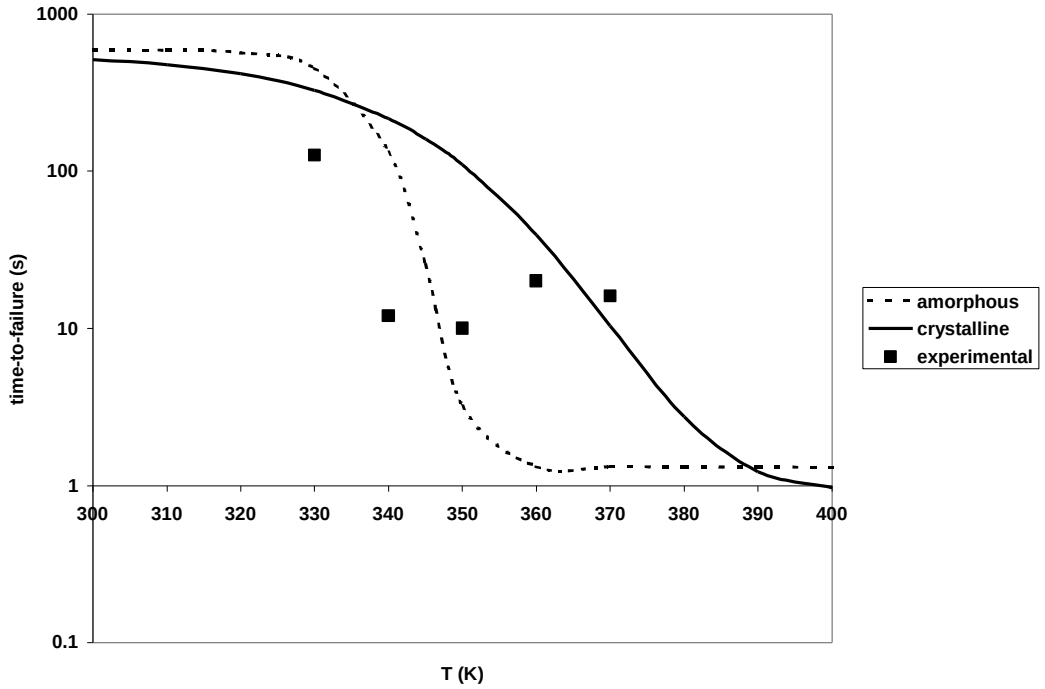


**Figure 67. Time-to-failure versus temperature for amorphous specimen bent at 90% of its maximum strain-to-failure**

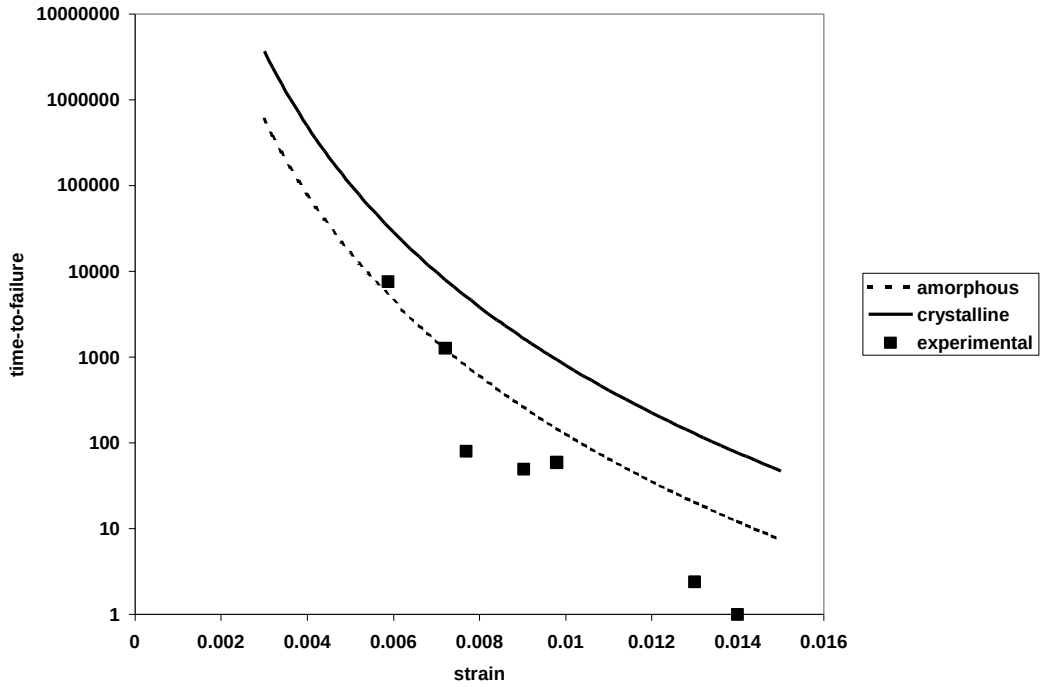


**Figure 68. Time-to-failure versus maximum strain-to-failure for amorphous specimen at 75°C**

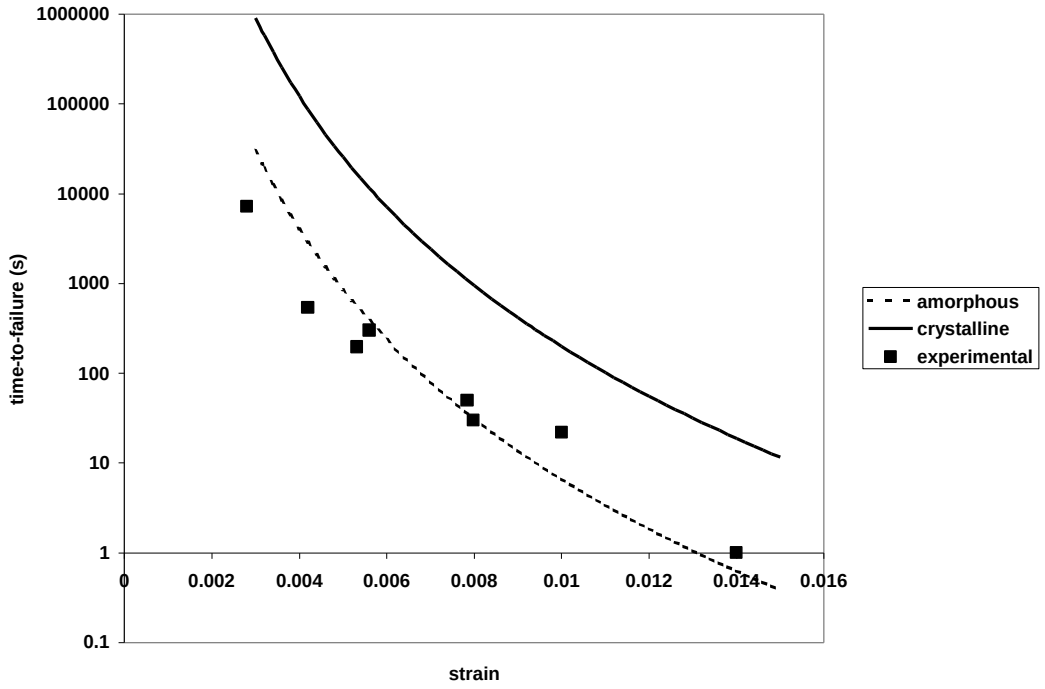


**Figure 69. Time-to-failure versus maximum strain-to-failure for amorphous specimen at 90°C**

### *3.2.4 Discussion*

We will start our discussion by analyzing the two time-to-failure versus strain level (Figure 61) and time-to-failure versus temperature (Figure 62) master curves. The isostrain condition leads to complex results. For all strain levels we can observe the presence of a plateau at high temperatures followed by a transition region, where the time-to-failure increases rapidly as the temperature decreases. Finally for low temperatures the curves describe another transition. These curves are similar to the shape of the modulus versus temperature (or time) master curves for the neat polymer. For high temperatures, the times-to-failure of the composite including the crystalline matrix are much higher than the times-to-failure of the composite made of amorphous resin. However, in the transition region, the curves intersect, and around room temperature the trend is inverted. At very low temperatures the modulus of the crystalline materials becomes higher again. This inversion in the transition region can be explained by the variations of the reference shear stress illustrated by Figure 60. The shear stress is

expressed via the statistical coefficients of the pure matrix. We remember that the Weibull coefficient associated with the glass transition was 20 in the case of the crystalline polymer and 60 for the amorphous material. Therefore, the transition region of the amorphous material is much steeper than the crystalline one. As we used the same $\mu_i$ (Equation 26) to describe the amplitude of the shear stress for the two cases, the inversion can not be compensated. As all our stress-rupture data were taken above room temperature, this trend can not be clearly verified from our data.

An encouraging result of this analysis is that the difference observed between the time-to-failure of the amorphous and crystalline composites at high temperatures (above the transition region) is driven by the matrix-versus-temperature equation (Equation 52), the effect of the efficiency factor being negligible in that case. The experimental results also follow this trend, as we will discuss below.

The shapes of the time-to-failure versus strain level curves at different temperatures are different than the ones described above. The curves are parabolic and do not exhibit the presence of a plateau. At high temperatures the crystalline and amorphous curves superimpose, while at lower temperatures, the curves become distinct, the crystalline curve giving higher times-to-failure. The difference between the 30°C and the 90°C curves is greater than the difference between the 90°C and the 200°C curves. After Tg, as the temperature increases again, a saturation temperature is reached, where a large difference in temperature does not lead to a significant difference in the resulting time-to-failure for any strain level.

The curves comparing the experimental results to our theoretical model are very encouraging. One must note that in order to generate curves close to the experimental data, the temperature $T_2$ (Equation 52) representing (in the present case) the glass transition temperature had to be reduced by 20°C ($T_2=T_g-20$). The introduction of this material constant needs further examination, but is beyond the scope of our present discussion.

Let us first focus on the isostrain experimental sets (Figure 63, Figure 66, and Figure 67). At 90% of their tensile maximum strain-to-failure, experimental data taken on the crystalline composite samples exhibit a life around three times longer than that of the amorphous composite. This difference is also reflected by the difference in the

theoretical results obtained when the composite life is calculated using the amorphous matrix properties and the crystalline properties. As was pointed out earlier in our discussion, no factor has been adjusted, and these results reflect the sensitivity of our model to the matrix modulus versus temperature description. The model also correlates well the data taken for the amorphous specimens bent at 75% of their maximum strain-to-failure (Figure 66). This is a very encouraging result considering the difference of time scale between these experiments (for the amorphous composite bent at 90%, the time-to-failure at 60°C is around 130 seconds, while at 75%, the time to failure jumps to 1000 seconds). These trends are followed by our model and the overall shape of the curve follows the experimental data. However, the fit is not perfect: at high temperatures, the times-to-failure predicted are lower than the experimental data. A possible explanation is that when the specimen is put in the oven, the temperature of the composite varies between room temperature to the temperature of the oven. At high temperatures, the time-to-failure can be extremely short and the temperature of the material might not have enough time to reach the temperature of the oven. In any case, the specimen spends some time at a lower temperature, leading to a longer life. The discrepancy would be amplified at high temperatures for high strain levels (shorter lives). The correlation between experimental data and theoretical results is better for the specimens bent at 75% than at 90% and seems to support this assumption (Figure 66 and Figure 67).

Similar types of comments can be made for the isotemperature experiments: the effect of crystallinity introduced in the description of the modulus versus temperature model for the matrix influences the time-to-failure towards higher values. The model using crystalline properties describes the results obtained on the crystalline composite best (Figure 64 and Figure 65) and the model using the amorphous properties for the matrix describe the results obtained for the amorphous composite (Figure 68 and Figure 69). Once again, the fit is not perfect but the scales represented vary from 120 seconds (crystalline specimen at 120°C) to 8000 seconds (amorphous specimen at 75°C) for the time-to-failure at a 0.005 strain level. Therefore, the overall behavior of the model seems to be correct. Some of the discrepancies (at low strain levels or low temperatures) can be explained by the presence of multiple microbuckles in the specimen. To obtain a better understanding of how the microbuckles nucleate and propagate, the underneath of a

crystalline specimen (compressive side) was videotaped during the stress rupture experiments in the oven. The specimen was bent at 50% of the maximum bending strain-to-failure at the mid-span, and placed in the oven at 120°C. After one minute at temperature, the first microbuckle initiated (Figure 70 a[48]). The next microbuckles appeared on one edge but were not located in the middle of the specimen (region of highest stress level). Then these first microbuckles stopped propagating and other microbuckles appeared on both edges of the specimen (Figure 70 b,c,d,e,f). During the final seconds before failure, one of the microbuckles ("fatal" microbuckle), located at a point of higher stress level (middle of the specimen) grew slowly, stopped for a short moment, then propagated very rapidly across the width of the specimen inducing fracture (Figure 70 g).

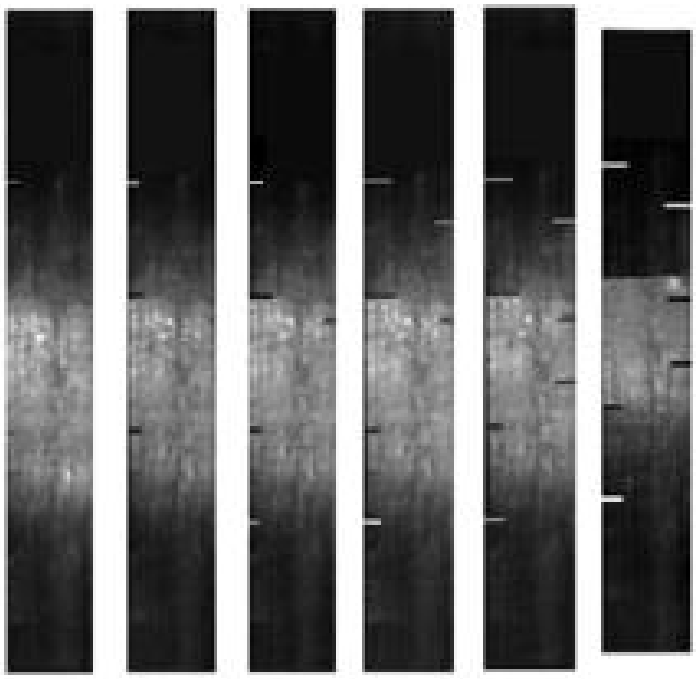

**a b c d e f**

**Figure 70. Underneath of the bent specimen in oven (sequence of events). a. at 60 seconds, b. at 75 seconds, c. at 80 seconds, d. at 85 seconds, e. at 90 seconds, f. at 92 seconds. From Mahieux et. al.**[48]

Budiansky's model[83] only considers the presence of one microbuckle. At very high strain levels, only one microbuckle forms and induces failure. At low strain levels a

multitude of microbuckles form as previously discussed. These microbuckles and their influence on the fatal microbuckle were not taken into consideration in the micromechanical model used to generate the data and might explain some of the discrepancies observed between the model and experimental data.

Despite discrepancies probably due to the micromechanical model used to describe the compressive failure process, the results are extremely encouraging. The temperature dependence of the tensile modulus and life of a bent specimen have been described for eight independent sets of experiments.

The next step to this study is to introduce cyclic loading and incorporate Equation 52 into composite life prediction models.

## 3.3 Fatigue and life prediction

### *3.3.1 Experimental work*

#### *3.3.1.1 Fatigue*

##### 3.3.1.1.1 Experimental apparatus

In order to investigate the effect of combined cyclic and thermal loading in end-loaded bending and to allowed comparison with quasi-static data, the same mode of loading (end-loaded) was chosen. A new type of fixture was developed. The fixture designed by Pipik et. al.[85] and shown in Figure 71 was made from aluminum and stainless steel, which is resistant to corrosion and can withstand the heat range over which the specimens were tested.

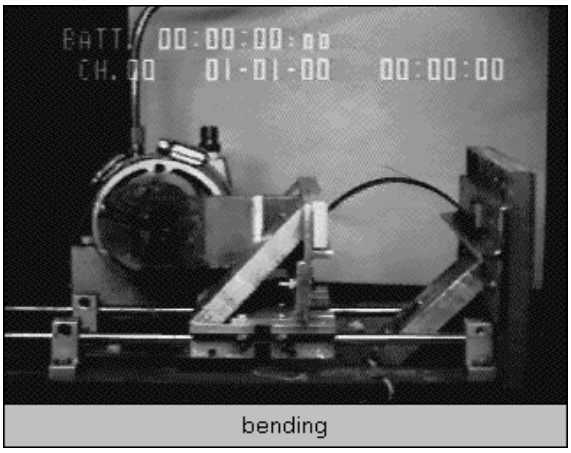


**Figure 71. End-loaded fatigue fixture from Jackson et. al.**[86]

Details of the fixture design were given by Pipik[85]: "the push rod assembly has a slot mounted on the end of a push rod, which is attached to one of the end pieces. The pin fits into copper bushings, and then into the slot, converting the rotational motion of the motor to a sinusoidal linear motion of the end piece. At the other end of the linear rails is another end piece, which holds the other end of the specimen in place.

The air motor and linear rail system were purchased from outside vendors, and were made of stainless steel and aluminum. The linear rail system, which is intended to keep the end piece and push rod from torquing, was made from hardened stainless steel and aluminum. The air motor was chosen over an electrical motor because it would survive better in a 90°C oven for the extended periods of time that these tests require. Also, access to an air supply near the oven allowed the motor to fit into the existing lab setup without requiring complex modifications" (Figure 72 and Figure 73).

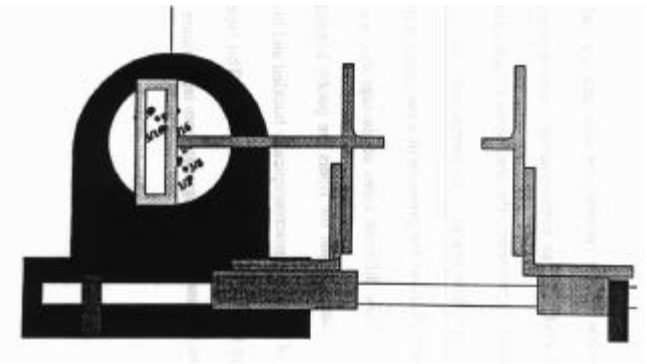

**Figure 72. Fatigue machine schematic. From Pipik**[85]

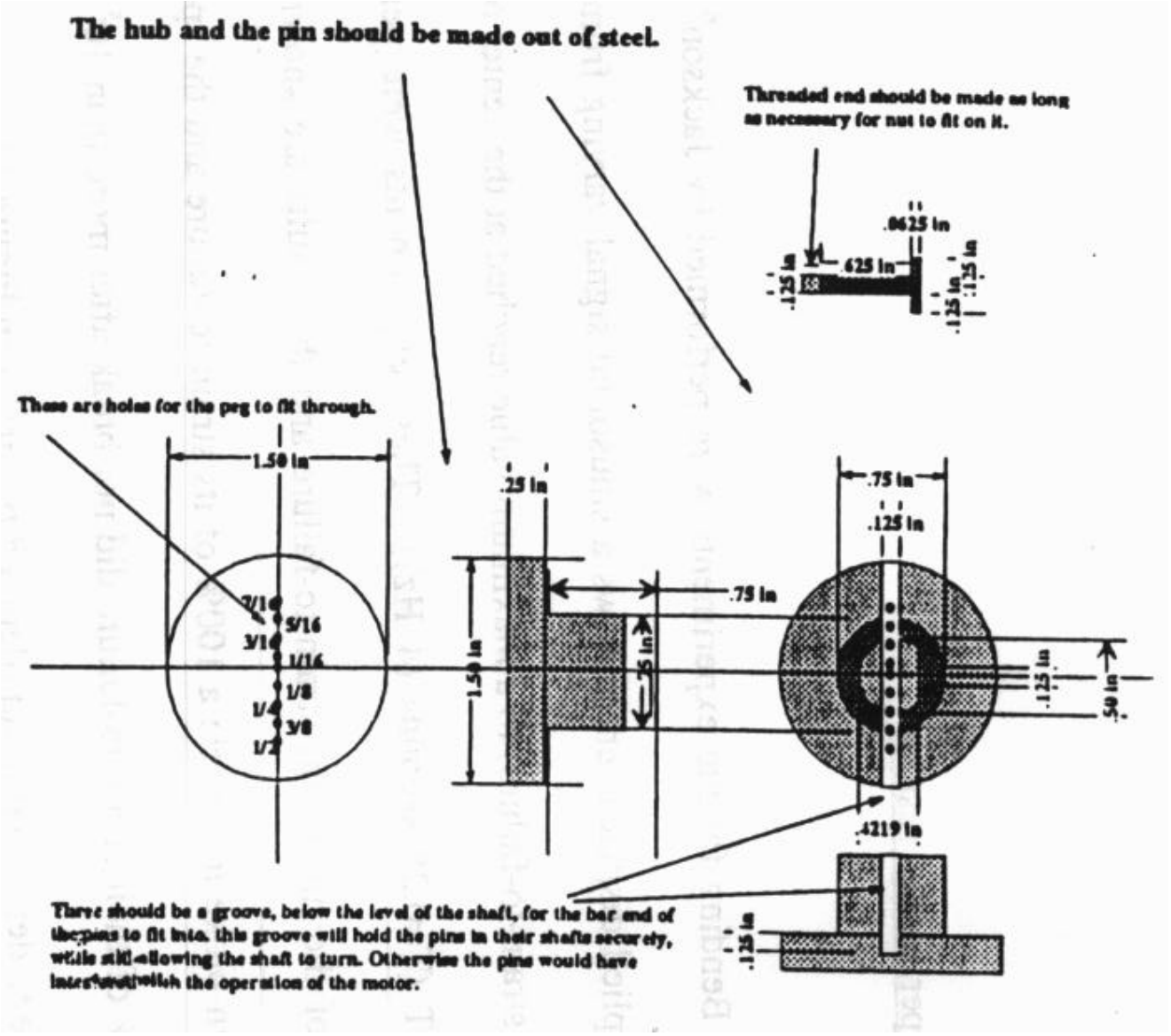


**Figure 73. Fatigue machine schematic (details)**[85]

3.3.1.1.2 Experimental results

Unidirectional AS4/PPS composites with an amorphous matrix were tested in fatigue The applied displacement varies sinusoidally from a small compression (3% of strain-to-failure) to a maximum value reached at the center of the specimen ($\varepsilon_{max}$) with a period T (T=0.25 seconds (4 Hz)). The normalized strain (Figure 74 to Figure 84) corresponds to the maximum strain at the mid-length of the specimen divided by the ultimate strain to failure at room temperature. The experiments included:

-Room temperature fatigue for various $\varepsilon_{max}$. The specimens were tested at very high strain levels. At room temperature, no failure was recorded below 90% of the ultimate strain to failure (the experiments were stopped after 100000 cycles that will define a run-out). The results are shown in Figure 74.

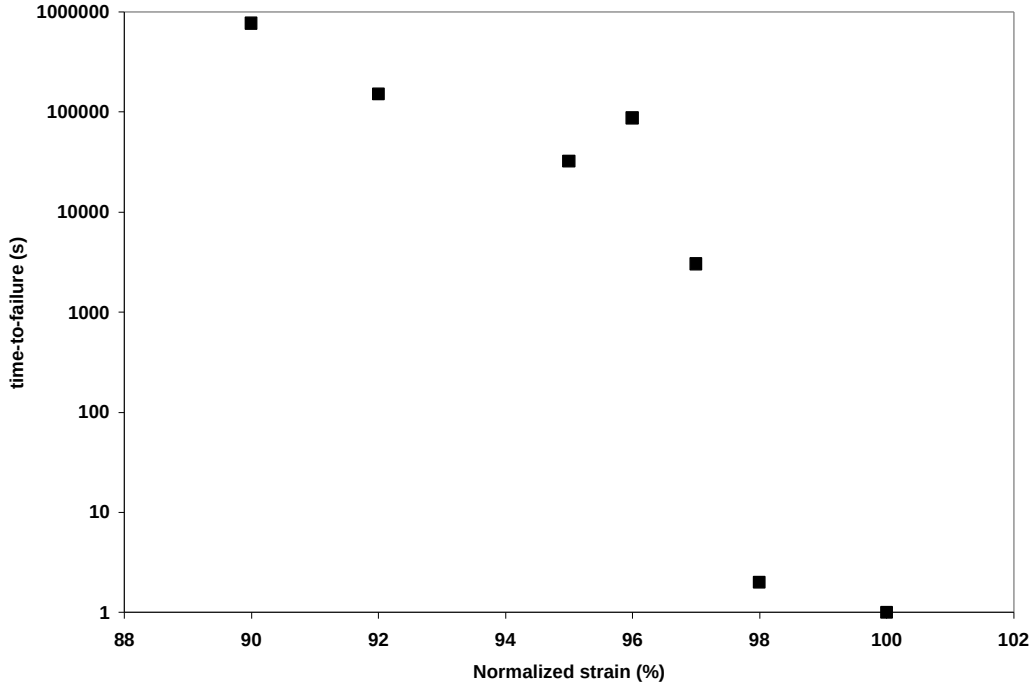


**Figure 74. Room temperature End-loaded fatigue experiments**

Observations of the compression side and the failure surface of the broken specimens were made with an environmental scanning electron microscope. The compression side was severely damaged by the cyclic load. Figure 75 shows the

presence of a microbuckle initiating from the edge. But Figure 76 and Figure 77 show different types of damage that were not observed at elevated temperature. One can note that the fibers are poorly bonded to the matrix. Figure 78 shows a bundle of fibers that macroscopically buckled and broke. The fibers are clearly crushed, resulting from a compressive cyclic load. This type of damage was only seen on specimens that underwent fatigue at room temperature.

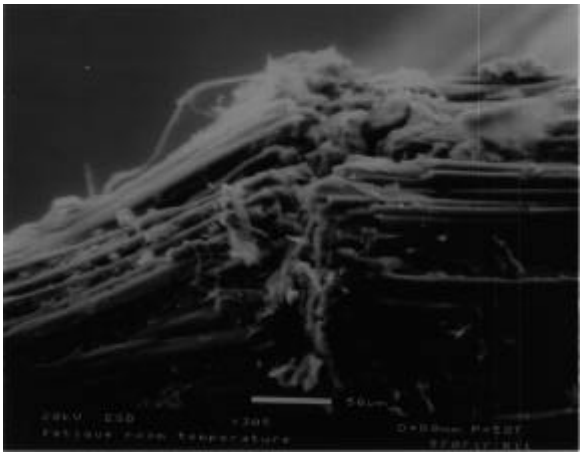

**Figure 75. SEM picture. Room temperature bending fatigue. Microbuckle on the compression side**

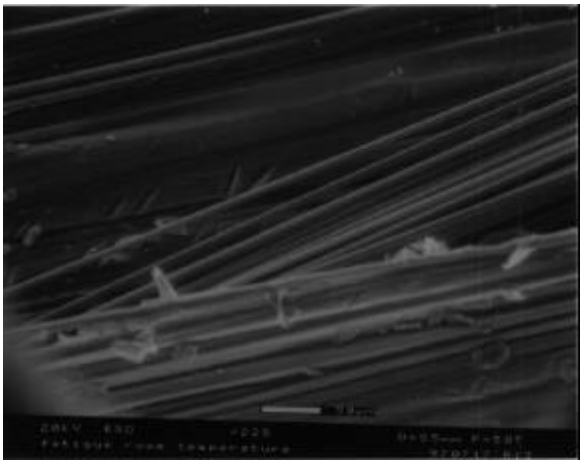

**Figure 76. SEM picture. Room temperature bending fatigue. Damage on the compression side**

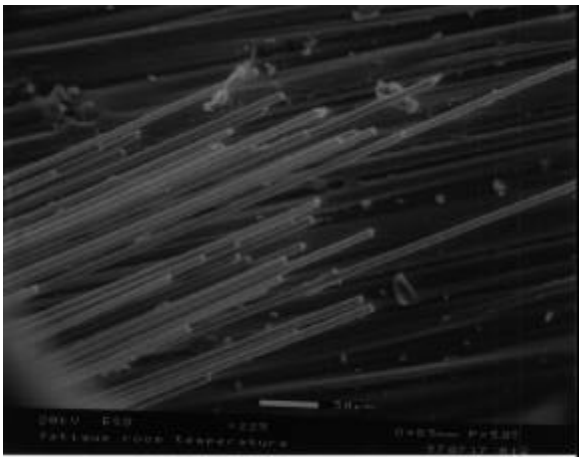

**Figure 77. SEM picture. Room temperature bending fatigue. Damage on the compression side**

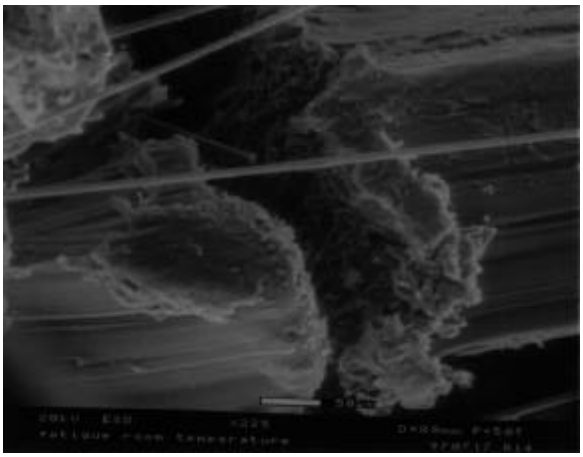

**Figure 78. SEM picture. Room temperature bending fatigue. Damage on the compression side**

-Fatigue bending at 75°C and 90°C for various $\varepsilon_{max}$. The results are shown in Figure 79 and Figure 80.

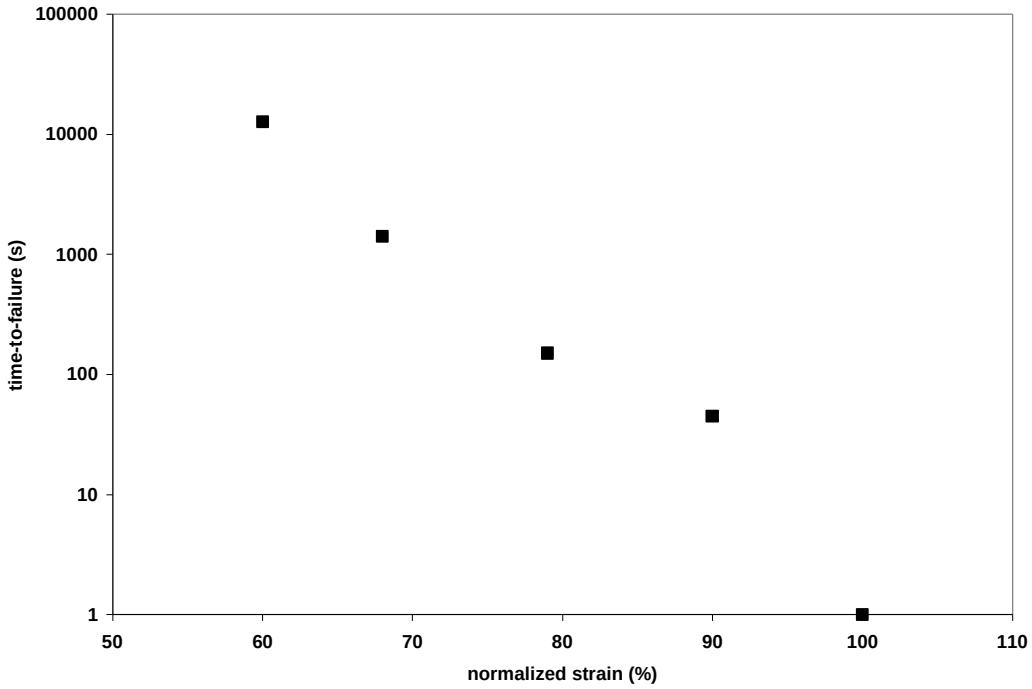


**Figure 79. End-loaded fatigue experiments at 75°C**

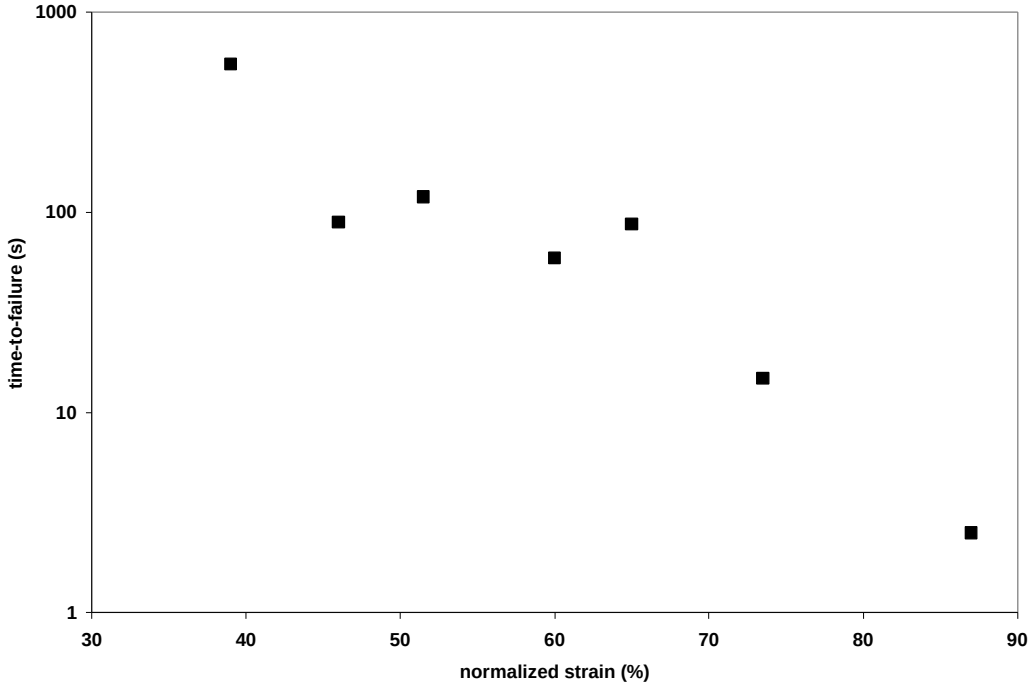


**Figure 80. End-loaded fatigue experiments at 90°C**

In the scanning electron microscope, no damage could be seen on the tension side of a specimen broken at 90°C in fatigue and unlike bending fatigue at room temperature, the compression surface looked very similar to the quasi-static case. The micrograph shown in Figure 82 was taken close to the failure surface. Out-of plane microbuckling is clearly apparent. One can also notice the change of plane of the microbuckle (convex then concave). This would corroborate the presence of discontinuities that would influence the propagation of the microbuckles. Other shallower microbuckles can also be found further from the failure location (Figure 81).

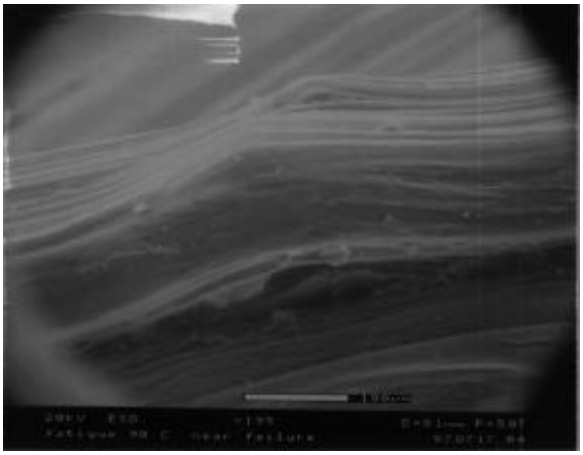

**Figure 81. SEM picture. 90°C bending fatigue. Microbuckle on the compression side**

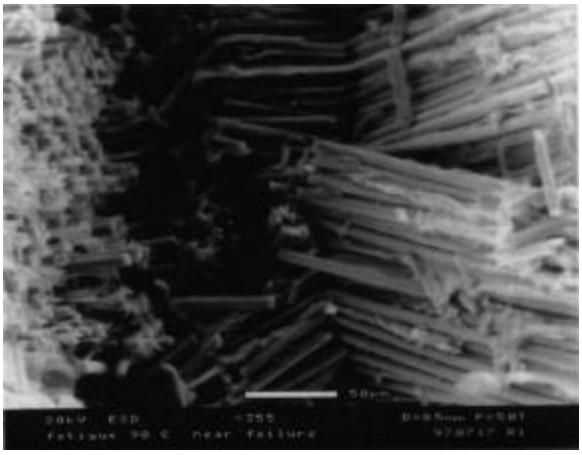

**Figure 82. SEM picture. 90°C bending fatigue. Microbuckle on the compression side**

-Fatigue bending at $\varepsilon_{max}$ =90% and $\varepsilon_{max}$ =75% for various temperatures. The results are shown in Figure 83 and Figure 84.

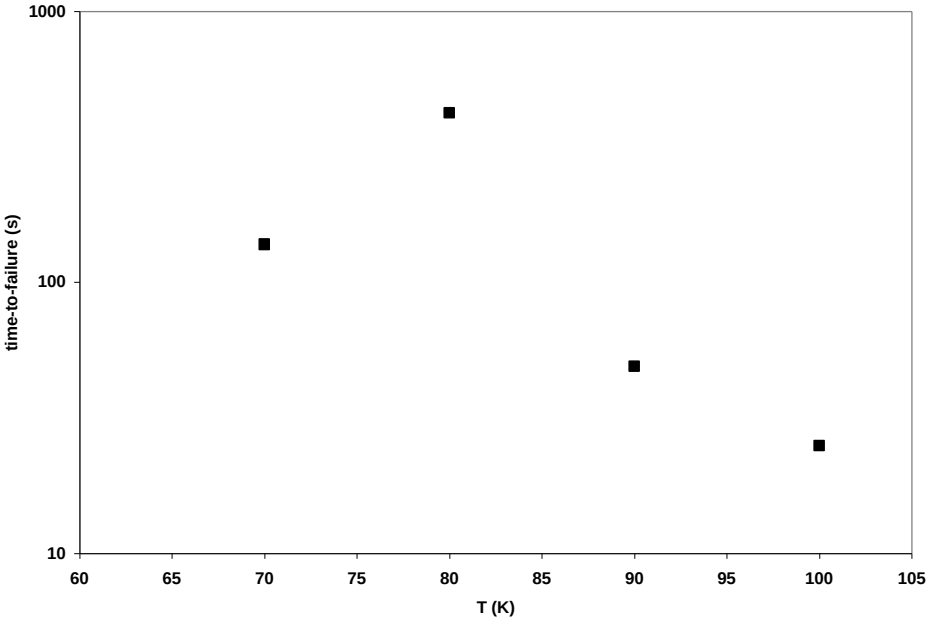


**Figure 83. End-loaded fatigue experiments at 75%**

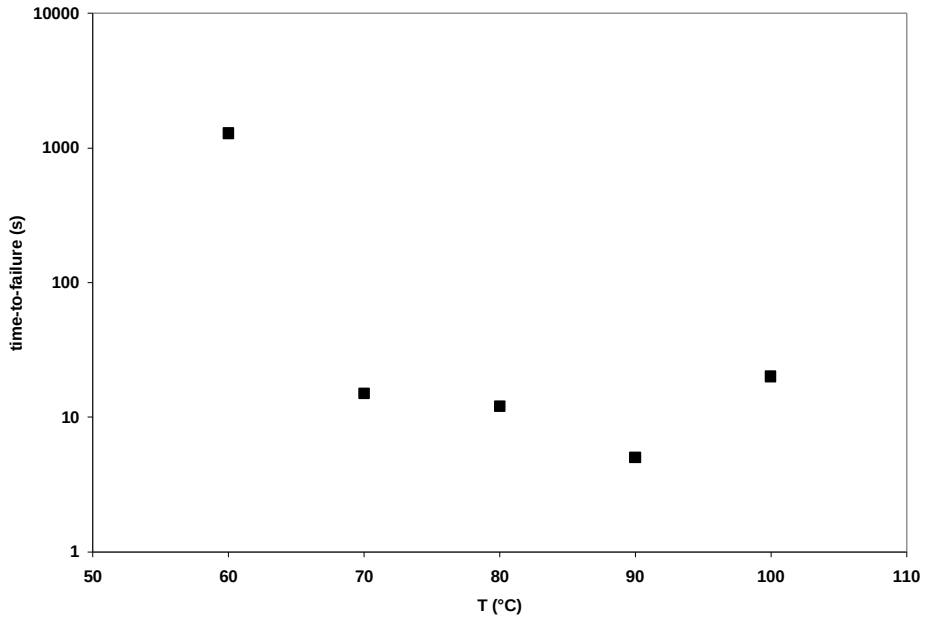


**Figure 84. End-loaded fatigue experiments at 90%**

The purpose of the following section is to predict the isostrain data at 75% and 90%, as well as the isotemperature data at 75°C and 90°C.

*3.3.1.2 Stress rupture and remaining strength*

End-loaded bending stress-rupture data are available from our previous experiments (section 3.2) for the amorphous material. An explicit relationship between the time-to-failure, the strain and temperature has also been established for the static experiments (Equation 87).

In order to use a life prediction code called MRLife[52], and predict the life of the composite under cyclic loading at elevated temperatures, we also need to characterize the strength degradation of the composite during the end-loaded static experiments. Remaining-strength experiments were conducted on the amorphous composite: a series of specimens were bent at 38% of their ultimate tensile strain-to-failure. They were taken out of the oven before failure. Quasi-static remaining strength experiments were performed in tension at a loading rate of 50 lbs per second and the ultimate load-to-failure was recorded. The same experiments were performed with specimens bent at 57% of their ultimate strain-to-failure. As intuitively expected, the remaining strength decreased as the time spent in the oven increased (Figure 85, Figure 86).

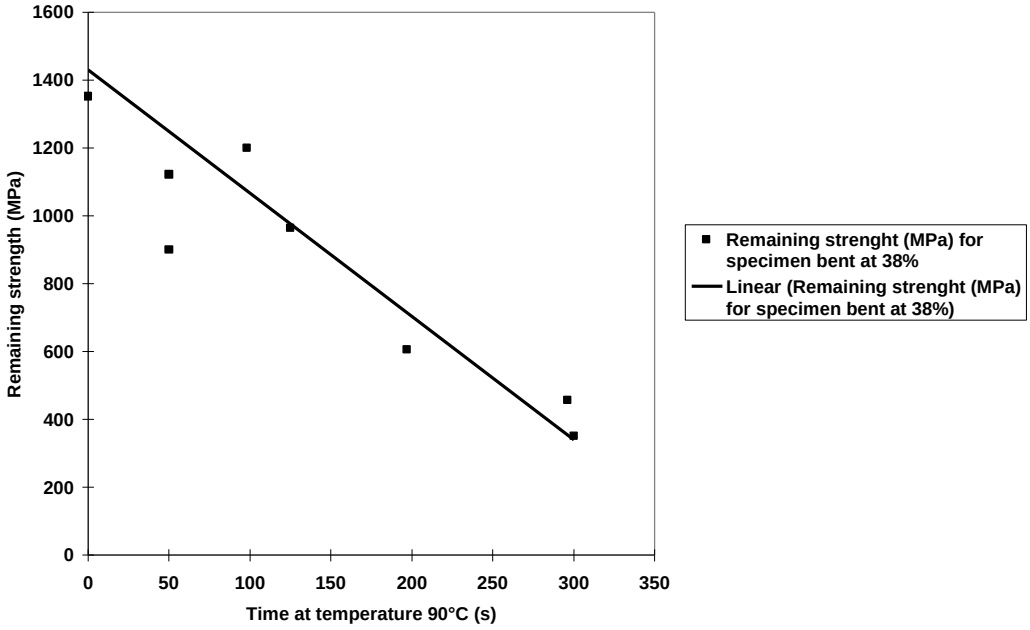


**Figure 85. Remaining strength. Stress rupture experiments at 90°C and 38% strain-to-failure**

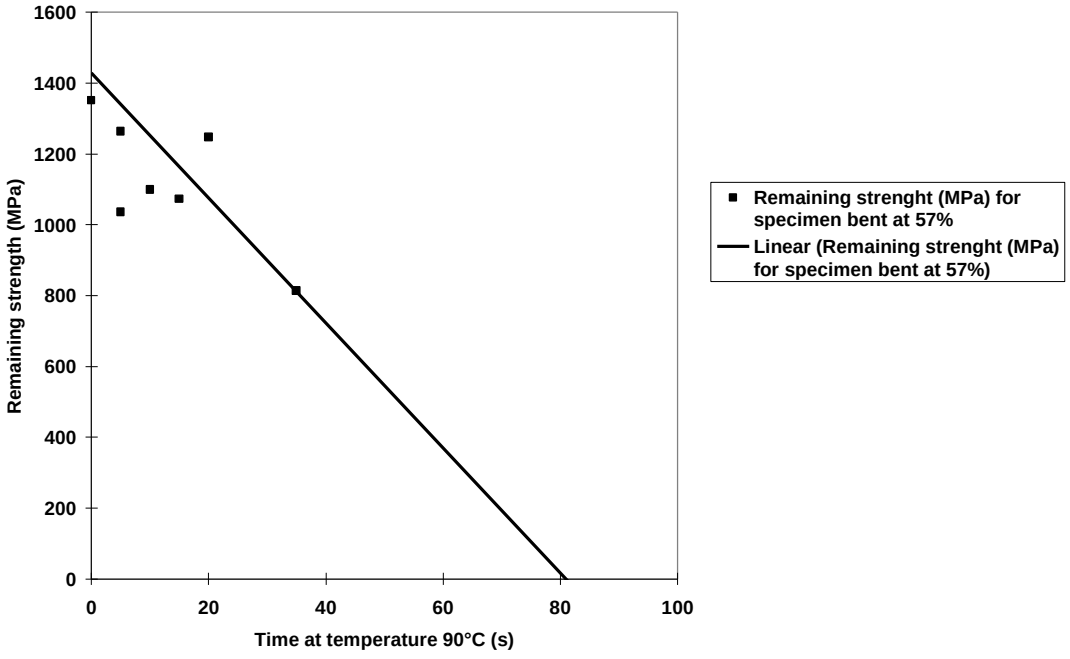


**Figure 86. Remaining strength. Stress rupture experiments at 90°C and 57% strain-to-failure**

### *3.3.2 Modeling and results*

The purpose of this section is to analytically combine the theoretical results obtained for the quasi-static experiments at elevated temperatures in bending (section 3.2) with the results of the room-temperature fatigue experiments in bending (section 3.3.1.1.2) to predict the life our unidirectional carbon fiber polymer matrix composites under bending fatigue at elevated temperatures.

#### *3.3.2.1 The MRLife concept*

The MRLife™ concept was introduced by Reifsnider and Stinchomb[52]. The first step for this analysis is to define a failure function, Fa. Maximum strain (strain over ultimate strain-to-failure) is a logical failure criterion for our case. The continuity function ψ can be defined by:

**Equation 88**

$$y = 1 - Fa$$

A general kinetic law is postulated:

**Equation 89**

$$\frac{dy}{dt} = y\, j\, t^{j-1}$$

where j is a material parameter and

**Equation 90**

$$t = \frac{t}{\hat{t}}$$

where $\hat{t}$ is a characteristic time. In the case of the quasi-static experiments, the characteristic time is the creep rupture life and in the case of fatigue:

**Equation 91**

$$t = \frac{n}{N}$$

where n is the number of cycles and N the number of cycles to failure.

After some mathematical manipulations the remaining strength can be expressed by the remaining strength integral[52]:

**Equation 92**

$$Fr = 1 - \int_0^t (1 - Fa(t))\, j\, t^{\,j-1} dt$$

*3.3.2.2 The incremental approach*

The problem in our case is the sinusoidal variation of the failure function. To deal with this problem and combine the effects of creep and fatigue, an incremental approach introduced by Case et. al.[53] was used. From Case[53], for a constant Fa applied, one can write:

**Equation 93**

$$Fr = 1 - (1 - Fa)t^{\,j}$$

If we consider a first-loading process at a constant $Fa_1$ for a time $\tau_1$ resulting in a remaining strength Fr followed by a load $Fa_2$, we can write the time that would have been necessary to cause an equivalent amount of damage at this second load level (pseudo time, $t_2^o$):

**Equation 94**

$$t_2^o = \left(\frac{1 - Fr}{1 - Fa_2}\right)^{\frac{1}{j}}$$

Over an interval of loading the remaining strength can be written as:

**Equation 95**

$$\Delta Fr = -(1 - Fa_2)\left\{\left(\frac{t_2^0 + \Delta t}{\hat{t}_2}\right)^j - \left(\frac{t_2^0}{\hat{t}_2}\right)^j\right\}$$

Where $t^o{}_2$ is the unormalized pseudo time:

**Equation 96**

$$t_2^0 = \hat{t}_2 t_2^0$$

Finally the remaining strength can be written as

**Equation 97**

$$Fr = 1 - \sum_{i=1}^{i=N_{blocks}} \Delta Fr_i$$

Using Equation 97, it is possible to use an incremental approach to the problem. The failure function Fa is shown in Figure 87 and can be represented by the following equation:

**Equation 98**

$$Fa = \frac{Fa_{\max} - Fa_{\min}}{2}\sin(\frac{2pt}{T} - \frac{p}{2}) + \frac{Fa_{\max} + Fa_{\min}}{2}$$

where T is the period. On the loading portion ($Fa_{min}<Fa<Fa_{max}$) the influence of creep on the remaining strength of the specimen can be computed assuming the failure function to be constant and equal to its average value over the half-period of time. The half period is then divided into an increasing number of steps where the average failure function can be written as:

**Equation 99**

$$Fa_{average} = \frac{aT}{2p\Delta t}(\cos(\frac{2pt}{T} - \frac{p}{2}) - \cos(\frac{2pt - \Delta t}{T} - \frac{p}{2}) + b$$

where

**Equations 100**

$$a = \frac{Fa_{\max} - Fa_{\min}}{2}$$

$$b = \frac{Fa_{\max} + Fa_{\min}}{2}$$

until convergence of the remaining strength is obtained.

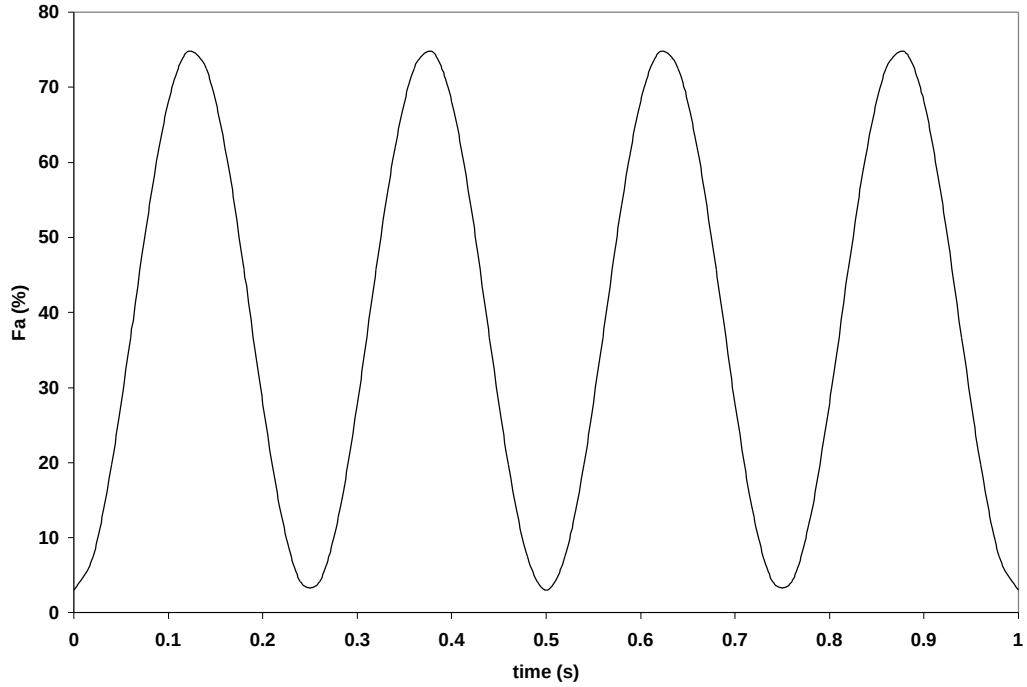


**Figure 87. Sinusoidal variations of the failure function Fa (with $Fa_{max}$=75%)**

At the load reversal, the strength reduction due to fatigue for a half period is applied. Then this process is repeated upon the unloading portion of the failure function.

The algorithm written by Case[87] in FORTRAN was modified for the present case to get the temperature-explicit life prediction as described in the following pages.

*3.3.2.3 Application to fatigue bending at elevated temperature*

The stress rupture data at any temperature can be calculated using Equation 87:

$$t_f = \frac{1}{M-1} \times \frac{1}{\dot{g}_{ref}} \times \left( \frac{\sum_{i=1}^{N} m_i \exp\left( -\left( \frac{T}{T_i} \right)^{m_i} \right)}{E_{11}(T) \times e_{\max}} \right)^M \times \left( \frac{1}{\bar{f}^{M-1}} - \frac{1}{\left( \frac{p}{2} \right)^{M-1}} \right)$$

The failure function Fa was chosen to be related to the applied maximum strain by:

**Equation 101**

$$Fa = \frac{e_{\max}}{e_o}$$

Where $\varepsilon_o$ is the ultimate strain-to-failure.

The remaining strength experiments run at 38% and 57% of the maximum strain-to-failure (Figure 85, Figure 86) enable the computation of the $j_{rupture}$ value according to Equation 102:

**Equation 102**

$$s = 1-(1-Fa)(\frac{t}{t_r})^{j_{rupture}}$$

Both fits led to a value of 0.66 for $j_{rupture}$.

During the bending experiments, the applied displacement varies following a sinusoidal signal varying from a small compression ($Fa_{min}$=0.03) to a maximum value reached at the center of the specimen ($Fa_{max}$) with a period T (T=0.25 seconds). These experiments were performed for different values of $Fa_{max}$ and can be represented by the following equation:

**Equation 103**

$$Fa = 0.9941 \cdot N_f^{-0.0045}$$

Where $N_f$ is the number of cycles to failure ( $N_f \geq 1$).

Experimental data and theoretical results are shown in following figures for the case of the end-loaded fatigue:

- isostrain experiments at 75% for various temperatures (Figure 88)
- isostrain experiments at 90% for various temperatures (Figure 89)
- isotemperature experiments at 75°C for various strain levels (Figure 90)
- isotemperature experiments at 95°C for various strain levels (Figure 91)

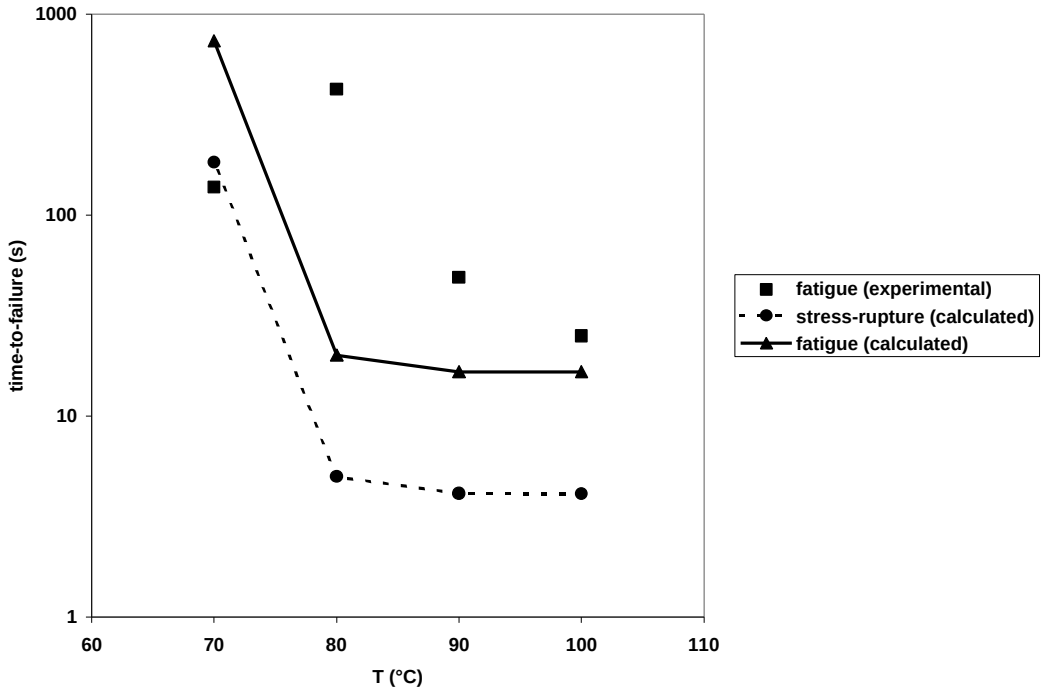


**Figure 88. Isostrain experiments and theoretical results at 75% for various temperatures**

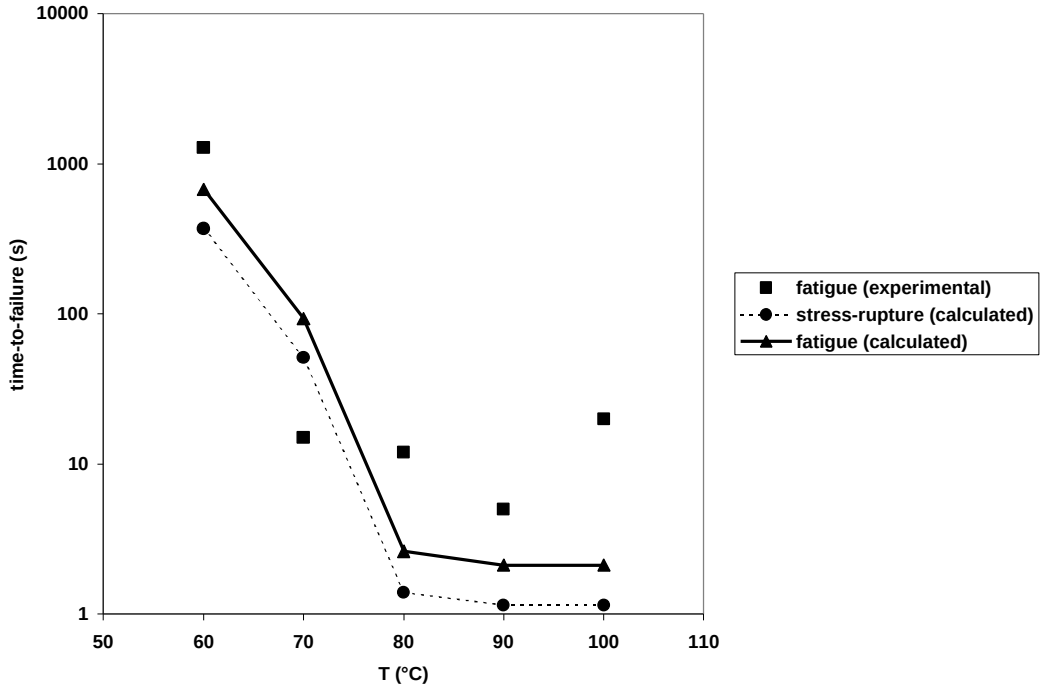


**Figure 89. Isostrain experiments and theoretical restults at 90% for various temperatures**

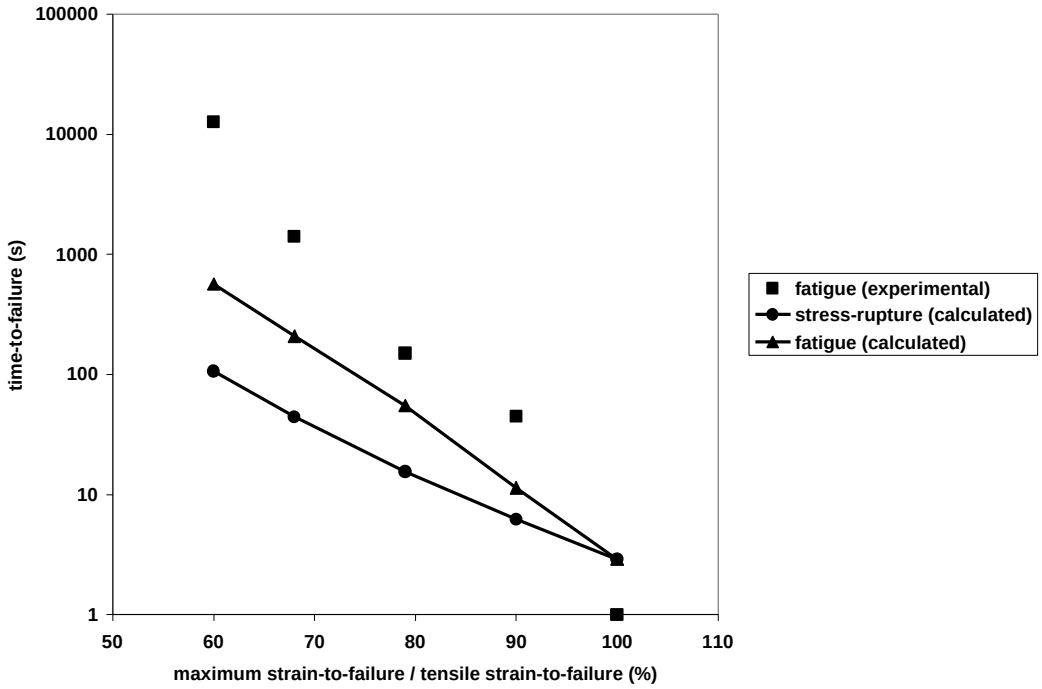


**Figure 90. Isotemperature experiments and theoretical results at 75°C for various strain levels**

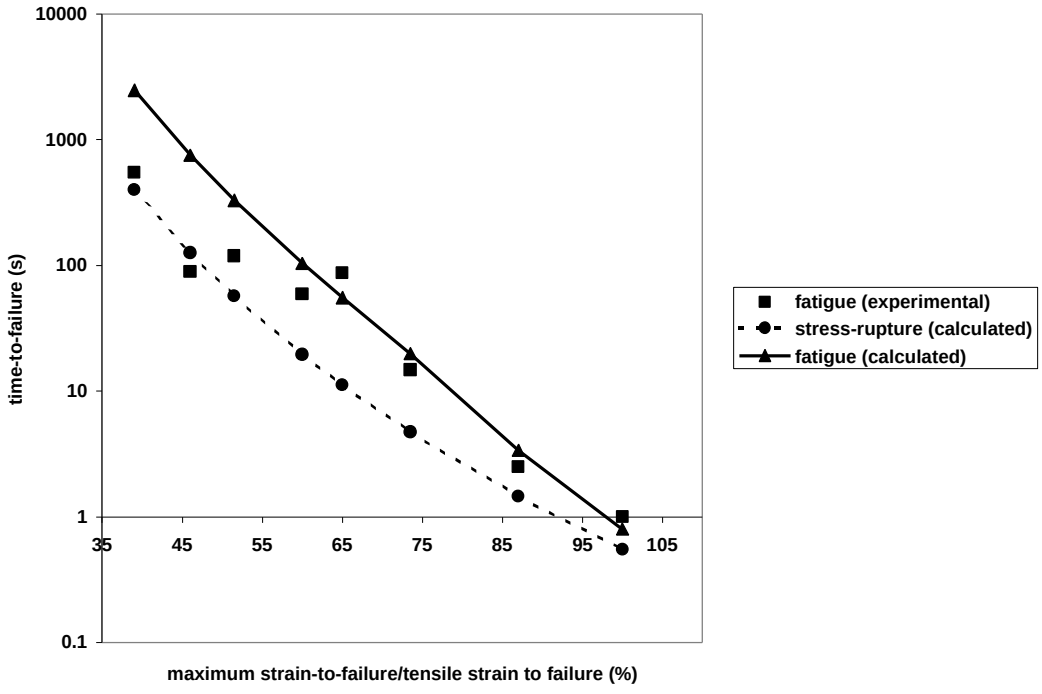


**Figure 91. Isotemperature experiments and theoretical results at 90°C for various strain levels**

*3.3.2.4 Discussion*

The life of the composite in bending fatigue is longer than the life in bending static-load experiments. This result is logical considering the fact that during cyclic loading, the strain varies from 0 to a maximum. The stress rupture effects are therefore less than the ones the composite would see if the load was constantly maximum. The MRLife results reflect this concept and predict longer lives for the fatigued specimen.

Let us compare the failure surfaces for the cases of stress rupture (Figure 92), bending fatigue (Figure 93) and bending fatigue at elevated temperatures (Figure 94).

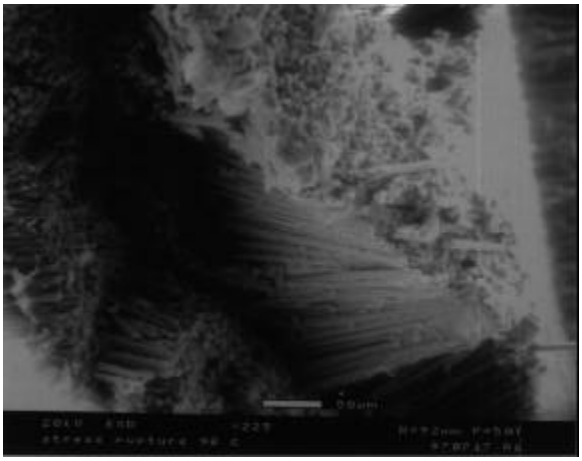

**Figure 92. SEM picture. Stress rupture at 90°C. Failure surface**

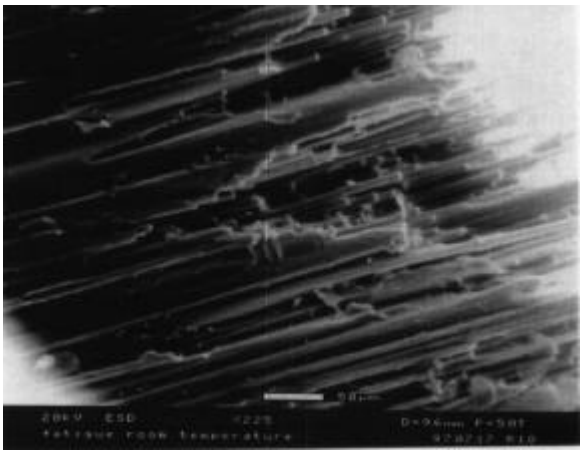

**Figure 93. SEM picture. Room temperature bending fatigue. Failure surface**

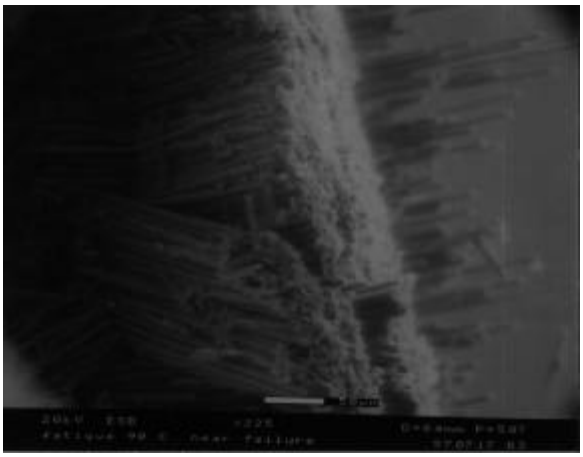

**Figure 94. SEM picture. Bending fatigue at 90°C. Failure surface**

The failure surface of the specimen broken in fatigue at elevated temperature is very similar to the one observed in the stress rupture experiments. A large compressive failure contribution and the presence of a very flat failure surface resulting from an unstable damage growth can be noted. The failure surface of the specimen broken at room temperature seems very different and does not seem to be affected by the local compressive situation. From these observations, it seems that high temperature fatigue experiments lead to lives close to the stress rupture lives, while lower temperatures (below the glass transition temperature) lead to long lives (dominated by the fatigue effects). This trend is clearly observed on the experimental results: at 90°C stress rupture data and fatigue data almost superimpose (Figure 90) while at 75 °C stress rupture and fatigue data (Figure 91) are distinct (longer fatigue lives).

For the isotemperature data, the theoretical results follow the global trend experimentally observed. At 90°C (Figure 91) the fit is good. But at 75°C (Figure 90), the model does not match the experimental time-to-failure recorded for low applied strains. This can be explained by the difficulty previously encountered in fitting the stress-rupture model to the experimental data for low temperatures and low strain levels (section 3.2.2.2): at high temperatures and high strain levels, failure is due to the presence of a single microbuckle, while at lower strain levels and temperatures, several microbuckles appear, that were not considered into our analysis.

For the isostrain data shown in Figure 88 and Figure 89, the model also follows the shape of the experimental data: a steep drop can be observed at temperatures around the glass transition, followed by a plateau. For temperatures above $T_g$ the model slightly underpredicts the life of the composite for $\varepsilon_{max}$ equal 75% and 90%. This result is logical due to the fact that the stress rupture model leads to shorter lives than the experiments for high temperatures. We explained this discrepancy (section 3.2.2.2) by the fact that the specimens do not reach high temperatures instantaneously; therefore, the samples see lower temperatures for a small amount of time, allowing longer experimental lives.

Once again, no parameters were adjusted in order to perform the predictions. This independent set of experiments illustrates the feasibility of making life prediction models for composites explicit in temperature, thanks to the stretched exponential developed for the neat polymers.

## 3.4 Classical Lamination Theory

The purpose of the present section is to illustrate the feasibility of integrating the stretched exponential (Equation 52) into Classical Lamination Theory[81] in order to make macromechanics models explicit in temperature.

### *3.4.1 AS4/PEEK laminate*

We consider an 8 ply symmetric laminate:

$$[AS4/PEEK_{45^\circ}, AS4/PEEK_{0^\circ}, AS4/PEEK_{-45^\circ}, AS4/PEEK_{90^\circ}]_s.$$

For the numerical applications, the properties of the constituents and volume fractions were kept at the same values as the ones used in section 3.1. The micromechanical models developed in this previous section were used to compute the longitudinal and transverse modulus of each ply (Equation 74, Equation 76, and Equation 77). The Poisson's ratio $\upsilon_{12}$, and the thermal expansion coefficient of the plies were assumed to be constant with respect to temperature. The thickness of the plies was taken equal to 14mm. The elastic moduli in the composite coordinates (x-y) are shown in Figure 95.

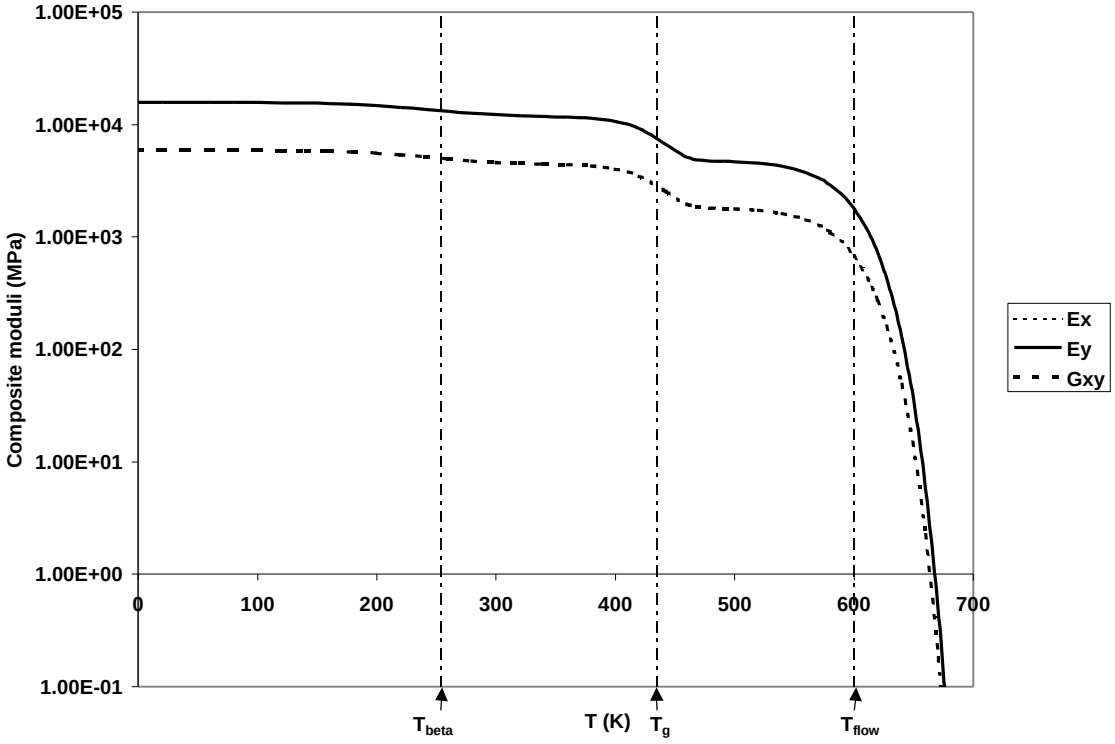


**Figure 95. $E_x$, $E_y$ and $G_{xy}$ versus temperature for the [AS4/PEEK$_{45°}$, AS4/PEEK$_{0°}$, AS4/PEEK$_{-45°}$, AS4/PEEK$_{90°}$]$_s$ laminate.**

The moduli decrease monotonically as a function of temperature, following a curve similar to the neat polymer: the different transitions are clearly present. Poisson's ratio for the entire laminate and in the laminate coordinates (x-y) is shown in Figure 96.

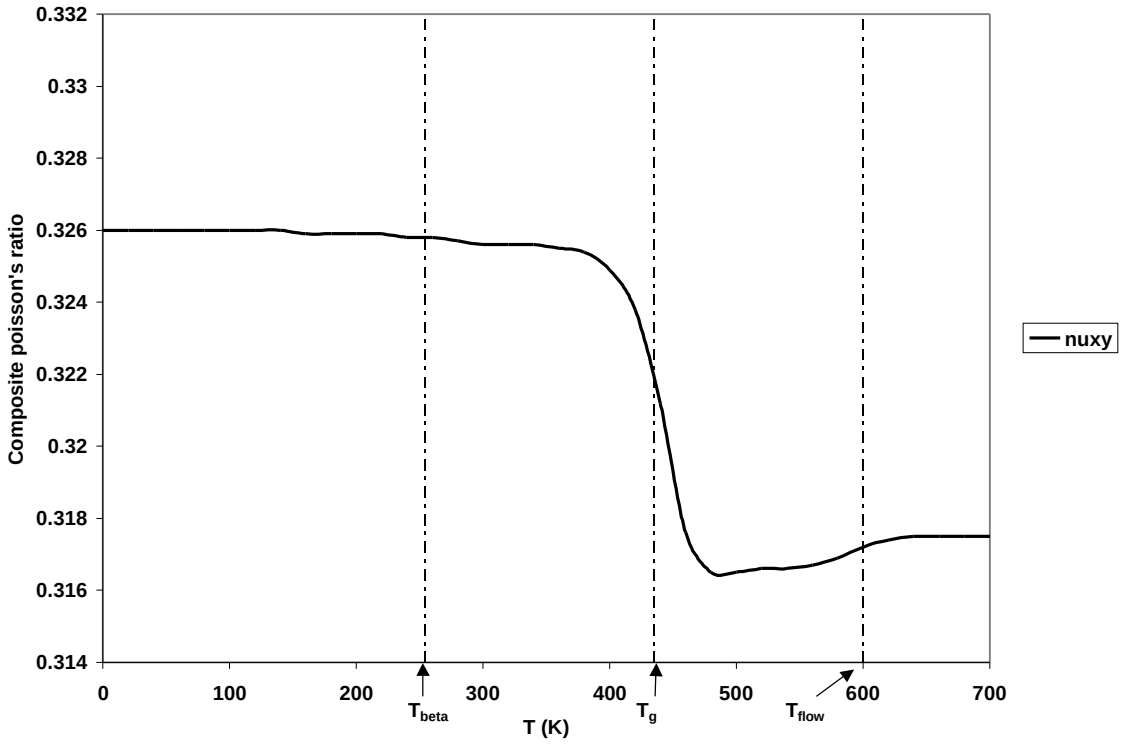


**Figure 96. $u_{xy}$ versus temperature for the [AS4/PEEK$_{45°}$ , AS4/PEEK$_{0°}$ , AS4/PEEK$_{-45°}$ , AS4/PEEK$_{90°}$]$_s$ laminate.**

This plot is more surprising: the variations of the poisson's ratio for the entire laminate is non monotonic. $\upsilon_{xy}$ decreases with temperature until the end of the glass transition. At this point, $\upsilon_{xy}$ increases even after flow of the matrix. These variations are due to the non-linear relationship between the longitudinal and transverse moduli in each ply and temperature and efficiency factor. The stresses and strains were calculated in each ply for different loading conditions.

*3.4.1.1 Pure Axial loading*

The stresses (fiber direction) and strains (fiber direction) were calculated for a pure axial loading condition ($N_x$=10, $\Delta T$=0). The results are shown in (Figure 97 and Figure 98).

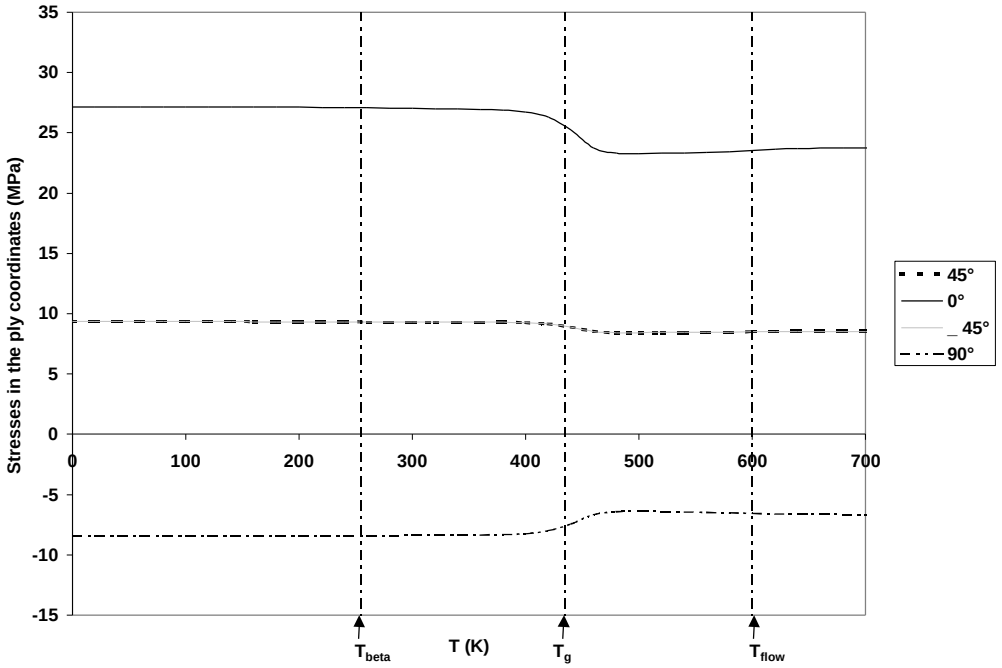


**Figure 97. Fiber direction stresses versus temperature in each ply. $N_x$=10 MPa. DT=0°C.**

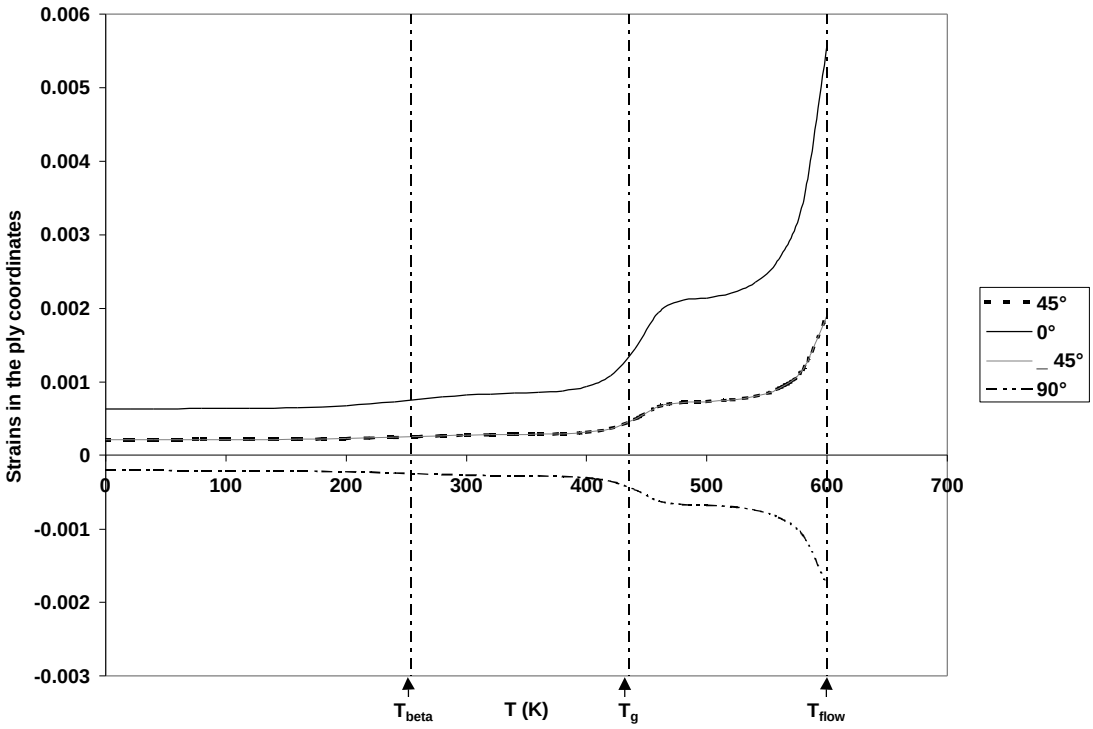


**Figure 98. Fiber direction strains versus temperature in each ply. $N_x$=10 MPa. DT=0°C.**

The stresses in the 0° and the ± 45° plies decrease until flow starts to occur. At this point, the stresses increase slightly, following the behavior of the composite's Poisson's ratio. The 90° ply follows the same trend but this time inverted: the stress increases up to a temperature above Tg then starts to slowly decrease. The strains (Figure 98) are monotonic in all the plies. The variations are amplified by the presence of the transitions.

*3.4.1.2 Thermal constraint*

Similar simulations were conducted on the laminate for a ΔT=-100°C (No mechanical load). The ply fiber direction stresses and strains are shown in Figure 99 and Figure 100.

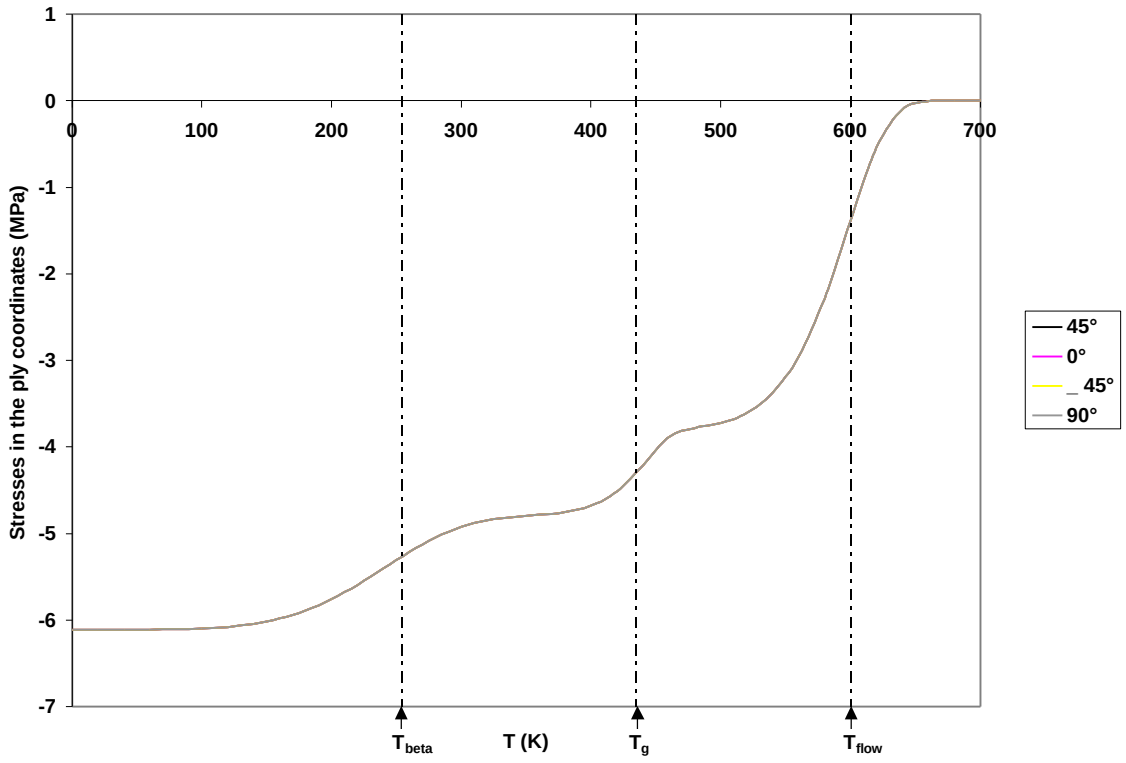


**Figure 99. Fiber direction stresses versus temperature in each ply. $N_x$=0 MPa. DT=-100°C.**

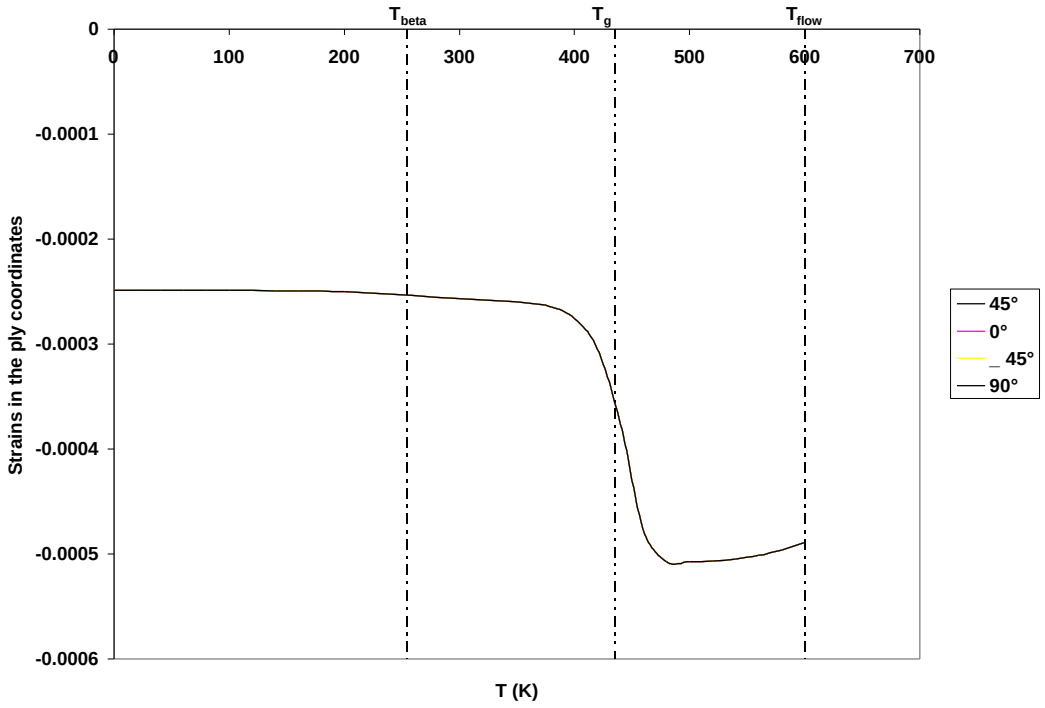


**Figure 100. Fiber direction strains versus temperature in each ply. $N_x$=0 Mpa. DT=-100°C.**

The stresses are identical in each ply (in the ply coordinates) and decrease to reach 0 after flow temperature. Inflection points mark the presence of the different transitions. The strains are also similar in the different plies: an abrupt drop in the strains is observed followed by a slight increase after the glass transition.

*3.4.1.3 Thermal and mechanical load combination*

The next case is the combination of the previous loads ($N_x$=10 MPa, $\Delta$T=-100°C). The results (in the fiber direction) are shown in Figure 101 and Figure 102.

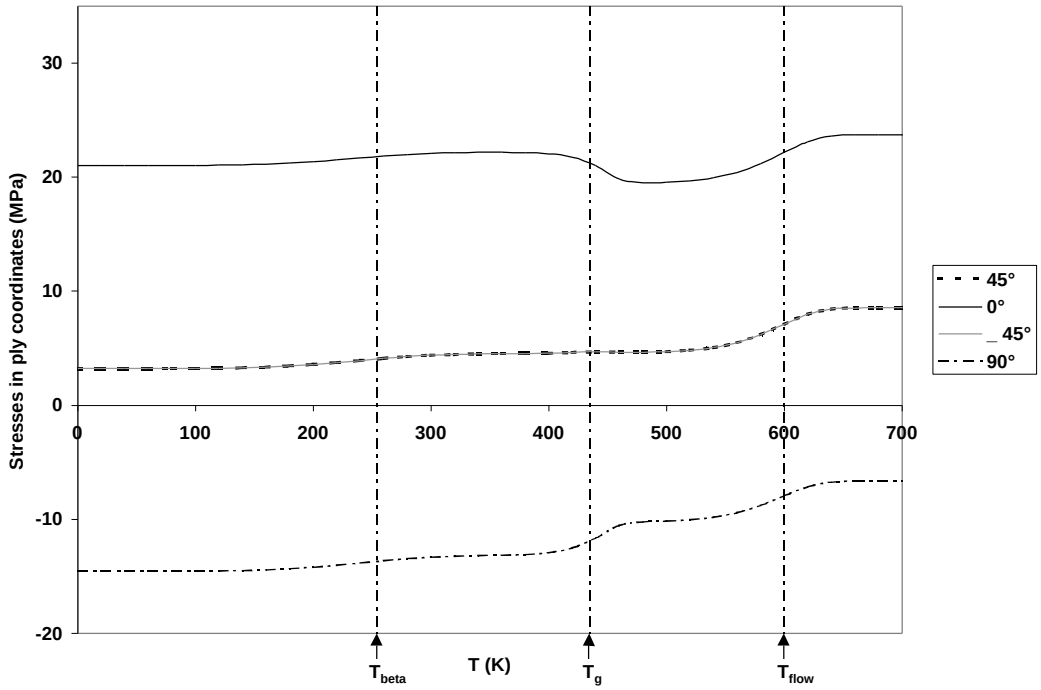


**Figure 101. Fiber direction stresses versus temperature in each ply. $N_x$=10 MPa. DT=-100°C.**

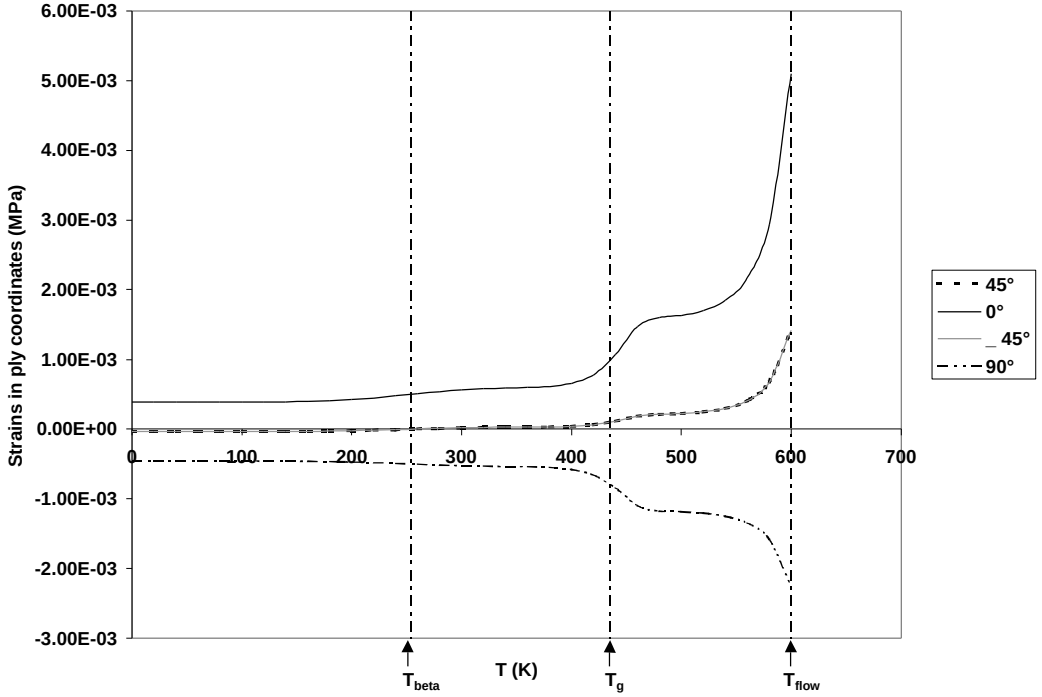


**Figure 102. Fiber direction strains versus temperature in each ply. $N_x$=10 MPa. DT=-100°C.**

The curves obtained are a combination of the two previous cases. The stresses increase slowly following the influence of the thermal load. The mechanical load induces differences in the response of the different plies. At Tg a drop is observed for the 0° ply and a rise is observed for the 90° ply. After the glass transition, the stresses start to slowly increase again for the 0° and the 45° plies. The fiber direction strains are monotonic and the shapes of the curves are similar to the case of pure mechanical loads.

### *3.4.2 AS4/PPS-AS4/PEEK hybrid laminate*

A similar numerical simulation was run on a hybrid laminate:

$$[AS4/PPS_{45°}, AS4/PPS_{0°}, AS4/PEEK_{-45°}, AS4/PEEK_{90°}]_s.$$

The different results for a $\Delta T$=-100°C and $N_x$=10 MPa are shown in the following Figures.

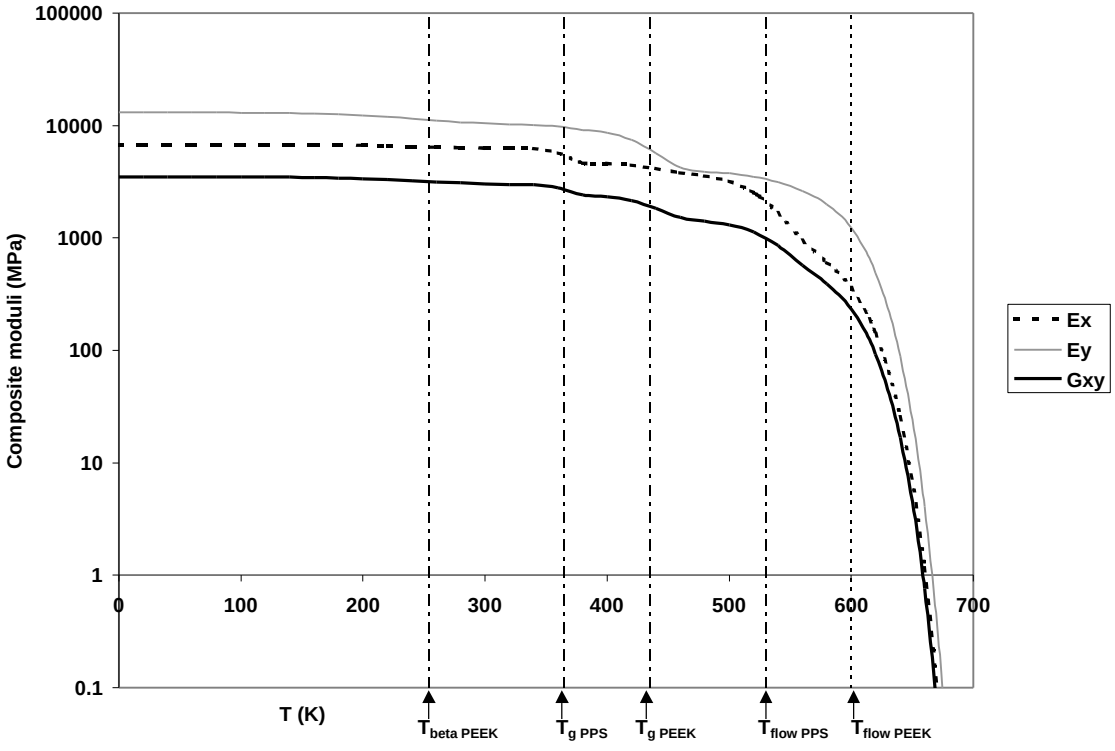


**Figure 103. $E_x$, $E_y$ and $G_{xy}$ versus temperature for the $[AS4/PPS_{45°}, AS4/PPS_{0°}, AS4/PEEK_{-45°}, AS4/PEEK_{90°}]_s$ laminate.**

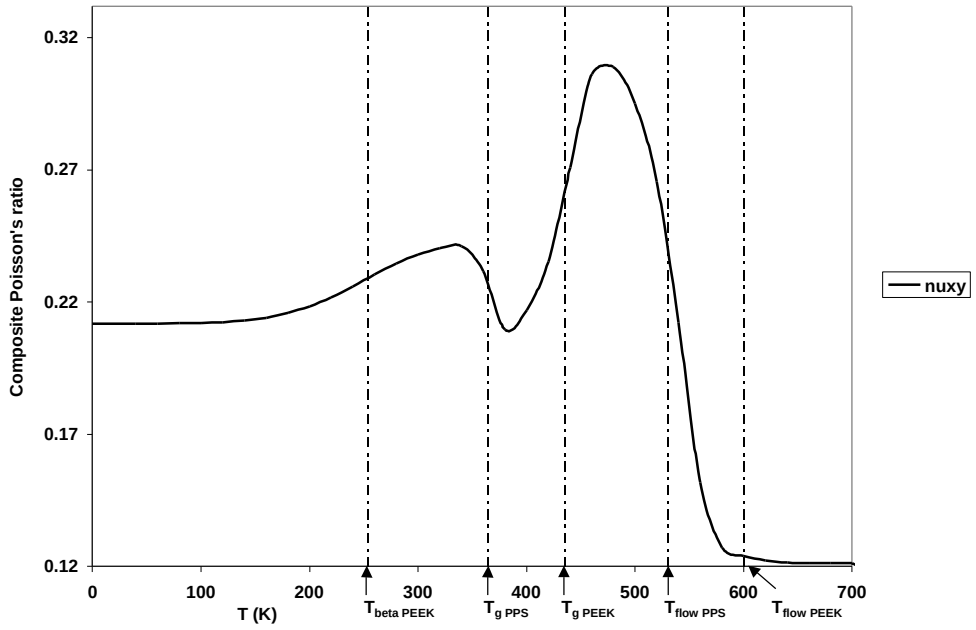


**Figure 104. $u_{xy}$ versus temperature for the $[AS4/PPS_{45°}, AS4/PPS_{0°}, AS4/PEEK_{-45°}, AS4/PEEK_{90°}]_s$ laminate.**

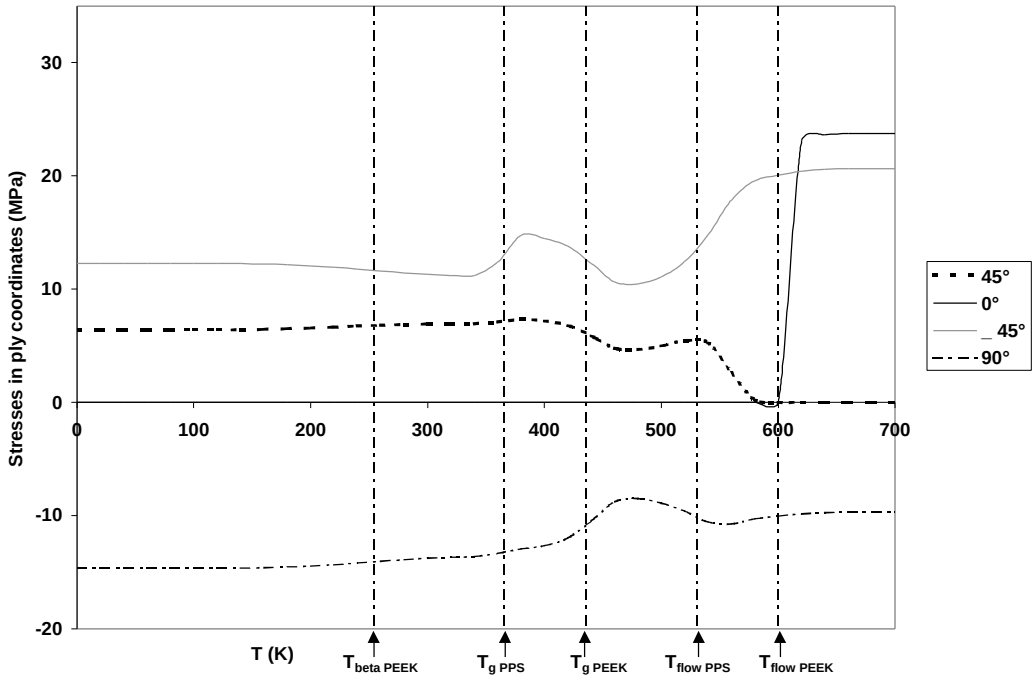


**Figure 105. Fiber direction stresses versus temperature in each ply. $N_x$=10 MPa. DT=-100°C. Hybrid laminate.**

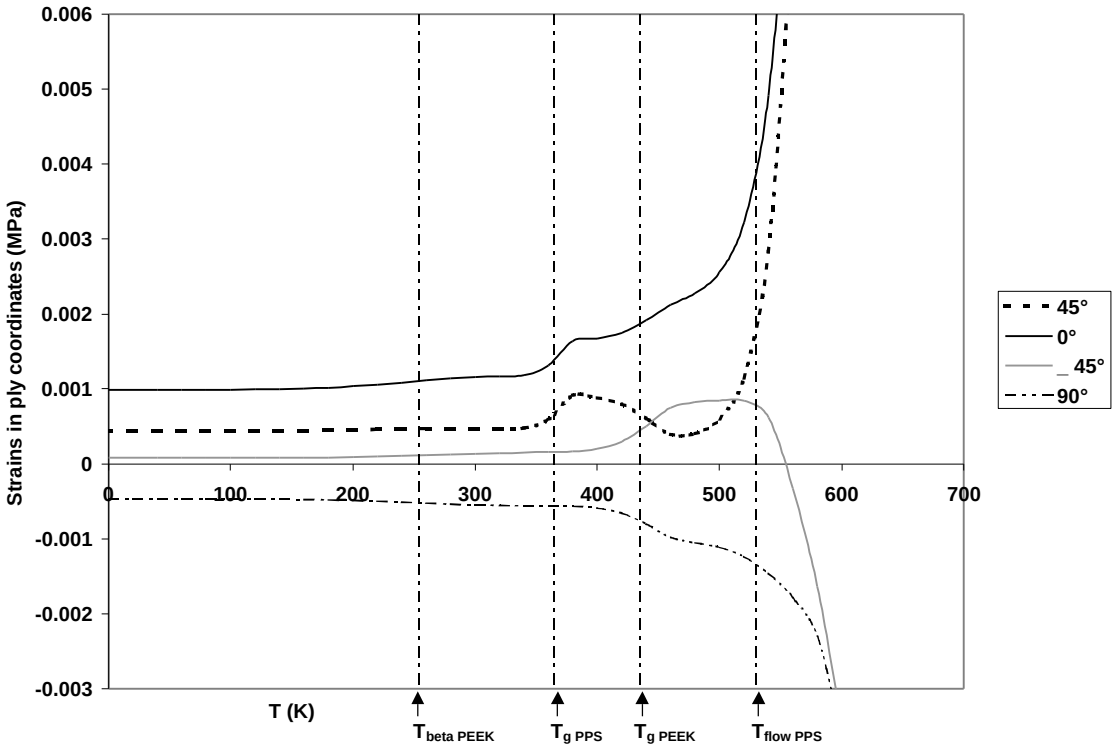


**Figure 106. Fiber direction strains versus temperature in each ply. $N_x$=0 MPa. DT=-100°C. Hybrid laminate.**

The moduli and Poisson's ration curves (Figure 103 and Figure 104) are very complex due to the presence of 5 transitions. The stresses (Figure 105) and strains (Figure 106) are different in each ply due to the difference in the matrix (PEEK or PPS). The behavior of the different plies in the fiber direction is clearly non-monotonic and very complex. The number of inflection points and maxima depend on the nature of the matrix and orientation of the fibers.

### *3.4.3 Discussion*

The outputs of the CLT combined with Equation 51 and Equation 52 are very surprising. The non-monotonic variations of the stresses and strains of the different plies in the fiber direction are related to the non-monotonic changes in the composite's

Poisson's ratio with temperature. It is difficult to compare these results with experimental data (measuring stresses and strains within the plies) and one must be prudent when analyzing the data: Poisson's ration was assumed constant for the consituents. However, the Poisson's ratio of a polymer is known to vary with temperature[13]. These variations might cancel the effects of the introduction of temperature via Equation 52 and lead to monotonic variations for $\upsilon_{xy}$. On the other hand, if the calculated stresses are close to reality, further study might allow new applications for these materials, such as thermally activated mechanical switching.

# Chapter 4 Conclusions and recommendations

## 4.1 Summary

A new engineering model has been established to enable the computation of stiffness variations with temperature, including those in the property transition regions. The feasibility of this approach has been demonstrated by applying this model to three thermoplastics, one elastomer and one thermoplastic-based composite over the entire solid-fluid temperature range (glassy to flow). The effects of crystallinity, molecular weight and filler content on the input parameters have been investigated for these four materials and are summarized in Table 13. The stiffness-temperature model was used in micromechanics models in order to predict the temperature dependency of the fiber direction stiffness response of unidirectional AS4/PEEK and AS4/PPS. The possibility of predicting the life of the first composite system in end-loaded bending was also investigated. The integration of the temperature dependence of the stiffness of the matrix into a life prediction model for composites (MRLife) was fairly successful. Finally, a new interesting behavior for the ply stresses of laminates with temperature was discovered.

**Table 13. Dependence of the input parameters on the microstructure**

| depend on ⇨ | Molecular Weight | Crystallinity | Filler content |
|---|---|---|---|
| $E_i$ | Yes | Yes | Yes |
| $T_i$ | Yes | Yes | Yes |
| $m_i$ | No | Yes | Yes |

## 4.2 Recommendations

This work focused on establishing new technical grounds and could not be exhaustive. Further work in several areas are required in order to validate the new

statements and concepts introduced in the present study. At the fundamental level, the statistics of bond breakage needs to be quantified in order to validate the arguments expressed concerning the relaxation of polymers and its relation to secondary bond breakage. In order to be used as an engineering prediction tool, the modulus-temperature model needs further refinement in the following areas.

### *4.2.1 Inputs for the polymer modulus versus temperature model*

It was established in the present dissertation that given the number of transitions, their magnitudes and the temperatures corresponding to these transitions, it is possible to establish the modulus versus temperature curve for any polymer. However additional work is needed in order to systematically compute these different inputs. The transition temperatures can be obtained through independent experiments such as dynamic scanning calorimetry (DSC). A careful literature review might also reveal the existence of viable models relating the microstructure of the polymer to the transition temperatures. For example, the glass transition temperature of a polymer can be theoretically calculated using the solubility parameter (i.e. the cohesive energy density)[88,89] or using the additivity of the structural groups. According to Van Krevelen[13]:

**Equation 104**

$$Tg = \frac{\sum_i s_i Tg_i}{\sum_i s_i}$$

where $Tg_i$ is the specific contribution to Tg of a given structural group and $s_i$ is a weight factor attributed to a given structural group. Tabulated values for each group are given (see Van Krevelen[13]) and the correlation between experimental and theoretical data is fair. The glass transition temperature does not only depend on the chemical nature of the molecules but also on their arrangement, i.e. molecular weight, cross-linking and crystallinity. The glass transition temperature can be related to the molecular weight (Mn) by an equation of the type:

**Equation 105**

$$Tg = Tg(\infty) - \frac{A}{\overline{Mn}}$$

A simple example of a degree of cross-linking-transition temperature relationship was established by Ueberreiter and Kanig[90]:

**Equation 106**

$$\Delta T_{g,c} = ZD$$

where $\Delta T_{g,c}$ corresponds to the change in the glass transition with increasing cross-linking, D the cross link density and Z is a tabulated value. More sophisticated cross-linking-transition temperature relationships have been established and can be used to compute the glass transition[1]. The glass transition is also very sensitive to the crystallinity content. The glass transition is approximately related to the melting point of a cystalline polymer by[91]:

**Equations 107**

$$\frac{Tg}{Tm} = 1/2 \quad \textit{for symmetrical polymers}$$

$$\frac{Tg}{Tm} = 1/3 \quad \textit{for unsymmetrical polymers}$$

The melting temperature (Tm) can be calculated using the additivity of structural groups[13]. Boyer[92] suggests semi-empirical relationships for the computation of the temperatures of the other transitions occurring in the polymer.

For the local mode relaxation, for example, (β relaxation) the transition temperature can be calculated from the glass transition temperature value at 100 Hz according to:

**Equation 108**

$$T(< Tg) \approx 0.75\, Tg$$

The analytical computation of the flow region requires further specific rheological study of the flow region.

The value of the instantaneous moduli in the different regions (initial height of the different plateaus) can be experimentally determined by a simple tension test. Once again, we ultimately would like to eliminate this experimental step by directly computing the values of the instantaneous modulus at the beginning of the different regions. According to Van Krevelen, the instantaneous modulus of the polymer in the solid state can be calculated using Equation 3 and Equation 4 presented in the first chapter. These

equations relate the modulus of the polymer to the Hartman function, tabulated for the different structural groups. Using additivity of the structural groups "ideal" moduli can be calculated for the solid polymer. Like the transition temperatures the instantaneous moduli of the polymer at a given temperature will not only depend on the nature of the polymer but on the molecular weight (Equation 28), degree of cross-linking (Equation 30) and crystallinity as well. A quantitative relationship between the instantaneous moduli after the beta transition ($E_2$ in Equation 52), after the glass transition ($E_3$ in Equation 52) and the percent of crystallinity was established by Khanna[80] but needs further validation:

**Equation 109**

$$\%\,crystallinity = \left[1 - \frac{\Delta \log E'}{2.46}\right] \times 100$$

and

**Equation 110**

$$\Delta \log E' = 2.46(\pm 0.14) \text{ for amorphous polymers}$$

### *4.2.2 The Weibull coefficients*

The Weibull coefficients were shown to vary linearly with crystallinity content and filler contents. Intuitively, we expect the Weibull parameters to also be related to the molecular weight distribution and the degree of cross-linking. Further experiments are required to establish theoretical models enabling the systematic computation of the Weibull coefficient associated with the different transitions as a function of these various parameters.

### *4.2.3 Other areas of interest*

To complete this study it would be useful to integrate the influence of other extrinsic parameters such as strain rate effects, moisture and chemical aggression. These different parameters will only influence the inputs of the model (transition temperatures, instantaneous moduli and maybe the Weibull coefficients).

Finally, the model needs further study and modifications to account for the possibility of bond re-formation (crystallization).

The different applications to composite models also needs to be further investigated:

### *4.2.4 Micromechanics*

The introduction of the temperature-dependent efficiency factor in the rule of mixtures for stiffness requires independent experimental validation. The characteristic parameters $\lambda_i$ in Equations 73 are probably related to the microstructure of the polymer and the polymer-fiber interface. A strong interface and a matrix that retain their mechanical properties with temperature (related to crystallinity, molecular weight, cross-linking…) will probably lead to efficiency factors very close to unity ($\lambda_1 >> \lambda_2$). However, this assumption needs further validation.

The coefficients $\mu_i$ associated with the shear stress of Equation 80 also need to be investigated in order to establish a relationship between the magnitude of these coefficients and the details of the materials' microstructure. Once again, we expect these coefficients to vary with crystallinity, molecular weight and crosslinking, and carefull observation of the materials' mechanical response with varying crystallinity can lead to the establishment of systematic relationships.

### *4.2.5 Strength*

The problem of fiber direction strength dependence of unidirectional composites has not been addressed in the present study. Making strength an explicit function of temperature would be a very powerful tool for the life prediction of PMC's.

### *4.2.6 End-loaded bending experiments on laminate composites*

The behavior of laminated composites in end-loaded stress-rupture and fatigue at elevated temperatures is unknown and further experimental work could allow us to validate the use of the polymer stiffness-temperature model in compression models.

### *4.2.7 The Classical Lamination Theory*

The results obtained using the Classical Lamination Theory need to be experimentally validated. If the calculated non-monotonic stress behavior is real, the possible engineering applications need to be identified.

**Finally, the polymer model can be applied to all other temperature related studies of polymer matrix composites, and life prediction schemes.**

## 4.3 Conclusions

This new model needs further study to be used as a comprehensive prediction tool. However it was demonstrated to offer great potential in reducing the experimental work required to design new composites. Ultimately this model could become a powerful tool in composites virtual design, enabling the use of Life Prediction tools, such as MRLife, over large temperature ranges including property transition regions.

## References


[1] Sperling, L. H., Introduction to physical polymer science, 2nd ed., John Wiley & Sons, Inc., New York, 1992

[2] Tobolsky, A. V., Properties and Structure of Polymers, wiley, New York, 1960

[3] Lennard-Jones, J. E., Proc. R. Soc. Lond., A106, 463, 1924

[4] Aklonis, J. J. and W. J. MacKnight, "Introduction to polymer viscoelasticity", 2nd Ed., Whiley & Sons, 1983

[5] Schatzki, T. F., J. Polym. Sci., 57, 496, 1962

[6] Boyer, R. F., Rubber Chem. Technol., 36, 1303, 1963

[7] Krishnaswamy, R.K., and D.S. Kalika, "Dynamic relaxation properties of poly(ether ether ketone)", Polymer, Vol. 35, No. 6, 1994

[8] Bartolotta, A., G. Di Marco, M. Lanza, and G. Carini, Journal of Polymer Science: Part B: Polymer Physics, Vol. 33, 93-104, 1995

[9] Wang, X. and J. K. Gilham, "$T_g$-temperature property ($T_g$TP) diagram for sermosetting systems: anomalous behavior of physical properties vs. extent of cure", Journal of applied polymer science, V 47 n 3, Jan 1993, pp. 425-446

[10] Krishnaswamy, R. K. and D. S. Kalika, "Dynamic mechanical relaxation properties of poly(ether ether ketone)", Polymer, v 35 n 6, Mar 1994, pp. 1157-1165

[11] Muzeau, E., J. Perez and G. P. Johari, "Mechanical spectrometry of the β relaxation in poly(methyl methacrylate), Macromolecules, 24, 1991, pp. 4713-4723

[12] Williams, M. L., R. F. Landel, and J. D. Ferry, J. Am. Chem. Soc., 77, 3701, 1955

[13] Van Krevelen, D. W., "Properties of polymers", 3rd Ed., elsevier, 1990.

[14] Hartmann B. and G. F. Lee, "Additive properties of some crosslinked epoxies", J. Appl. Phys. 51 (10), October 1980.

[15] Bicerano, J., "Prediction of polymer properties", M. Dekker, 1993

[16] Matsuoka, S., "Relaxation phenomena in polymers", Carl Hanser Verlag, 1992

[17] Gibbs, J. H., and E. A. DiMarzio, J. Chem. Phys., 28, 373, 1958

[18] Fox, T. G., and P. J. Flory, J. Appl. Phys., 21, 581, 581, 1950

[19] Kohlraush, R. Pogg. Ann. Phys., 12, 393, 1847

[20] Williams, G., and D. C. Watts, Trans. Fraday Soc. 1970, 66, 80

[21] Connolly M., F. Karasz, and M. Trimmer, Macromolecules, 28, 1872, 1995

[22] Ngai, K. L., R. W. Rendell, A. K. Rajagopal, and S. Teiltler, S. Ann. N.Y. Acad. Sci., 484, 150, 1986

[23] Rouse, P. E., J. chem. Phys., 21, 1272, 1953

[24] Bueche, F., J. Chem. Phys., 22, 603, 1954

[25] Zimm, B. H., J. Chem. Phys., 24, 269, 1956

[26] Peticolas, W. L., Rubber chem. Technol., 36, 1422, 1963

[27] Ferry, J. D., R. F. Landel, and M. L. Williams, J. Appl. Phys., 26, 359, 1955

[28] De Gennes, P-G., "Scaling Concepts in Polymer Physics," Cornell University, 1979

[29] Khanna, Y.P., "Estimation of polymer crystallinity by dynamic mechanical techniques," J. Appl. Polym. Sci., vol. 37, No. 9, May 1989

[30] Murayama, T., and J.P. Bell, J. Polym. Sci., 8, 437, 1970

[31] Cowie, J. M. G, "Polymers: chemistry & physics of modern materials", 2nd Ed., Blackie A & P, 1991

[32] Nielsen, L. E., Polymer Rheology, Dekker, New York, 1977

[33] Barnes, H. A., J. F. Hutton, and K. Walters, An Introduction to Rheology, Elsevier, Amsterdam, 1989

[34] Ninshino, T., H. Ohkubo and K. Nakamae, "Temperature dependence of the elastic modulus of crystalline regions of polyethylene with different microstructures. Explanation with the kinked-chain model", J. Macromol. Sci. Phys, v B31 n2, 1992, pp. 191-214

[35] Matsuo, M. and C. Sawatari, "Temperature dependence of the crystal lattice modulus abd the Young's modulus of polyethylene", Macromalecules, 21, 1988, pp. 1653-1658

[36] Rassmussen, R. S., J. Chem. Phys., 16, 712, 1948

[37] Shimanoushi, T., M. Ashina, and S. Enomoto, J. Polymer Sci., 590, 93, 1962

[38] McCrum, N. G., B. E. Read and G. Williams, "Anelastic and dielectric effects in polymeric solids, Dover ed., 1967

[39] Lacks, D. J. and G. C. Rutledge, "Temperature dependence of structural and mechanical properties of isotactic polypropylene", Macromolecules, Vol. 28, n 4, pp. 1115-1120.

[40] Lacks, D. J. and G. C. Rutledge, "Mechanisms for axial thermal contraction in polymer crytals: polyethylene vs isotactic polypropylene", Chemical engineering science, Vol. 49 n 17, 1994, pp. 2881-2888

[41] Lacks, D. J. and G. C. Rutledge, "Simulation fo the temperature dependence of mechanical properties of polyethylene", The journal of physical chemistry, Vol. 98 n 4, 1994

[42] Rigby, D., H. Sun, and B. E. Eichinger, Polymer International, 44, 311-330, 1997

[43] Boyd, R.H., "Relaxation Processes in Crystalline Polymers: Molecular Interpretation – A Review," polymer, Vol 26, august 1985

[44] Matthews, F. L. and R. D. Rawling, Composite Materials: Engineering and Science, Chapman & Hall, 1994

[45] Walther, B. M., "An Investigation of the Tensile Strength and Stiffness of Unidirectional Polymer-Matrix, Carbon-Fiber Composites under the Influence of Elevated Temperatures", Electronic Master Thesis, Virginia Tech, Blacksburg, 1998

[46] Crews, L.K., and H.L. McManus, "Modeling the Effects of High Temperature Exposure on the Mechanical Material Properties of Graphite/Epoxy," Proceedings of the 13th Annual Technical Conference on Composite Materials, September 21-23, Baltimore, MD, 1998

[47] Halpin, J. C., and S. W. Tsai, "Effects of Environmental Factors on Composite Materials," AFML-TR 67-423, June 1969

[48] Mahieux, C. A., B. E. Russell and K. L. Reifsnider, "Stress Rupture of Unidirectional High Performance Thermoplastic Composites in End-Loaded Bending at Elevated Temperatures. Part I Experimental Characterization of the failure mode," Journal of Composite Materials, volume 32, no.14, 98

[49] Mahieux, C. A., B. E. Russell and K. L. Reifsnider, "Stress Rupture of Unidirectional High Performance Thermoplastic Composites in End-Loaded Bending at Elevated

Temperatures. Part II Analytical Modeling," Scheduled to be published in Journal of Composite Materials, 98

[50] Russell B. E., C. A. Mahieux and K. L. Reifsnider, "Stress Rupture of PMC's in End-Loaded Bending," Journal of Applied Composites, 5, 151-159, 98

[51] Mahieux, C. A. and K. L. Reifsnider, "Effects of Out-of-plane Deformation on Stress Rupture of Unidirectional Polymer Matrix Composites," Composites and functionally graded materials, ASME 97, MD-Vol. 80

[52] Reifsnider, K. L. and W. W. Stinchomb, "A critical element model of the residual strength and life of fatigue loaded coupons," *Composite materials: Fatigue and Fracture*, ASTM STP 907, Edited by H. T. Hahn, ASTM, Philadelphia, 298-303, 1986

[53] Case, S., N. Iyengar, and K. L. Reifsnider, "Life prediction tool for ceramic matrix composites at elevated temperatures", Seventh symposium on composites: fatigue and fracture.

[54] McKenna, G.B., "Glass formation and glassy behavior," Comprehensive polymer science, Pergamon, 1989

[55] Mahieux, C.A., and K.L. Reifsnider, "Property modeling across transition temperature in polymers: a robust stiffness-temperature model", Submitted to Polymer, Dec 98.

[56] Ashby, M.F. and D.R.H. Jones, "Engineering materials 2: an introduction to microstructures, processing, and design"

[57] Platzer, N,, Progress in Polymer Engineering, Ond. And Eng. Chem., 61, no. 5, P.10, 1969

[58] Miller, M. L., Ther structure of Polymers. Reinhold Publishing Corp, New York, 1966

[59]Weibull, W., "A Statistical Theory of the Strength of Materials", Ingeniorsvertenskapsakademiens handlingar 151, 1939

[60] Schmieder, K. and K. Wolf, Kolloid Z., 127, 65, 1953

[61] Brennan, A.B., and Y.Q. Wang, Polymer, Vol 34, 4, pp.807-812, 1993

[62] Bartolotta, A., G. Di Marco, M. Lanza, and G. Carini, Journal of Polymer Science: Part B: Polymer Physics, Vol. 33, 93-104, 1995

[63] Risch, B.G., D.E. Rodrigues, K. Lyon, J.E. McGrath and G.L. Wilkes, Polymer, Vol 37, No 7, 1229-1242, 1996

[64] Chanda, M., and S. K. Roy, Plastics technology handbook, Marcel Dekker, Inc., New York, 1987

[65] Margolis, J. M., Engineering thermoplastics, properties and applications, Marcel Dekker, Inc., New York, 1985

[66] Devaux, J., et al, "On the molecular weight determination of poly(ary-ether-ether-ketone) (PEEK), polymer, Vol. 26, December, 1985

[67] Phillips Petroleum Company, private communication.

[68] Victrex, PEEK processing guide, 1998

[69] Young, R., and Baird, Society Plastics Engineers, ANTEC, Atlanta, 1998

[70] Mettler Toledo instruction notebook, density determination kit for AT/AG and PG/PG-S/PR balances

[71] Huo, P. and P. Cebe, "Dielectric relaxation of Poly(Phenylene Sulfide) containing a fraction of amorphous phase," Journal of Polymer Science: Part B: Polymer Physics, Vol. 30, 239-250, 1992

[72] Bas, C., M. Fugier and N. D. Albertola, "Reinforcement effect and molecular motions in semicrystalline PEEK films: Mechanical and Physical modelings. I," Journal of applied Polymer Science, 64, 1041-1052, 1997

[73] Marand, H., private communication

[74] www.shef.ac.uk/chemistry/webelements/nofr-heat/In.html

[75] Mahan, B.H., Thermodynamique chimique, Intereditions, 1977

[76] Lu, S.X., and P. Cebe, "Effects of annealing on the disappearance and creation of constrained amorphous phase," Polymer, Vol. 31, No. 21, 1996

[77] Bas, C., and D. Alberola, Polymer Journal, Vol. 29, No. 5, 1997

[78] Turi, E.A., "Thermal characterization of polymeric materials," Academic press, 1997

[79] Lu, S.X., P. Cebe, and M. Chapel, "Effects of molecular weight on the structure of Poly(phenylene sulfide) crystallized at low temperatures", Macromolecules, 30, 1997

[80] Khanna, Y.P., "Estimation of polymer crystallinity by dynamic mechanical techniques," J. Appl. Polym. Sci., vol. 37, No. 9, May 1989

[81] Jones, R. M., Mechanics of Composite Materials, Taylor & Francis, 1975

[82] Subramanian, S., Effect of Fiber/Matrix Interphase on the Long Term Behavior of Cross-Ply Laminate, Dissertation, Visrginia Tech, Blacksburg, 1994

[83] Budiansky, B. and N. A. Fleck. 1994. "Compressive kinking of fiber composites: A topical review", *App Mech rev*, 47(6)

[84] Russell, B. E. and K. L. Reifsnider, private communication.

[85] Pipik, S. F., B. E. Russell and K. L. Reifsnider, "Design of a compression bending fixture to test out-of-plane behavior of composite materials at elevated temperatures", NSF-SURP program. 1996

[86] Jackson, J. J. and K. L. Reifsnider, "End displacement bending fatigue life prediction of AS4/PPS composite material at elevated temperature", NSF-SURP program. 1997

[87] Case, S.W., private communication

[88] Boyer, R.F., Polym. Eng. Scien., 8, 161, 1968

[89] Boyer, R.F., "Encyclopedia of Polymer Science andEngineering," 2nd ed., Vol.17, pp.23-47, Wiley, New York, 1989

[90] Ueberreiter, K., and G. Kanig, J. Chem. Phys., 18, 399, 1950

[91] Boyer, R.F., "The Relation of Transition Temperatures to Chemical Structure in High Polymers," Rubber Chem. Technol. 36, 1303, 1963

[92] Boyer, R.F., J. Polymer Sci., Symposium No. 50, 189., 1975

## Vita

Céline A. Mahieux, daugther of Guitty Fakhr and Francis Mahieux, was born on February 23, 1973 in Teheran, Iran. She grew up in Argenteuil, a northern suburb of Paris, France. She attended Middle school and High school at the Collège et Lycée Notre Dame de Bury, France. After graduation she attended the Université de Technologie de Compiègne (UTC, France). After two years of general engineering she entered the department of Mechanical Engineering and specialized in Materials and Technologic Innovation. She was then selected for an exchange program between UTC and Virginia Polytechnic Institute and State University (VPI, USA). In August 1995, she moved to Blacksburg to enroll the Materials Science and Engineering Master's program and in January 1996, she started her research on composite materials in the Material Response Group of the Engineering Science and Mechanics department. After her graduation in December 1997, she pursued her research in the Materials Response Group as a doctorate candidate. Céline intends to pursue her fundamental study of composite materials in an academic environment.

Céline A. Mahieux